ABSTRACT

Title of dissertation: THE SELF-ASSEMBLY OF PARTICLES WITH MULTIPOLAR INTERACTIONS

Justin John Stambaugh,
Doctor of Philosophy, 2004

Dissertation directed by: Professor Wolfgang Losert
Department of Physics

In this thesis, we describe results from investigations of the self-assembly of anisotropically interacting particles. In particular, we focus upon the roles of dipolar and higher order multipolar interactions on the patterns of self-organization. Using an experimental model system of vertically vibrated magnetic spheres, we investigate the effects of octopolar and higher order interactions on the pattern of self-assembly. We show that simple theoretical point charge models can be used to provide insight into the underlying causes of the observed phenomena. We also show that such models can be used to better understand the pattern formation in several related physical systems, including biological macromolecular self-assembly and cohesive granular materials.

THE SELF-ASSEMBLY OF PARTICLES WITH MULTIPOLAR INTERACTIONS

by

Justin John Stambaugh

Dissertation submitted to the Faculty of the Graduate School of the
University of Maryland, College Park in partial fulfillment
of the requirements for the degree of
Doctor of Philosophy
2004

Advisory Committee:

Professor Wolfgang Losert, Chair/Advisor
Professor Edward Ott
Dr. Jack F. Douglas
Professor Daniel P. Lathrop
Professor Sandra Greer

ACKNOWLEDGMENTS

First, I would like to thank my adviser, Wolfgang Losert, for his guidance in the research presented here. His support and liberal allowance for freedom in my work has been an invaluable part of my Ph.D. experience.

I would also like to thank Ed Ott for his contributions to my research. His simple and elegant ideas have contributed to a large portion of this thesis.

Dan Lathrop deserves credit for the wonderful thought of studying these magnetic beads upon which a substantial portion of this thesis is based. I appreciate the time Don Martin has taken to teach me a significant number of useful skills, and help with numerous perplexing issues throughout my Ph.D. career. Dottie Brosius has helped me a great deal, both with printing my many posters, and by developing the LaTeX template in which this thesis has been written. I also thank Kevin Van Workum and Jack Douglas for contributing simulation work and some interesting background to this thesis. Dan Sackett, Jennifer Galanis and Ralph Nossal have provided a great deal of biological insight and guidance to my work, and I would like to thank them for their contributions to my research.

I owe tremendous gratitude to Zach Smith and Dave Jones both for their generous contributions to my research and for their guidance in computational matters. Kyuyong Lee, Matt Ferguson, Gene Kwon, Parul Rastogi, Nicolas Taberlet, Masahiro Toiya, Mike Newey, Peter Bradford, Andrew Pomerance, Sejin Han, Cory

Poole, Erin Rericha, Seung-Jong Baek, and Juan Gabriel Restrepo have provided many stimulating conversations, teachings, and insight, without which my creative thirst would have been quenched prematurely.

I am very grateful to my family and friends for their inspirational contributions to my life and my work.

Most of all, I would like to thank my wife, Jennifer, for her constant support and for putting up with four years of living meagerly during our pursuit of this graduate degree.

This work was supported by ONR (Physics), NSF (Grant No. 0243824, Physics098632), and NASA grant NAG32736.

CONTENTS

LIST OF TABLES

LIST OF FIGURES

1. INTRODUCTION

In this thesis, we describe results from investigations of the self-assembly of anisotropically interacting particles. In particular, we focus upon the roles of dipolar and higher order multipolar interactions on the patterns of self-organization. Using an experimental model system of vertically vibrated magnetic spheres, we investigate the effects of octopolar and higher order interactions on the pattern of self-assembly. We show that simple theoretical point charge models can be used to provide insight into the underlying causes of the observed phenomena. We also show that such models can be used to better understand the pattern formation in several related physical systems, including biological macromolecular self-assembly and cohesive granular materials.

1.1 Motivation

The self-assembly of anisotropically interacting particles is currently a topic of considerable interest for several fields of science. In particular, the self-assembly of biological macromolecules (which, in general, are anisotropically interacting) is of significant interest to the pharmaceutical industry because of possible therapeutic value [1, 2, 3, 4, 5]. For example, the popular chemotherapy drug Taxol targets

the self-organization of tubulin proteins in cancer cells and prevents cell division and the growth of tumors [2, 5]. Understanding the conditions which are favorable to self-assembly and what causes such conditions to be favorable is fundamental to the control of the polymerization. As a basic step toward understanding the self-assembly of anisotropically interacting particles, we investigate the self-organization of spheres with dipolar and higher order interactions.

Two-dimensional dipolar systems have been investigated using many different experimental and theoretical approaches [6, 7]. Patterns have been observed experimentally in nm to mm-sized magnetic particles suspended on the surface of a liquid [8, 9, 10, 11, 12], in a magnetic fluid containing nonmagnetic particles [10, 13], in magnetic bubbles in garnet films [14], in mm to cm-sized magnetically excited magnetized spheres [15], at the atomic scale in thin magnetic films [16, 17, 18, 19, 20, 21, 22, 23], in dipolar molecular fluids such as hydrogen fluoride [24, 25], and recently in mm-sized vertically vibrated magnetic spheres [26]. Studies of biological systems also suggest that dipole-dipole interactions between biological molecules may be an important part e.g. of pattern formation in a lipid monolayer [27, 28]. Monte Carlo simulations of the thermal equilibrium of large 2D systems of hard spheres with centrally embedded point dipoles have shown that ordering in the absence of external forces depends on the dipolar strength, the temperature of the system, and the number density of the spheres [11, 29, 30, 31].

Significant work has also been done on pattern formation in 3D systems of dipolar spheres [32, 33, 34, 35]. The investigations show that low-density 3D systems of dipolar spheres form chains and rings at low temperatures, but the chains

and rings do not coagulate to form a liquid phase. The lack of a liquid phase was suggested to be a consequence of the saturation of the interaction potential during chain formation, and the resulting lack of strong interactions between chains. In addition, because of the dissociation and recombination of the chains during equilibrium, this system of dipolar spheres has been compared to microscopic physical systems of so-called 'living polymers', which exhibit similar dynamic behavior [32]. The focus of our work is on the self-assembly of 2D systems of particles with dipolar and higher order magnetic interactions. We find that at low temperatures chains can collect to form a dense structure, in agreement with simulations of 2D systems of dipolar spheres by Clarke *et al.* [25].

The self-assembly of anisotropically interacting particles is of particular interest in molecular biology because of the wide array of biological systems which exhibit self-assembly and the variety of self-organized structures that are vital to the function of living cells [36, 37]. Studies of biological systems suggest that dipole-dipole interactions between particles play an important role in such phenomena as microtubule formation [38] and pattern formation in a lipid monolayer [27]. While the interactions between these nanoscale biological particles are difficult to rigorously model, simple model systems of dipolar spheres may provide insight into the dynamics of biological self-assembly in a fundamental manner.

There also is significant current interest in the dynamics of granular materials that have interactions in addition to the typical hard-sphere interactions. The dynamics of wet granular mixtures has been a recent focus as an example of pattern formation among isotropically attractive particles [39, 40]. In granular systems,

the addition of attractive forces between particles has been observed to both cause and prevent segregation under different circumstances [39]. The dynamics of dipolar interacting spheres is also of current interest as a novel granular material with anisotropic interactions [41, 42, 26]. Blair and Kudrolli [26] found that, in a vertically vibrated 2D mixture of magnetic and non-magnetic granular spheres, the magnetic spheres can self organize and cluster, depending on the volume fraction of magnetic particles and on the relative strength of the magnetic dipole-dipole interaction to the external vibration amplitude. In our earlier work [41], we showed that the shape of the magnetic field is another important factor in the self-assembly, ans the higher order moments of the interactions can significantly affect the pattern formation.

Moments of order higher than dipole are of particular importance to biological macromolecules, where macromolecular interaction potentials can be highly anisotropic to higher than dipole order, and small changes in the interactions can dramatically alter the self-assembly pattern (for example, see the self-assembly of sickle cell hemoglobin in Chapter 6). However, while the self-assembly of dipolar systems have been studied relatively extensively [6, 7, 8, 9, 10, 11, 12, 26, 29, 30, 31, 34, 43], the affects of higher order moments on self-assembly are, to a large degree, unknown. Relatively few simulations or theoretical studies using models which include higher order moments [24, 25, 27, 54] have been done. The purpose of this thesis is a detailed study of how higher order moments (in particular, octopole moments) affect the self-assembly of dipolar particles.

1.2 Outline of Thesis

In Chapter 2, we describe our experimental and theoretical methods. We give general schematics of our experimental setup, including a general description of the dipolar particles used. We also describe, in general, the models used to provide theoretical insight into the observed self-assembly.

In Chapter 3, we investigate the clustering transition as a function of temperature. We show, using our experimental system and Monte Carlo simulations performed by collaborators at *NIST*, that at temperatures above the clustering transition, the particles are largely dissociated from each other and exhibit traditional gas phase characteristics. At temperatures below the polymerization transition, the thermal (kinetic) energy of the particles is insufficient to overcome the attractive interactions and the particles form strongly bound clusters. The anisotropic nature of the dipolar interactions induces head-to-tail alignment, resulting in the formation of linear, ring, or branched structures. Between these two limits lies a broad transition region in which these polymer-like structures continuously form and disappear in dynamic equilibrium. Our results show that the transition temperature, T_Φ, increases and the width of the transition broadens with increasing concentration, C, in accord with the analytic theory of equilibrium polymerization. *(Work to be submitted to Physical Review E by J.Stambaugh, K. Van Workum, J. Douglas, and W. Losert.)*

Chapter 4 describes the effects of higher order multipole interactions. Pattern formation is investigated for a vertically vibrated monolayer of magnetic

spheres. The spheres, of diameter D, encase cylindrical magnetic cores of length, l. For large D/l, we find that the particles form a hexagonal-close-packed pattern in which the particles' dipole vectors assume a macroscopic circulating vortical pattern. For smaller D/l, the particles form concentric rings. The static configurational magnetic energy (which depends on D/l) appears to be a determining factor in pattern selection, even though the experimental system is driven and dissipative. *(Work published by J.Stambaugh, D. Lathrop, E. Ott, and W. Losert, Physical Review E,* ***68*** *026207 (2003).)*

In Chapter 5, we investigate binary systems of magnetic spheres. We show, using a simple experiment and numerical calculations, that in dilute self-assembled networks, a small change in the multipole moment distribution of a small fraction of the particles can significantly increase the branching in the self-assembled network. We also show that otherwise identical systems of magnetic spheres can segregate due only to differences in their magnetic fields. Vertically vibrated monolayers of magnetic spheres can segregate both by field strength and by field shape. In binary systems of particles with differing field strength and all other properties identical, the segregation increases with the proportion of weaker particles, and also increases approximately linearly with acceleration over the acceleration range studied. Binary systems of particles with differing field shape and all other properties identical also show approximately linear increases in segregation as acceleration is increased over the acceleration range studied. Segregation occurs in conjunction with a decrease in magnetic energy, with the energy decrease being mostly due to the actual segregation, rather than an evolution of the spatial pattern. *(Work*

published J.Stambaugh, Z. Smith, E. Ott, and W. Losert, Physical Review E, ***70*** *031304 (2004).)*

In Chapter 6, we discuss biological self-assembly. Specific examples of several relevant biological self-assembling macromolecular systems are given. We discuss the important interactions which govern the self-assembly, and, in particular, we describe the role of electrostatic interactions in self-assembly. We characterise the electrostatic properties of several of these macromolecules by calculating their electrostatic multipole moments up to octopole. We also describe a Monte Carlo method of developing minimal point charge models of the macromolecules which match the electrostatic multipole moments of real proteins up to the octopole terms.

Chapter 7 describes a minimal interaction model of the self-assembling protein, tubulin. We propose a simple point charge model of the protein tubulin, and we show that, without altering the dipole moment, the addition of higher order multipole moments to the model can energetically stabilise the biologically correct self-assembly pattern. The model consists of four static point charges embedded within an impenetrable rectangle with the dimensions of a tubulin dimer. We find that aggregates of the model tubulin dimers reproduce key features of microtubule structure: cylindrical shape, staggering, and fraying at the edges. We also present a physical macroscopic magnetic analog of our model, and show that it has many of the same structural characteristics as microtubules. *(Work to be submitted to Biophys. J. by J.Stambaugh, D. Jones, and W. Losert.)*

Appendix A is a detailed calculation of the multipole moments, up to octopole, of our model and experimental particles from Chapter 5. This

includes a determination of the conditions for matching the moments of the model and experimental particles.

In Appendix B, we theoretically analyze the preferred self-assembly patterns of some of our magnetic particles from Chapters 4 and 5 as a function of the system size. This includes a calculations of the energies of several different patterns of particles with dipolar and higher order interactions versus the number of particles in the patterns.

Appendix C is a detailed description of some of the energy calculations from Chapter 4. This includes a calculations of the energies of several different patterns of particles with dipolar and higher order interactions.

2. METHODS

2.1 Experimental

The following is a description of general characteristics of our experimental setup. Experimental details that are unique to each chapter will be described within the respective *Experimental Details* sections of each chapter. The experimental portion of this thesis is focused upon macroscopic two-dimensional systems of vertically vibrated magnetic spheres. Figure 2.1 is a schematic of the experimental setup used. A horizontal cylindrical container with a diameter 17.5 times a particle diameter and a height of 1.7 particle diameters was constructed with a black Delrin or gray polyvinyl chloride bottom and a rigid transparent acrylic top (for imaging). The system was imaged from above at a rate of 1-2 Hz using a grayscale or color CCD camera. The acceleration amplitude, a, was varied from $4g$ to $11g$ (where g is the acceleration of gravity) and was measured using an accelerometer. Magnetic spheres were placed in the container and sinusoidally vibrated vertically at 30 Hz using an electromagnetic shaker. The maximum strength of the magnetic field from the shaker at the inner container surface was 23.1 G at zero acceleration amplitude, although at typical acceleration amplitudes the RMS magnetic field strength was of order 1 G. No noticeable effect due to any external magnetic field from the shaker

was observed.

The magnetic particles used were cylindrical permanent magnets rigidly encased in spherical hard plastic shells. The plastic shells and some of the magnets (the 'long' magnets) are distributed as 'Magnetic Marbles' by the *Safari* toy company, and were purchased in the Smithsonian Air and Space Museum. Other magnets with differing properties were purchased elsewhere and were used to replace the existing *Safari* magnets in order to alter the multipolar interactions of the particles. Magnet materials were chosen for their resistance to demagnetization (both from vibration and opposing magnetic fields) and their physical strength. Magnetic field magnitudes of our particles were determined by measuring the maximum magnetic field on the surfaces of at least twenty particles using a Gauss meter and calculating mean and standard deviation of the measurements. Figure 2.2 is a general schematic of our magnetic particles. By altering the material makeup and the axial length l of the magnetic cores, we are able to independently change the dipolar and octopolar moments (from symmetry the quadrupole moments are identically zero). It may also be possible to construct similar magnetic particles with nonzero quadrupole moments by, e.g., slicing a cylindrical magnet vertically along its axis, rotating one of the halves 180^o about the axis perpendicular to the slicing plane, then fixing the halves back together. The quadrupole moment would then be a function of l, and the particles would have zero dipole moment. Another method of constructing partlicle with non-zero quadrupole would be to permenantly attach the north faces of two cylindrical magnets together such that the magnetic dipoles are opposing. However, for the remainder of this thesis, we will describe observations of magnetic particles

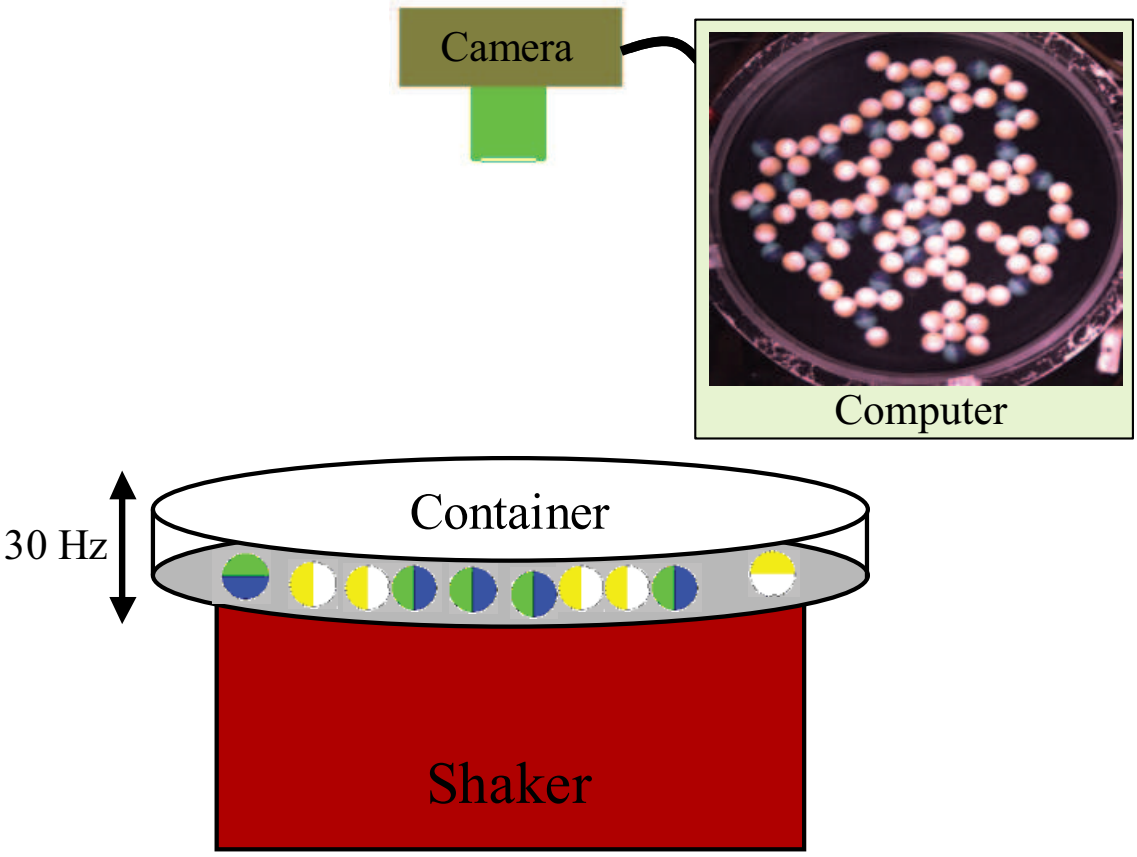

Fig. 2.1: A schematic of the experimental setup. Magnetic spheres are placed in a 2D container and vertically vibrated at 30 Hz. The system is imaged from above.

with zero quadrupole moments. For the majority of the experiments described in this thesis, the particles were constructed to have differently colored northern and southern hemispheres so that dipole orientations could be discerned.

2.2 Theoretical Models

The following is a description of general characteristics of our theoretical magnetic particle models. Model details that are unique to each chapter will be described within the respective *Energetic Considerations* sections of each chapter. The theo-

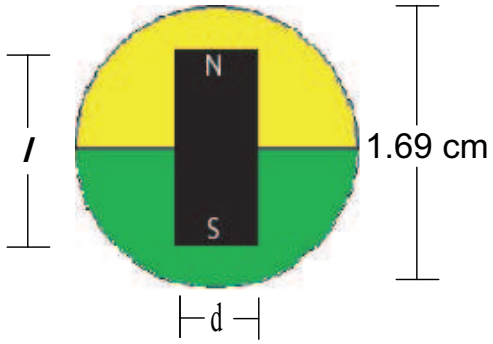

Fig. 2.2: A general schematic of the magnetic particles used. The material makeup and l of the magnetic cores were parameters that were varied to independently alter the strengths of the dipolar and octopolar interactions.

retical models in this thesis consist of two to eight static point charges surrounded by appropriately shaped impenetrable boundaries. Figure 2.3 is a general schematic of my model of the magnetic spheres described in fig. 2.2. The model consists of impenetrable spheres of diameter, D, containing four magnetic 'charges' of equal magnitude $\pm q$, separated by distances h and w ($0 < h, w \leq D$), such that the charges are at the corners of a rectangle. This model is a two-dimensional theoretical analog of our three-dimensional particles. h, w, and q were varied to independently change the dipolar and octopolar moments (from symmetry the quadrupole moments are identically zero), and mimic the interactions of the magnetic spheres in the experiment. This model reduces to a two-charge model in the limit of $w/D \to 0$. It can also be reduced to a two-point-dipole model in the limit of of $h/D \to 0$, and a single, centrally located point dipole model if $h/D \to 0$ and $w/D \to 0$. Similar point charge models were also developed to describe interactions between anisotropically

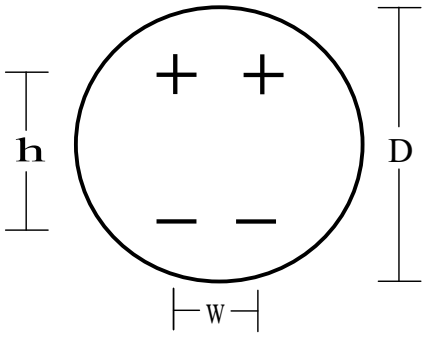

Fig. 2.3: A schematic of our general magnetic particle model. The model consists of four point charges of equal magnitude $\pm q$, separated by distances h and w ($0 \leq h$, $w \leq D$), such that the charges are at the corners of a rectangle.

interacting biological macromolecules. Those will be described in Chapters 6 and 7.

2.3 The Multipole Moment Expansion

The electrostatic potential of any system of static electric charges can be expanded about a point using the well-known multipole expansion [55],

$$\Phi(\mathbf{x}) = \frac{1}{4\pi\epsilon_0} \sum_{l=0}^{\infty} \sum_{m=-l}^{l} \frac{4\pi}{2l+1} q_{lm} \frac{Y_{lm}(\theta,\phi)}{r^{l+1}}, \tag{2.1}$$

where Y_{lm} are the spherical harmonics, r is the distance from the expansion center,

$$q_{lm} = \int Y^*_{lm}(\theta',\phi') r'^l \rho(\mathbf{x}') d^3x', \tag{2.2}$$

and $\rho(x)$ is the charge density at position x. In general, the $l = 0$ term in the expansion is named the 'monopole' term, the $l = 1$ term in the expansion is named the 'dipole' term, the $l = 2$ term in the expansion is named the 'quadrupole' term, $l = 3$ term in the expansion is named the 'octopole' term, and so on for higher order

terms. In general, we may also speak of 'multipole moments' to characterise the various terms in the multipole expansion. In this thesis, we define these moments as follows:

- Monopole Moment (scalar),

$$Q = \sum_{i=1}^{N} q_i \tag{2.3}$$

- Dipole Moments (vector),

$$p_j = \sum_{i=1}^{N} q_i j_i \tag{2.4}$$

- Quadrupole Moments (traceless rank 2 tensor),

$$Q_{jk} = \sum_{i=1}^{N} q_i (3 j_i k_i - r_i^2 \delta_{jk}) \tag{2.5}$$

- Octopole Moments (rank 3 tensor),

$$O_{jkl} = \sum_{i=1}^{N} q_i j_i k_i l_i \tag{2.6}$$

In general, these moments are associated with their respective terms in the expansion through the following relation:

$$\Phi(\mathbf{x}) = \frac{1}{4\pi\epsilon_0} \left[\frac{Q}{r} + \frac{\mathbf{p} \cdot \mathbf{x}}{r^3} + \frac{1}{2} \sum_{i,j} Q_{ij} \frac{x_i x_j}{r^5} + ... \right]. \tag{2.7}$$

3. POLYMERIZATION TRANSITIONS IN TWO-DIMENSIONAL SYSTEMS OF DIPOLAR SPHERES

(Simulations by Kevin Van Workum and Jack F. Douglas, Polymers Division, National Institute of Standards and Technology)

3.1 Overview

In this chapter, we investigate the clustering transition in our two-dimensional system of magnetic spheres, as a function of vibration amplitude. Following previous work on vertically vibrated granular matter [44], we draw an analogy between vibrational excitation in our experimental system and thermal excitation in a Monte Carlo simulation of a similar system. We show, using our experimental system and Monte Carlo simulations performed by collaborators at *NIST*, that at temperatures above the clustering transition, the particles are largely dissociated from each other and exhibit traditional gas phase characteristics. At temperatures below the polymerization transition, the thermal (kinetic) energy of the particles is insufficient to overcome the attractive interactions and the particles form strongly bound clusters. The anisotropic nature of the dipolar interactions induce head-to-tail alignment resulting in the formation of linear, ring, or branched structures. Between these

two limits lies a broad transition region in which these polymer-like structures continuously form and disappear in dynamic equilibrium. Our results show that the transition temperature, T_Φ, increases and the width of the transition broadens with increasing concentration, C (measured as particle area fraction in our 2D system), in accord with the analytic theory of equilibrium polymerization [48].

It is important to have well-defined models of self-organization that contain the minimal physical characteristics of those systems and to extensively study the essential characteristics of these systems. We need to determine what kind of thermodynamic transitions are involved and how to determine the relevant interaction parameters. The dynamical properties of these systems (formation and the properties while functioning) are also a crucial concern and we need to develop simple models that are amenable to large scale simulations so that these properties can be studied with existing computational resources. Optimally, the physical systems chosen should have well-defined physical realizations that can be compared to both simulation and analytic theories of self-organization.

Van Workum and Douglas [49] have advocated dipolar fluids as a prototypical model of self-organization and they have extensively investigated the polymerization transition which occurs in this model by Monte Carlo simulations in three dimensions. Stambaugh and Losert [41, 42] have experimentally and theoretically studied the self-assembly of spheres with multipolar interactions and have found sensitive dependance of the self-assembly pattern on higher order moments. This chapter considers a physical realization of a dipolar fluid constrained to be nearly two-dimensional, and a corresponding Monte Carlo simulation of this two-dimensional

fluid. This comparison not only provides a check on the physical model developed involving magnetic particles shaken vertically to thermalize the granular fluid, but provides a valuable check on the thermodynamic characteristics provided by the Monte Carlo simulations and the analytic theory of equilibrium polymerization. The choice of the dipolar fluid is independently motivated by the fact that protein molecules characteristically have large electrostatic dipole moments (e.g. tubulin $\approx$ 1400 Debye, as will be shown in Chapter 6) and dipolar interactions clearly have relevance to the self-organization processes occuring in proteins [77].

3.2 Experimental Details

The magnetic particles used in this chapter had magnetic cores of length, $l = 1.42 \pm 0.01$ cm., and diameter, $d = 0.94 \pm 0.01$ cm. The particles (*long* particles) were 5.3 ± 0.1 grams in mass, the maximum strength of the magnetic field on the surface of a particle was 0.54 kG $\pm 16\%$, and the particle diameter, D, was 1.69 ± 0.01 cm. The container is constructed with a black Delrin bottom and N particles were placed in the container, to give a system concentration, $C = \frac{N}{17.5^2}$ prior to vibration. The system was imaged from above at a rate of 0.5 Hz with a 1280x1024 pixel color camera. a was varied from $5g$ to $11g$.

Earlier work has shown that a direct analogy can be made between the excitation of macroscopic particulate matter by vertical shaking and thermal excitations of microscopic matter [44]. For the range of driving amplitudes studied, this analogy

can be quantified by the expression

$$T \propto v_p^2, \tag{3.1}$$

where T is the effective temperature and v_p is the peak velocity of the vertically vibrated surface. v_p can be easily calculated from the vibration acceleration and frequency, and hence, we define our experimental temperature as $T = v_p^2$.

3.3 Simulation Details

Simulations performed by Kevin Van Workum and Jack F. Douglas, Polymers Division, National Institute of Standards and Technology.

The magnetic particles are modeled as hard spheres, as described in Chapter 2, but with $w = 0$ such that they are made up of two oppositely charged monopoles. The monopoles are separated by a distance $h = 0.69D$ and are situated symmetrically about the center of the sphere. The potential energy between monopole i on sphere a and monopole j on sphere b is given by

$$u_{a_i b_j} = \frac{q_{a_i} q_{b_j}}{r_{a_i b_j}}, \tag{3.2}$$

where $r_{a_i b_j}$ is their separation distance and the q's denote the charges of the monopoles. This model is chosen to effectively represent the real interactions of the magnetic particles used in the experiments.

In order to mimic the quasi-two-dimensional nature of the experimental setup, the centers of the spheres are restricted to lie in a plane while the embedded dipole vectors are allowed to rotate in 3D. All the spheres also interact with a boundary

consisting of a radially symmetric hard wall (a cylinder) similar to that in the experiments.

Canonical ensemble Monte Carlo (MC) simulations are used to generate equilibrium configurations and thermodynamic averages. In addition to the traditional translational and rotational MC moves, two advanced MC methods are implemented. The Aggregate Volume Bias MC method [45] is used to enhance the dynamic formation and destruction of clusters. This method provides efficient phase space sampling in systems that form strong interparticle associations such as those present in this study. The Parallel Tempering MC method [46, 47] is also used in these simulations to provide improved statistical sampling. In this algorithm, several independent simulations proceed in parallel, each at a different temperature but with the same number of particles. Periodically, two simulations adjacent to one another with respect to their temperatures are chosen at random and a swap of their particle configurations is attempted. Attempted swaps are accepted with a probability given by

$$p_{a\leftrightarrow b} = \min[1, \exp\{\Delta U \Delta\beta\}], \tag{3.3}$$

where $\Delta U = U_b - U_a$ is the potential energy difference of the systems, and $\Delta\beta = 1/(k_B T_b) - 1/(k_B T_a)$. T, for the simulations, is defined in units of the dipolar particle self-energy divided by k_B. At low temperatures, the particles can form large, strongly associated clusters that may become trapped in local potential energy minima causing the exploration of relevant phase-space to proceed inefficiently. At high temperatures the particles are largely free from such constraints and the simulation

samples configuration space more effectively. By 'connecting' the simulations at low temperature to those at high temperature through Parallel Tempering, one improves the statistical sampling of phase-space. In the present study, 24 simulations were used at each concentration and adjacent simulations differed in temperature by $\Delta T = 0.01$.

3.4 Results

Based on previous analytical modeling [48] and Monte Carlo simulations [49] of equilibrium polymerization of the Stockmayer fluid (dipolar spheres with additional isotropic Lennard-Jones van der Waals interactions), we anticipate a polymerization transition to occur at constant concentration. At temperatures above the polymerization transition, the particles are largely dissociated from each other and exhibit traditional gas phase characteristics. At temperatures below the polymerization transition, the thermal (kinetic) energy of the particles is insufficient to overcome the attractive interactions and the particles form strongly bound clusters. The anisotropic nature of the dipolar interactions induces head-to-tail alignment, resulting in the formation of linear, ring, or branched structures. Between these two limits lies a broad transition region in which these polymer-like structures continuously form and disappear in dynamic equilibrium. For the present, we loosely define the polymerization transition temperature, T_Φ, as the temperature at which the particles first begin to form clusters. A more rigorous definition of T_Φ based on the average cluster size follows.

As examples of the observed structures, Fig. 3.1 show the experiment (a-c) for $C = 0.026$ at $T/T_\Phi > 1$, $T/T_\Phi \approx 1$, and $T/T_\Phi < 1$, respectively. Fig. 3.1 (d-f) shows similar renderings of the simulations for $C = 0.026$ at $T/T_\Phi > 1$, $T/T_\Phi \approx 1$, and $T/T_\Phi < 1$, respectively. For $T/T_\Phi < 1$, a linear chain of head-to-tail aligned particles is observed and for $T/T_\Phi > 1$ the particles are completely dissociated. Near the transition, $T/T_\Phi \approx 1$, a fraction of particles are loosely associated while the remaining are dissociated. This is our first hint that the observed broad transition involves the dynamic formation and destruction of polymeric chains at equilibrium with larger chains forming as the temperatures decreases.

We first characterize the transition by monitoring the average cluster size as a function of temperature. Two particles are considered to be part of the same cluster when their interparticle distance is less than $r_a = 1.125\sigma$. Based on previous work [50], the observed average cluster size is expected to be relatively independent of small changes in r_a. The average cluster size is then defined by

$$L = \frac{\sum_{i=1}^{N} iN_i}{\sum_{i=1}^{N} N_i}, \tag{3.4}$$

where i is the number of particles in a given cluster and N_i is the number of chains of length i. In Fig. 3.2, we show L as a function of T for the experiments (a) and the simulations (b) for a range of concentrations. We find a family of curves describing the general increase of L upon cooling. At higher concentrations, the increase in $L(T)$ occurs faster as T is lowered, reflecting the concentration dependence of the polymerization transition. The curves in Fig. 3.2 notably have a similar shape, and it is natural to seek a reduced variable description.

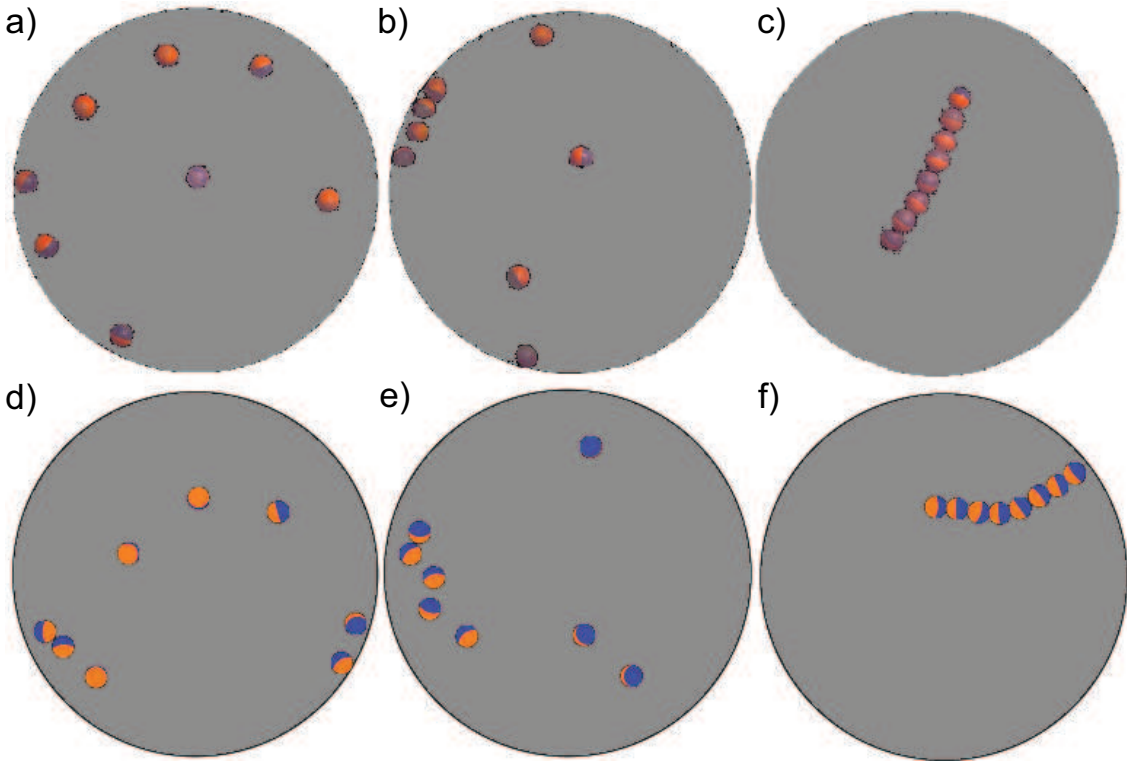

Fig. 3.1: A photograph of an experimental system where the concentration $C = 0.026$ at three different temperatures: $T/T_\Phi > 1$ (a), $T/T_\Phi \approx 1$ (b), and $T/T_\Phi < 1$ (c). A rendering of the simulation where $C = 0.026$ and: $T/T_\Phi > 1$ (d), $T/T_\Phi \approx 1$ (e), and $T/T_\Phi < 1$ (f).

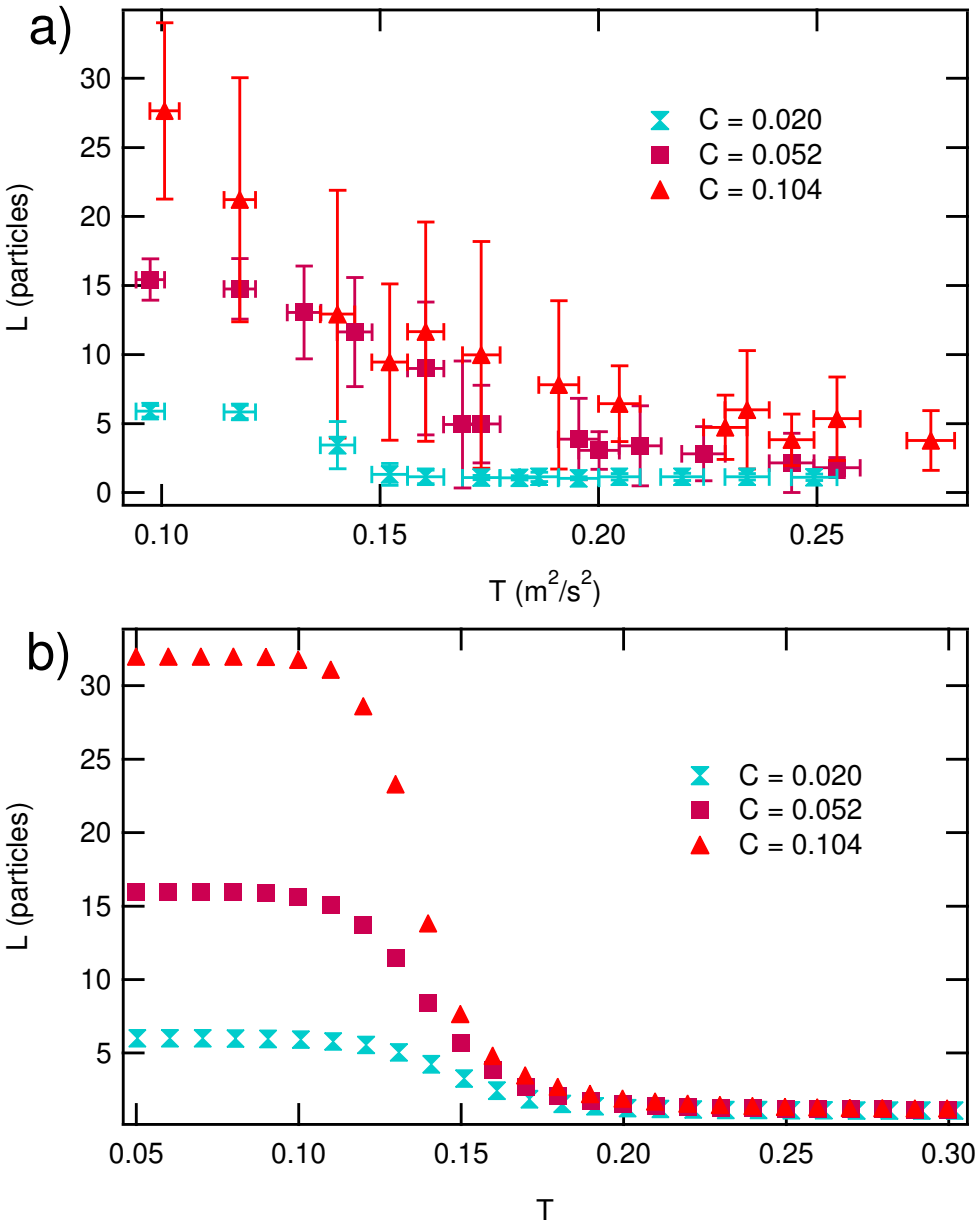

Fig. 3.2: a) A plot of L as a function of T for experimental systems where $C = 0.020$, 0.052, and 0.104. b) A plot L as a function of T for similar simulated systems.

Previous simulations of the polymerization transition in the Stockmayer fluid have demonstrated that a universal reduced variable description of the temperature dependence of L can be obtained by expressing temperature relative to its value of the polymerization transition, T_Φ defined by an inflection point in the order parameter for the polymerizatino transition Φ (See Eqn. 3.5 for definition). It was also found that L at this temperature is nearly universal, taking a value 2.1 regardless of particle concentration [49]. This result is predicted also by the analytic theory of equilibrium polymerization [48]. We checked this relation for the simulated analog of our experimental system and found that L at the polymerization transition (T_Φ) again lies in a narrow range for the concentrations we consider. This universality in the magnitude of L at T_Φ suggest that we should similarly be able to reduce the scatter in the measurements in Fig. 3.2 by simply normalizing temperature by the temperature where $L = 2$, to obtain an approximate equation of state description of the T dependence of L. This procedure is motivated by the comparitively noisy nature of our Φ data.

We see from Fig. 3.3(a) that this procedure indeed reduces the scatter considerably and the reduction is quite good for the approach to the polymerization transition temperature $T \to T_\Phi$ where $L = 2$. Note that the simulation data in Fig. 3.3(b) exhibits a tendancy to saturate to a finite value, which is simply the number of particles in the system. This feature is a finite size effect and the growth of L at low T is apparently unbounded in the thermodynamic limit, as found before for the three-dimensional Stockmayer fluid. The chains in the experiment also visually exhibit a saturation of chain length to a size corresponding to the number of

particles in the system at low T, but the particle tracking algoithm can not follow these large clusters reliably, giving rise to the residual scatter in Fig. 3.3(a) and the absence of a discernable plateau. Nevertheless, Fig. 3.3(a) clearly indicates the sharp rise in L at lower T and the significance of $L(T_\Phi) = 2$ in defining a reduced variable description of these observations. We also note that our determination of $\Phi(T)$ below is consistent with $L(T_\Phi) \approx 2$ within experimental uncertainty in our experimental system and we could equally as well have reduced our L data by T_Φ values determined directly fomr the inflection point of Φ Both procedures lead to a regettable large scatter at low T, where the uncertainties from our particle tracking estimates of L and Φ are large.

It is also natural to monitor the average fraction of particles that are members of a cluster, i.e. the extent of polymerization, Φ. The extent of polymerization is defined by

$$\Phi = \frac{N_p}{N}, \tag{3.5}$$

where N_p is number of polymerized (reacted) particles and N is the total number of particles in the system. Φ therefore defines an order parameter where $\Phi = 0$ corresponds to an entirely dissociated system, and $\Phi = 1$ corresponds to a state where all the particles are in contact with at least one other particle.

Figure 3.4(a) is a plot of Φ versus T for experimental systems where $C =$ 0.020, 0.052, and 0.104. A transition from $\Phi \approx 1$ to $\Phi \approx 0$ is seen with increasing T for $C = 0.020$, while the transitions for $C \geq 0.052$ are partially captured for the temperature range studied. While it is likely that observations of the $C \geq 0.052$

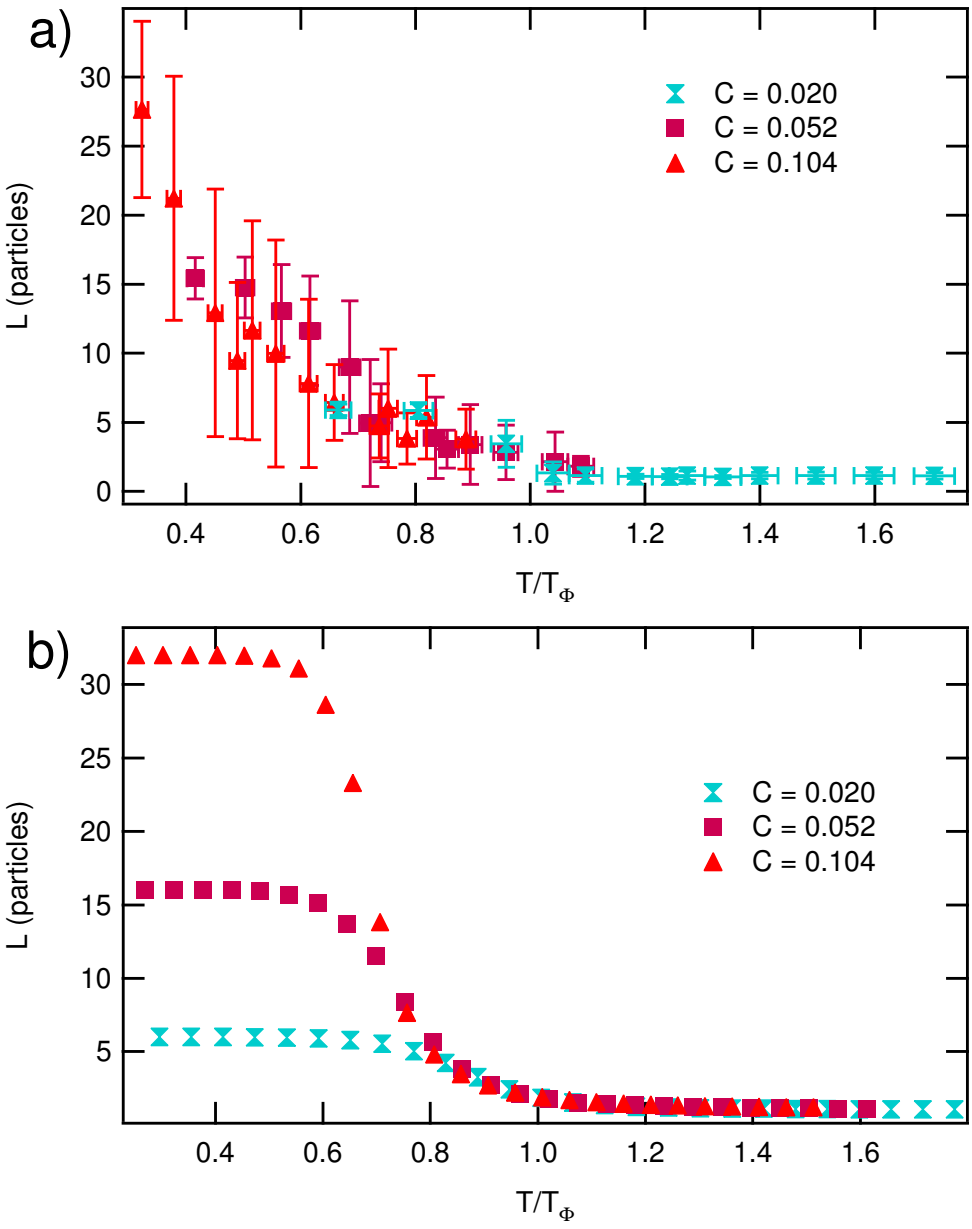

Fig. 3.3: a) A plot of L as a function of T/T_Φ for the experimental systems where $C = 0.020$, 0.052, and 0.104. b) A plot of L as a function of T/T_Φ for similar simulated systems.

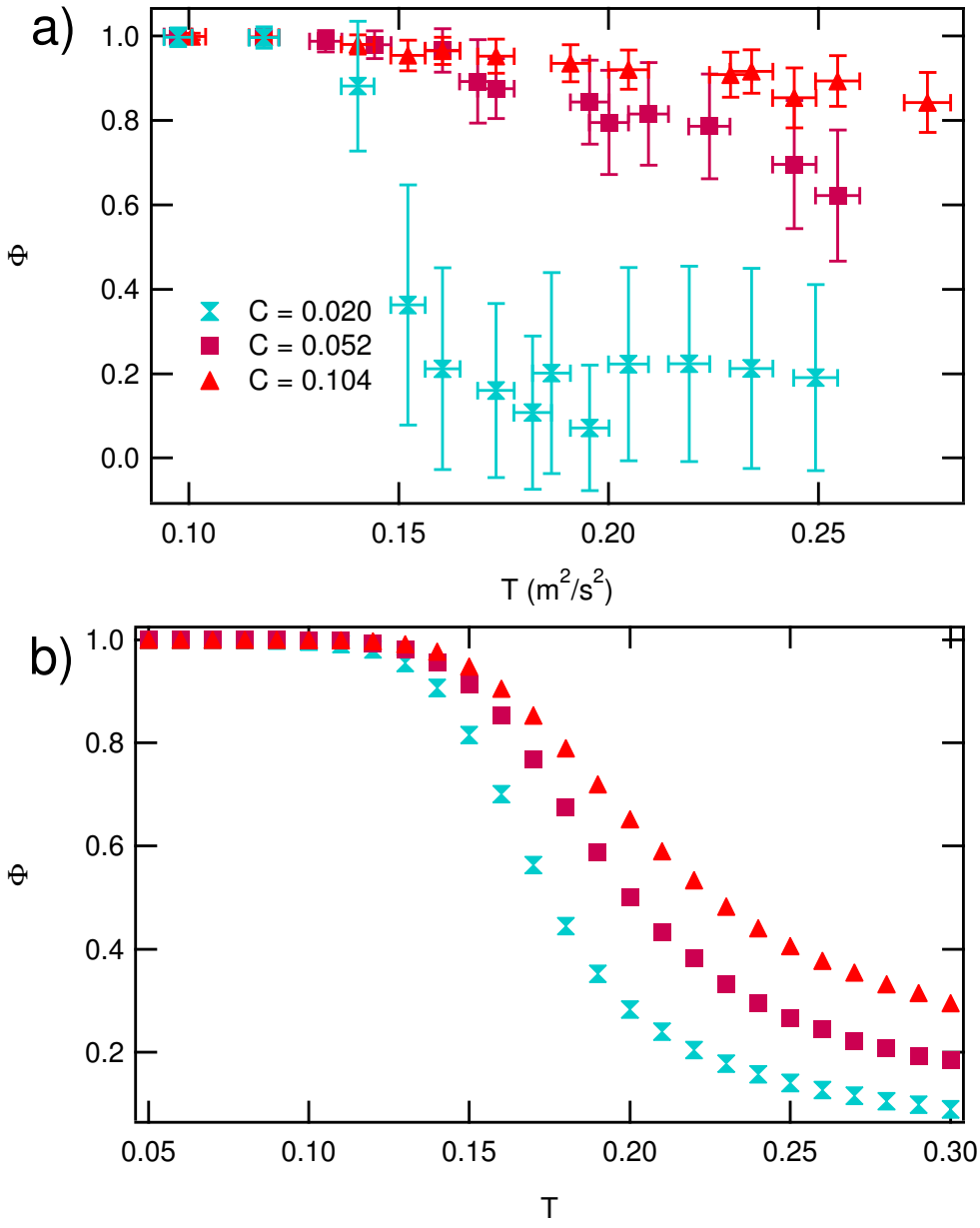

Fig. 3.4: (a)A plot of Φ versus T for experimental systems where $C = 0.020$, 0.052, and 0.104. (b) A similar plot of Φ versus T for similar simulated systems. Note that for both simulation and experiment, T_Φ increases and the transitions broaden with increasing C.

systems at higher T would show transitions similar to those at $C < 0.052$, the experimental setup limited our observations to $T < 0.3$. Figure 3.4(b) is a plot of Φ versus T for simulated systems for $C = 0.020$, 0.052, and 0.104. A transition from $\Phi \approx 1$ to $\Phi \approx 0$ is seen with increasing T for all C. While the simulation methods exclude the possibility of investigating temporal dynamics, the experimental system allows a detailed study of the evolution of the spacial patterns in time.

Figure 3.5 is a plot of Φ versus time for the experimental system where $C = 0.052$ and $T \approx T_\Phi$. Φ varies significantly within the timespan of the experiment, with $\Phi \approx 0$ and $\Phi \approx 1$ at various times, though T remains constant. This large variance and intermittency is characteristic of the system when $T \approx T_\Phi$, and similar phenomena are observed at other concentrations.

Figure 3.6 is the distribution of Φ's observed in Fig. 3.5, normalized to the total number of frames in the experiment. The broad range of the distribution is a characteristic of the system at $T \approx T_\Phi$.

Figure 3.7 is a plot of the variance in Φ versus T/T_Φ for the experimental system where $C = 0.052$. Note the significant peak at $T/T_\Phi \approx 1$. This peak at $T \approx T_\Phi$ is a characteristic behavior of the system at the transition, and it is also observed at other concentrations.

In order to directly compare T_Φ in our experiments and simulations, we rescale our experimental temperature using the expression

$$\tilde{T} = AT + B, \tag{3.6}$$

where A and B are constants to be determined. This method of rescaling is con-

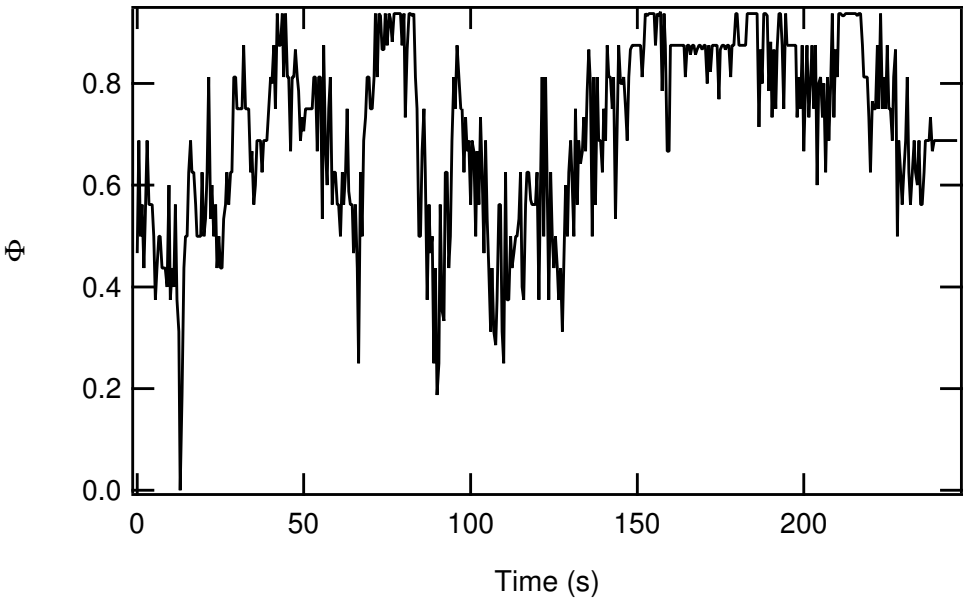

Fig. 3.5: A plot of Φ versus time for the experimental system where $C = 0.052$ and $T \approx T_\Phi$. Note the large variation in Φ, with $\Phi \approx 0$ and $\Phi \approx 1$ at various times, though T remains constant. This large variance and intermittency is characteristic of the system when $T \approx T_\Phi$.

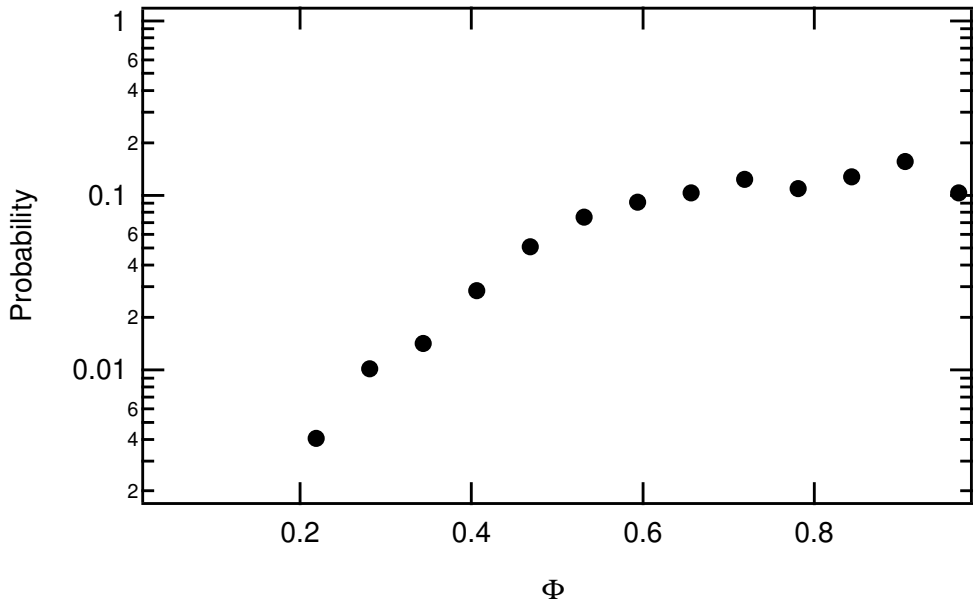

Fig. 3.6: A plot of the distribution of Φ's observed in Fig. 3.5, normalized to the total number of frames in the experiment. Note that the distribution is nonzero nearly over the entire range of Φ.

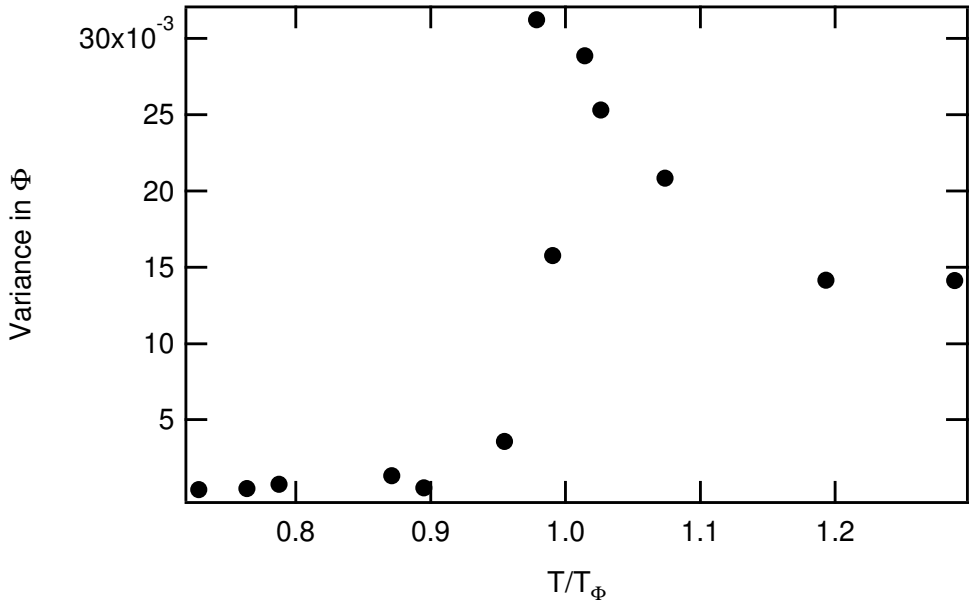

Fig. 3.7: A plot of the variance in Φ versus T/T_Φ for the experimental system where the concentration $C = 0.052$. Note the significant peak at $T/T_\Phi \approx 1$.

sistent with the thermal relation for vertically vibrated systems described in earlier work [44]. A and B are determined from a linear best fit to a plot of the T_Φ values from the experiment (at $C = 0.020$, 0.026, 0.039, 0.052, 0.078, and 0.104) vs. the T_Φ values from the simulation at similar C. For our experiments, $A = 13.798$ and $B = 0.15144$. Figure 3.8 shows the polymerization transition temperatures, T_Φ and $\tilde{T}_\Phi$ ($\tilde{T}_\Phi$ are the rescaled experimental T_Φ values), as a function C for the experiment (filled circles) and the simulation (open circles). Also, in Fig. 3.8 is a fit of the Dainton-Ivin equation [51] to the simulation data,

$$T_\Phi = \frac{\Delta h_p}{\Delta s_p + k_B ln C}, \tag{3.7}$$

where $\Delta h_p = -2.13 \pm 0.19$, and $\Delta s_p/k_B = -8.5 \pm 1.0$ (in units of particle self energy). A similar fit to the experimental data gives $\Delta h_p = -2.20 \pm 0.34$, and

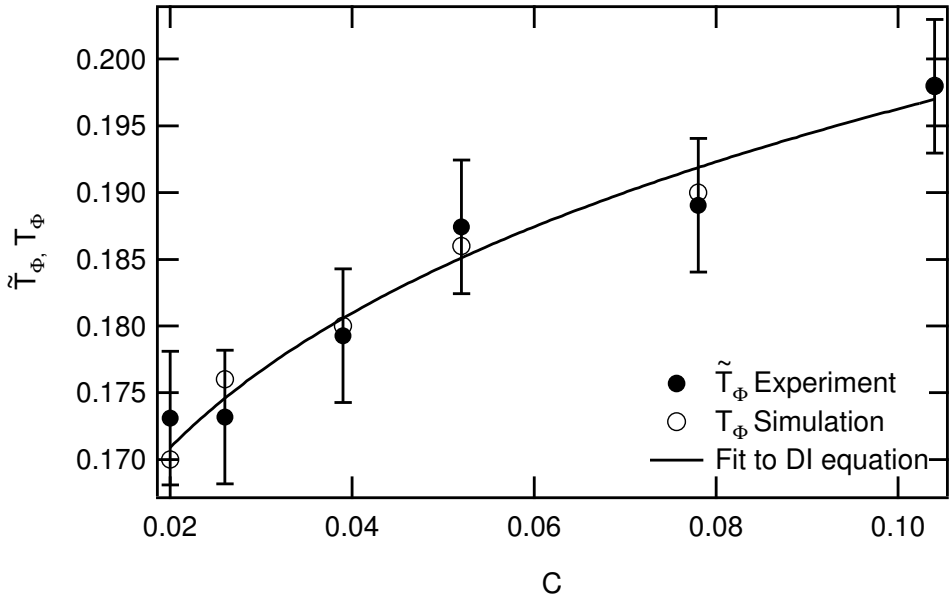

Fig. 3.8: T_Φ (open circles) and $\tilde{T}_\Phi$ (filled circles) versus the concentration C for the systems studied. Also plotted is a fit of T_Φ to the Dainton-Ivin equation.

$\Delta s_p/k_B = -8.9 \pm 1.8$. Note that T_Φ and $\tilde{T}_\Phi$ increase with increasing C, in a similar fashion for both the experiment and the simulation.

3.5 Conclusion

We have investigated the self-organization of dipolar spheres into chains as a fundamental model of the self-assembly of particles having anisotropic interparticle interactions. Our studies of a two-dimensional system of confined dipolar spheres has shown that there exists a polymerization transition of the spheres at finite temperatures. Using a simple model system of vertically vibrated magnetic spheres, together with Monte Carlo simulations of a similar system, carried out by collaborators at *NIST*, we showed that the transition temperature and the broadness of the

transition is concentration dependent. Our results show that the transition temperature, T_Φ, increases and the width of the transition broadens with increasing concentration, C, in accord with the analytic theory of equilibrium polymerization of Dudowicz et al. [48].

3.6 Outlook

Possible future work includes investigating the role of the system size in the transitions. This investigation could be done experimentally by building containers of different diameters and repeating the experiments at similar concentrations as those investigated above. Such studies would help determine what role the system size has on our results, and allow for better statistics in the case of larger systems.

It would also be interesting to investigate the role of higher order interactions on these transitions. Quadrupolar particles could be built, as discussed in Chapter 2, or the role of the octopole could be investigated by using cylindrical magnetic cores of differing lengths. These studied would give insight into the affects of higher order interactions on polymerization transitions, and may have specific implications for biological macromolecular self-assembly where higher order interactions are essential.

Another possible extension of this work is to build sturdier magnetic particles with weaker interactions so that higher relative temperatures can be investigated without destroying the particles.

4. PATTERN FORMATION IN A MONOLAYER OF MAGNETIC SPHERES

4.1 Overview

In this chapter, we report observations of pattern formation in our experimental system which depends on the shape of the magnetic core, i.e. the magnetic multipole moment distribution. While systems of dipolar spheres have been investigated relatively extensively [6, 7, 8, 9, 10, 11, 12, 26, 29, 30, 31, 34, 43], the roles of higher order moments in self-assembly are relatively unknown. Our results show that spheres containing short cylindrical magnets form HCP (hexagonal close-packed) macrovortices(Fig. 4.1(a)), while spheres containing long cylindrical magnets form concentric rings. This implies that the pattern formation depends not only on the dipolar moment, the temperature of the system, and the concentration of the spheres, but also on higher order multipole moments. In particular, because of the cylindrical symmetry of the magnetic cores, our work illustrates the effect of the octopole moment on the self-assembly.

Monte Carlo simulations of the thermal equilibrium of large 2D systems of hard spheres with centrally embedded point dipoles have shown that ordering in the absence of external forces depends on the dipolar strength, the temperature of

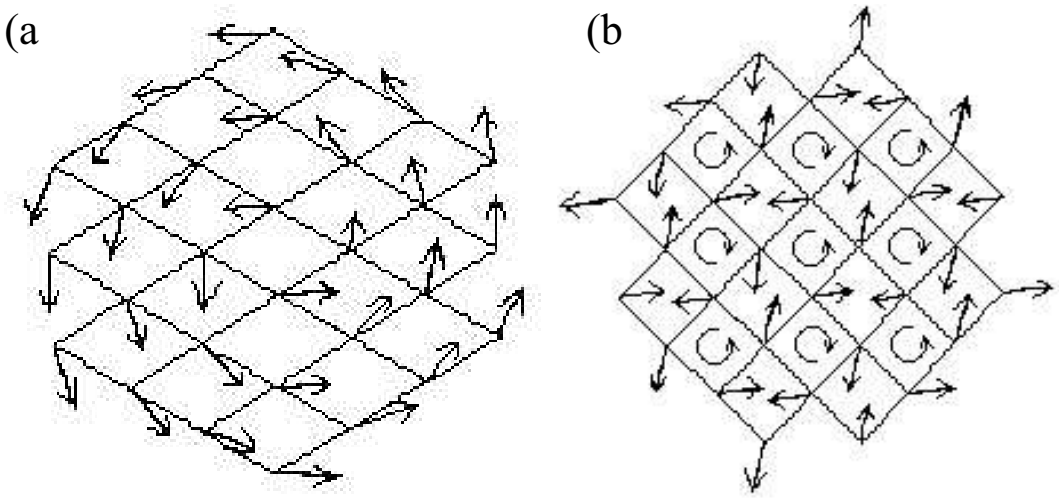

Fig. 4.1: (a) A schematic illustration of the 'HCP macrovortex' pattern. The dipoles are oriented in a macroscopic circulating vortical pattern about the center. (b) A schematic illustration of the 'square-packed microvortex' pattern. The dipole axes are tilted by about 45° with respect to the axes of the square pattern, and the dipole orientations are such that they define alternating directions of circulation (indicated by the rotational arrows in the centers of the squares) on a checker-board pattern of squares (after Ref. [52]).

the system, and the number density of the spheres [11, 29, 30, 31]. At intermediate temperature, high density systems of dipolar spheres form hexagonal-close-packed (HCP) macrovortices (Fig. 4.1(a)), while intermediate density systems form networks of long branching chains [29]. At high temperatures, systems of dipolar spheres disassociate and become gaseous [26, 29].

A calculation done by Belobrov *et al.* [52] showed that the zero-temperature ground state of a finite (< 500 particle) two-dimensional HCP lattice of dipoles is a macrovortex (Fig. 4.1(a)), while the zero-temperature ground state of a finite square-

packed lattice of dipoles is a microvortex (Fig. 4.1(b)). The microvortex state as a minimum of the interaction Hamiltonian, was also remarked upon by Rozenbaum et al. [53]. A similar macrovortex state seen at the atomic scale in 500 nm diameter thin magnetic films is also of significant current technological interest as a novel magnetic RAM material [16, 17, 18, 19, 20, 21, 22, 23]. The possibility of information storage in such systems occurs due to an ordered out of plane component of the atomic spins near the center of the macrovortex. While macrovortecies have been observed in magnetic thin films of thickness less than 30 nm, the out of plane ordering has been shown to vanish in the case of magnetic monolayers. The central out of plane dipole orientation is independent of the ordering of the rest of the macrovortex, and is easily flipped electronically, allowing for the possibility of two bits of memory storage for each micron-diameter disk. The macrovortex state was also observed in simulations of a dense system of dipolar spheres in thermal equilibrium [29], and in an experimental system of settled magnetic spheres (a system of magnetic spheres that are initially magnetically excited with a solenoid and then allowed to settle at the bottom of a container under zero external magnetic field) [15]. However, to our knowledge, a macrovortex pattern has never been observed in a finite temperature experimental system of dipolar spheres. We provide the first direct experimental demonstration of the macrovortex pattern in a thermalized system of dipolar spheres. We also provide a direct experimental visualization of a microvortex pattern in a zero temperature system of dipolar spheres.

4.2 Experimental Details

In the following experiments, we investigate particles encasing magnetic cores of two types which we call 'long' and 'short' magnets. The long magnets we used had length, $l = 1.42 \pm 0.01$ cm., and diameter, $d = 0.94 \pm 0.01$ cm. The short magnets we used had $l = 0.64 \pm 0.01$ cm. and $d = 0.95 \pm 0.01$ cm. Once the *long* magnets had been encapsulated in the spherical shells, the particles (*long* particles) were 5.3 ± 0.1 grams in mass, the maximum strength of the magnetic field on the surface of a long particle was 0.54 kG $\pm$16%. The particles containing the *short* magnets (*short* particles) were 4.3 ± 0.1 grams in mass, the maximum strength of the magnetic field on the surface of a short particle was 0.12 kG $\pm$24%. The short magnets were secured inside the plastic shells by filling the extra space in each half shell with RTV resin. All particles were constructed to have a light colored north hemisphere and a dark colored south hemisphere so that dipole orientations could be discerned. (Previous experiments on thermally or externally excited systems did not sense the dipole orientations of individual particles.) The container was constructed with a polyvinyl chloride bottom and N particles were placed in the container prior to vibration, to give a system concentration, C, as defined in Chapter 3. Typically, $0.30 < C < 0.65$. The system was imaged at a rate of 2 Hz for 500 frames with a 1024x1024 pixel camera. In these experiments, typical accelerations for the long particles were $4 - 8g$, while short particles were usually driven at about $2 - 5g$.

4.3 Results

Figure 4.2(a) shows the 'network' pattern of short particles where $C = 0.309$, after being shaken at $4.3g$ for 250 seconds. In this case (Fig. 4.2(a)), the initial state was created by pouring the particles randomly into the container. The observed chain-like structure is similar to the pattern observed by Blair *et al.* [26] in intermediate density systems of vertically vibrated magnetic spheres, and by Weis [29] in simulations of intermediate density systems of dipolar spheres. Figure 4.2(b) shows the configuration of short particles where $C = 0.618$ after being shaken at $4.3g$ for 250 seconds. The initial state of the particles was random. The final state of the particles after being driven is mostly an HCP macrovortex state similar to the ground state of a dipolar hexagonal lattice predicted by Belobrov *et al.* [52] (Fig. 4.1(a)) and seen in simulations by Weis [29]. We find that this HCP-based macrovortex is a stable state for the short particles. When other patterns such as square-packed microvortices (Fig. 4.1(b), 4.2(c)) or concentric rings are set up as the initial condition, after driving, the system always becomes an HCP-based macrovortex (Fig. 4.2(d)). If the system is set up as a macrovortex, it remains in a macrovortex state. Also, when several single chains of the particles are brought together in an antiferromagnetic square-packed state of 190 particles (each chain has the opposite dipolar orientation from that of the two neighboring chains), they immediately, without driving, reorient themselves into the microvortex state (Fig. 4.1(b), 4.2(c)). If the particles are initially set up in a ferromagnetic HCP pattern, under small ($2.4g$) agitation, the macrovortex state is assumed.

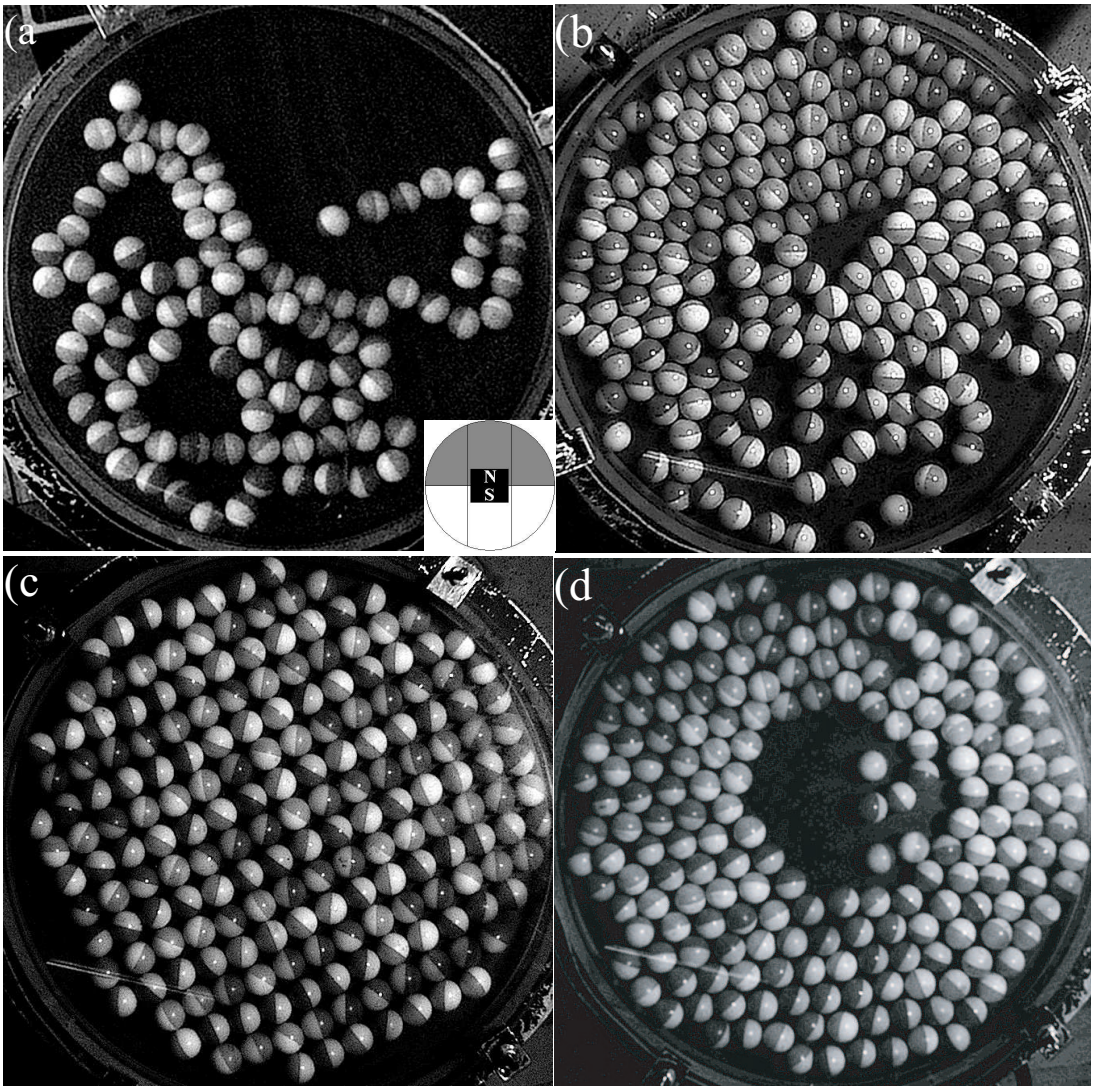

Fig. 4.2: (a) The network pattern of an intermediate density ($C = 0.309$) system of short particles after being shaken at $4.3g$ for 250 seconds. (b) The final macrovortex configuration of a dense ($C = 0.618$) system of short particles after being shaken at $4.3g$. (c) The microvortex pattern made by the square-packed set up, undriven, dense ($C = 0.618$) system of short particles. (d) A 'hollow macrovortex' configuration of the short particles after being set up in an aligned, concentric rings pattern and then shaken at $4.3g$.

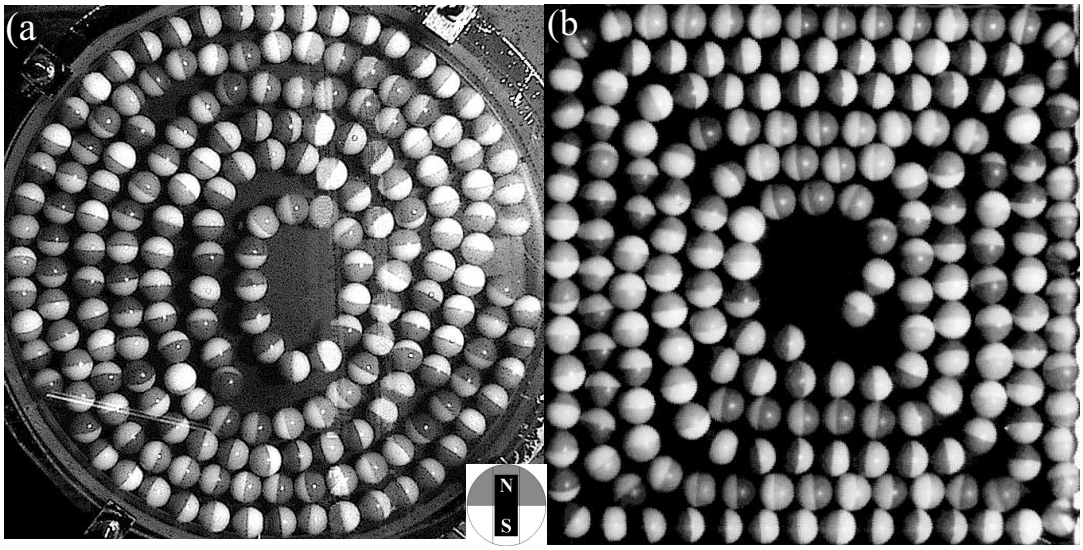

Fig. 4.3: (a) The final concentric ring state of a dense, $C = 0.618$, system of initially random long particles after being shaken at $7.8g$ for 250 seconds. (b) The final state of the system after being shaken in a square box at $7.8g$ for 250 seconds. The pattern is one of squared-off concentric rings, similar to the final state of the particles in the cylindrical container of equal height and area.

Figure 4.3(a) is the final concentric ring state of a $C = 0.618$ system of long particles after being shaken at $7.8g$. The initial state of the particles was random. The existence of the concentric ring state is independent of the initial conditions of the system. If the system is set up in any other state, it rearranges into a concentric ring state with sufficient driving. Systems of all lower densities also prefer ring and line states at intermediate and low accelerations ($< 8g$).

Figure 4.4(a) is the initial random state of a dense (190 particle) system of long particles. After 100 seconds of shaking at $7.8g$, the system evolves into the spiral pattern shown in Fig. 4.4 (b) (blue and red lines are superimposed upon the

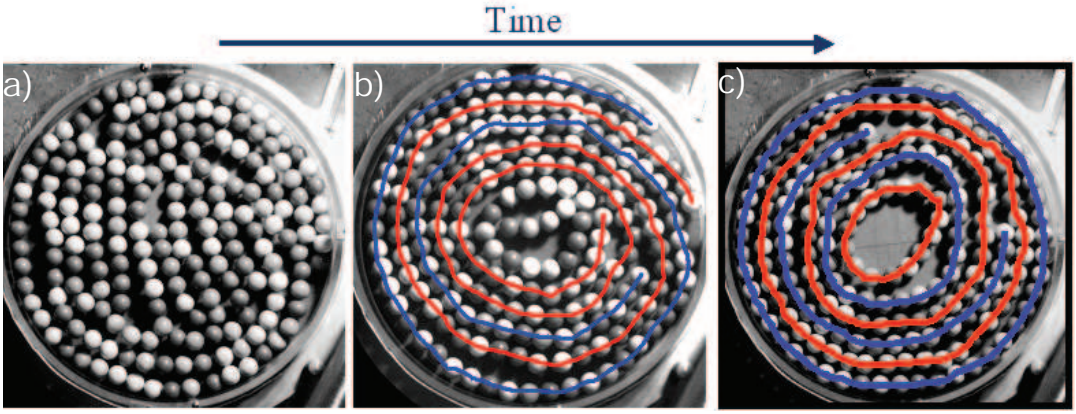

Fig. 4.4: (a) The initial random state of a dense (190 particle) system of long particles. (b) An intermediate state of the same system of long particles after shaking at 7.8g for 100 seconds. Note the spiral ordering that occurs (highlighted by blue and red drawn lines). (c) The final state of the system after 250 seconds, a steady state pattern of concentric rings, similar to that shown in Fig. 4.3.

pattern to highlight the spiral ordering). Figure 4.4(c) is the final state of the system after 250 seconds, a steady state pattern of concentric rings, similar to that shown in Fig. 4.3.

Figure 4.5 (a) is the initial state of an intermediate density ($C = 0.325$) system of long particles. The system quickly evolves to form chains of variable length (highlighted by red drawn lines) after 30 seconds of vibration at 6.4g, as shown in Fig. 4.5 (b). Figure 4.5 (c) is the final state of the system after 100 seconds, a steady state pattern of concentric rings, similar to that shown in Fig. 4.3 and Fig. 4.4 (c). Note the contrast in between the ring-like ordering of the long particles shown in Fig. 4.5 (c), and the network pattern formed by the system of short particles at similar density shown in Fig. 4.2 (a). The ring state is a robust steady state phe-

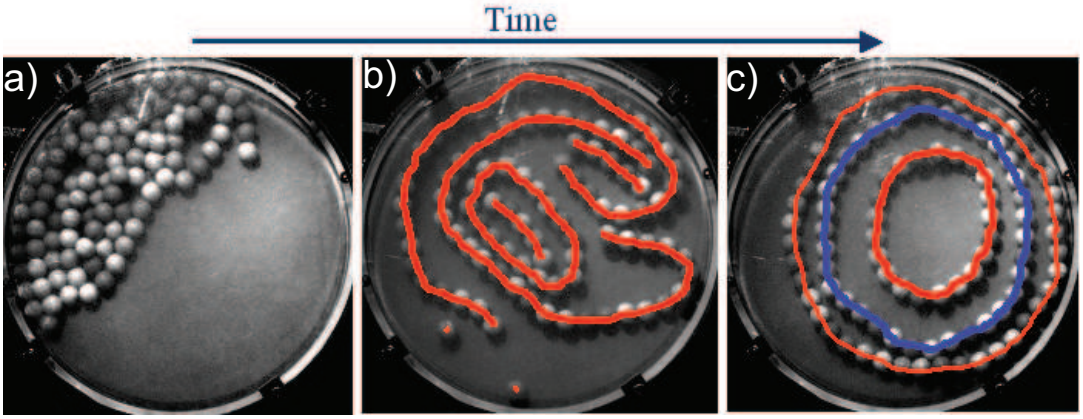

Fig. 4.5: (a) The initial state of an intermediate density ($C = 0.325$) system of long particles. (b) An intermediate state of the same system of long particles after shaking at $6.4g$ for 30 seconds. Note the appearance of long chains. (highlighted by red drawn lines). (c) The final state of the system after 100 seconds, a steady state pattern of concentric rings, similar to that shown in Fig. 4.3 and Fig. 4.4. Note that the ring state is a robust steady state phenomenon for the long particles, reproducibly appearing at several different particle densities and in different shaped containers.

nomenon for the long particles, reproducibly appearing at several different particle densities and in different shaped containers, as illustrated in Figs. 4.3, 4.4, and 4.5.

We can track the positions of all particles during our experiments, using digital image algorithms developed in the *IDL* programming environment. To gauge quantitatively how much HCP clustering occurred in each experiment, we designed a program that finds the number of particles with 6 touching neighbors in each image. The program identifies particles as 'touching' if the centers of the particles are within 9/8 particle diameters of each other. We found that for a system of 190 short

particles ($C = 0.618$) initially in a random state and then shaken at $4.3g$, the mean number of particles with 6 touching neighbors, N_6 , averaged over 500 frames, was 43.3 ± 9.0. For 190 initially random long particles shaken at 7.8g, $N_6 = 0.14 \pm .09$. In these two experiments, where 190 particles began in a random state, the N_6 of the short particles was more than 300 times the N_6 of the long particles. Using this measure, in all experiments with similar initial conditions, the short particles were quantitatively more clustered than the long particles.

Boundary conditions do not appear to affect the qualitative features of the final states for either type of particle. We performed similar experiments in a square box of height and area equal to those of the cylindrical container, and the final states were always qualitatively similar to the final state in the cylindrical container. For example, see Fig. 4.3(b), which shows the state of a $C = 0.618$ system of long particles after shaking in the square box under similar initial conditions as for Fig. 4.3(a).

4.4 Energetic Considerations

To gain insight into the reasons why the long particles form different patterns than the short particles, we numerically examined the theoretical model described in Chapter 2 with $w \to 0$. This model is similar to that used in simulations by Schneider *et al.* [27] to model lipid headgroups (which are also dipolar), and it gives qualitatively similar results to the two-parallel-dipole model used by Camp *et al.* [54]. Similar three point charge models are used to match charge, dipole and quadrupole

moments of polar molecular systems such as hydrogen fluoride for simulations [24]. Our model also reduces to a central point dipole model as $h/D \to 0$.

We use the usual Coulomb energy formula,

$$U_{ij} = \frac{\mu_0}{4\pi} \frac{q_i q_j}{R_{ij}} \tag{4.1}$$

(similar to Eq. 3.2 in Chapter 3) and sum over all interparticle pairs of charges to obtain the energy of a pattern of particles (excluding the energy of pairs of charges within the same particle). When we take the limit $h/D \to 0$, our calculations are consistent with the energy calculations of rings and lines of spheres containing single point dipoles done by Clarke *et al.* [25].

It is interesting to note that, assuming the dipole moments are aligned with the z axis, while $P_{0.75}/P_{0.001} = 1$ by design (where $P_{h/D}$ is the z component of the dipole moment of a model particle with a given value of h/D, the ratio of the zzz components of the octopole moments, $O_{0.75}/O_{0.001} = 562500$. Because the zzz component of the octopole moment is the highest order differing term, it is likely the most important differing moment for models of different h/D for small h/D.

In Fig. 4.6, we have plotted the energies of two touching particles as the angle between their axes is symmetrically bent for several values of h/D. Note that the slope of the curves increases as h/D increases. This indicates that chains of particles with large h/D are stiffer than those with small h/D. Also note that at $\Theta = 0$, the particles are in the head-to-tail configuration and at $\Theta = \pi/2$, the particles are in the antialigned side-to-side configuration. For large h/D, the head-to-tail ($\Theta = 0$) configuration is much more favorable than the antialigned side-to-side ($\Theta = \pi/2$)

configuration (e.g. for $h/D = 0.75$, the head-to-tail energy is more than 6 times the antialigned side-to-side energy). For $h/D = 0.001$, the head-to-tail energy is only twice the antialigned side-to-side energy. This fact is elucidated by plotting the ratio of the energy of two particles in head-to-tail alignment, E_{HT} to the energy of two particles in an antiparallel side-to-side alignment, E_{SS}, versus h/D, as is shown inf Figure 4.7. This indicates that, as the distance between the charges increases, the relative importance of the side-to-side interaction decreases. Particles with large h/D (e.g., our long particles) have a strong preference to align head-to-tail, while particles with small h/D (e.g., our short particles) do not. This is in contrast to recent models of dipolar 'spherocylinders' (cylinders with hemispherical ends) which encapsulate a single centrally located point dipole [56, 57]. These spherocylindrical particles increase the relative importance of side-to-side interactions.

Figure 4.8 is a plot of the energy gained by bringing together ten 10-particle chains in various patterns normalized to the energy of ten infinitely separated 10-particle chains versus h/D. At low h/D (< 0.19), the lowest energy state is the HCP macrovortex (as predicted by Belobrov et al. [52] for $h/D = 0$ particles). At $h/D > 0.19$, the particles energetically prefer a ring state. This is consistent with our observations of high density systems; particles with short cylindrical magnetic cores form a macrovortex (Fig. 4.2(b)), while particles with long magnetic cores form rings (Fig. 4.3(a)). Also, the orientations of the long particles in each ring appear to be independent of the orientations of the particles in neighboring rings. The square-packed microvortex state is more favorable than the square-packed antiferromagnetic arrangement only at very small h/D (< 0.1). This is also consistent

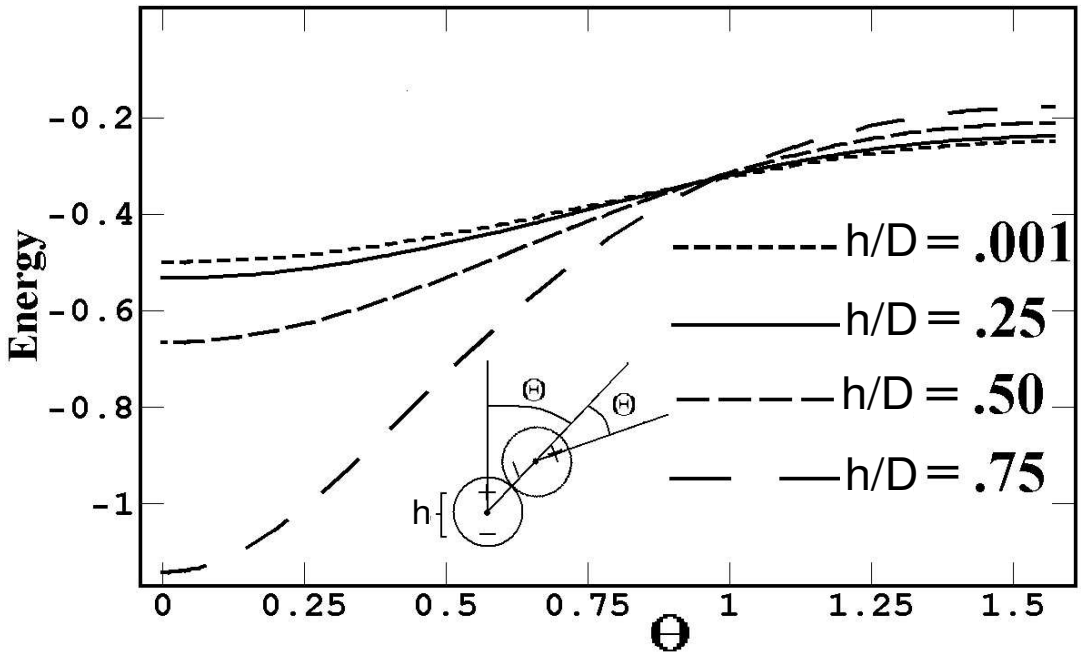

Fig. 4.6: The energies in units of $\frac{q^2h^2\mu_0}{D^3\pi}$ of two touching particles as a function of the angle Θ between their axes for several values of h/D.

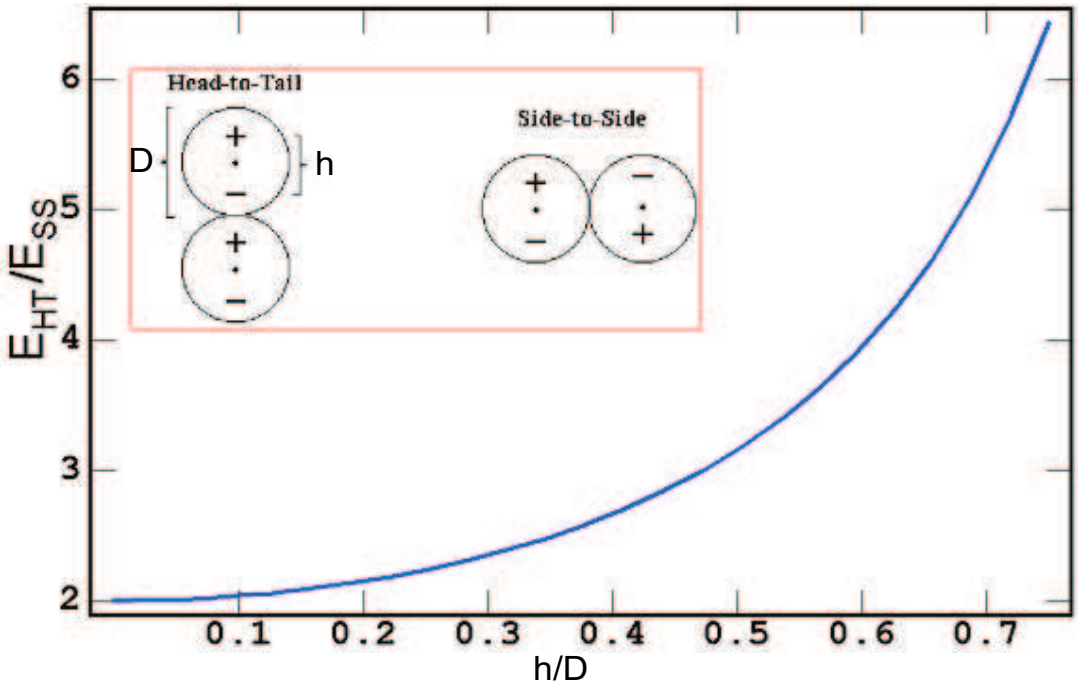

Fig. 4.7: The ratio of the energy of two particles in head-to-tail alignment, E_{HT} to the energy of two particles in an antiparallel side-to-side alignment, E_{SS}, versus h/D. Note that particles with large h/D strongly prefer a head-to-tail alignment (with $E_{HT}/E_{SS} \approx 6$ at $h/D = 0.7$), while particles with smaller h/D have relatively little preference.

with our observations. When we attempt to set up the short particles in a square-packed antiferromagnetic pattern, they immediately, without driving, reorient into a microvortex pattern. The long particles never form a microvortex pattern when set up in a square-packed antiferromagnetic state, even when driven. The HCP ferromagnetic state is energetically unfavorable compared to separated lines at all h/D. This is in contrast to the result for an *infinite* HCP lattice, in which case the *ground state* is ferromagnetic [58]. It is also interesting to note that the ground state of an HCP lattice of magnetic dipoles can change under an external tangential magnetic field. Bologa *et al.* [15] observed a transition in an unexcited system of magnetic spheres from an HCP macrovortex state to an HCP ferromagnetic state under an increasing external tangential magnetic field.

We conclude that particles with a large h/D, such as our long particles, are more likely to form long, stiff, weakly interacting chains and rings. Particles with small h/D are more likely to aggregate into clustered patterns. Energetically, it has been shown that the ground state of a hexagonal lattice of point dipoles is a macrovortex [52]. It has also been shown that for systems of between 4 and 13 (point) dipolar particles, the global ground state is a single ring [25]. For a system of 14 or more dipolar spheres, a 'double ring state' has lower energy, and it is expected that the lowest energy configuration changes once again to triple, quadruple, and higher order ring states as the number of particles increases. We conjecture that, as the number of particles increases, the global ground state may begin to look like a 'hollow macrovortex', similar to that in Fig. 4.2(d).

Figure 4.9 is a plot of the energies (normalized to the energy of $\sqrt{N}$ infinitely

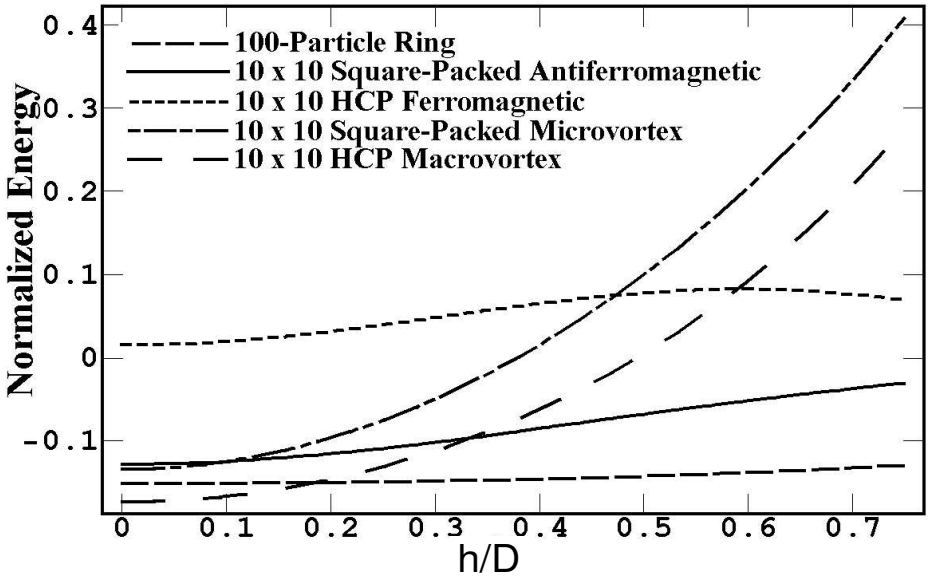

Fig. 4.8: The energy of ten 10-particle chains brought together in various patterns normalized to the energy of ten infinitely separated 10-particle lines versus h/D. The energy of two infinitely separated 10-particle lines is normalized to 0 for all h/D. Note that the HCP macrovortex is the lowest energy conformation only for $h/D < 0.19$; for $h/D > 0.19$, a single 100-particle ring state is of lower energy.

separated chains of length $\sqrt{N}$) of several different patterns of dipolar ($h = 0.001$) particles versus $\sqrt{N}$. All patterns except the ring pattern are rectangular lattices of dimensions N particles by N particles. Note that the ring state is energetically preferred for $\sqrt{N} < 9$, while for $\sqrt{N} \geq 9$ the HCP macrovortex is preferred. It is also interesting to note that while the normalized energy of the HCP macrovortex steadily increases for $\sqrt{N} > 20$, the normalized energy of the HCP ferromagnetic pattern decreases. By taking a linear best fit to the final four data points of both the HCP patterns, and extrapolating to higher $\sqrt{N}$, we predict the ferromagnetic state to be of lower energy at $\sqrt{N} \approx 105$. It is well-known that there is a transition from macrovortex to ferromagnetic ordering in an HCP dipolar lattice for large N [52, 58], and our calculations suggest the transition would occur at $N \approx 11000$.

Figure 4.10is a plot of the energies (normalized to the energy of $\sqrt{N}$ infinitely separated chains of length $\sqrt{N}$) of several different patterns of $h = 0.69$ model particles versus $\sqrt{N}$. All patterns except the ring pattern are rectangular lattices of dimensions N particles by N particles. Note that the ring state is energetically preferred for all calculated values of $N > 2$, while the microvortex and macrovortex patterns are highly unfavorable, in contrast to the favored patterns of the $h = 0.001$ dipolar particles as shown in Fig. 4.9.

4.5 Conclusions

Our experimental and theoretical results show that the shape of the magnetic core in particles can be a determining factor in pattern formation, even in simple systems.

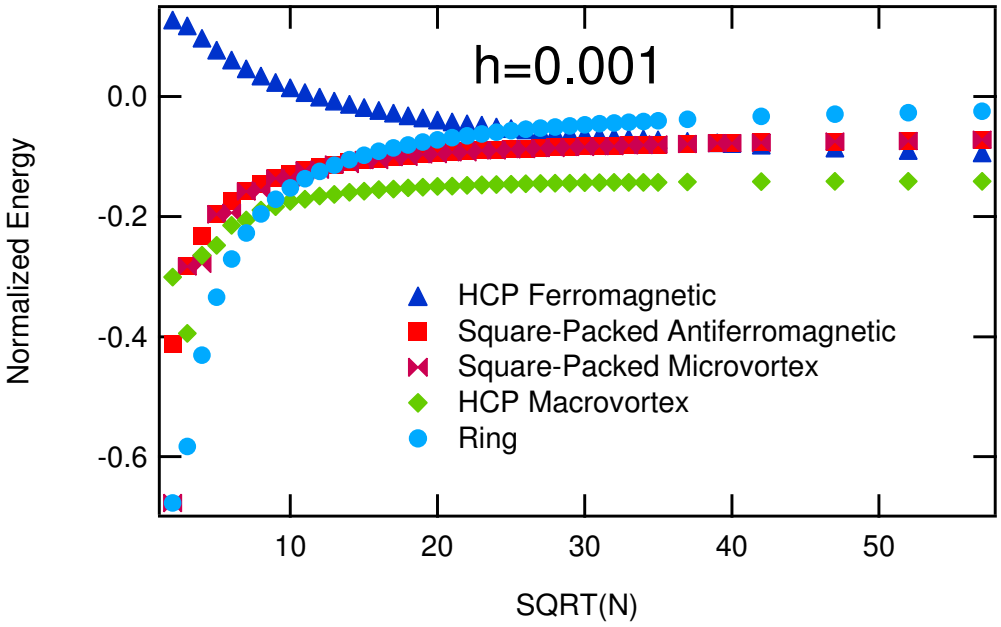

Fig. 4.9: A plot of the energies (normalized to the energy of $\sqrt{N}$ infinitely separated chains of length $\sqrt{N}$) of several different patterns of dipolar ($h = 0.001$) particles versus $\sqrt{N}$. All patterns except the ring pattern are rectangular lattices of dimensions N particles by N particles. Note that the ring state is energetically preferred for $\sqrt{N} < 9$, while for $\sqrt{N} \geq 9$ the HCP macrovortex is preferred.

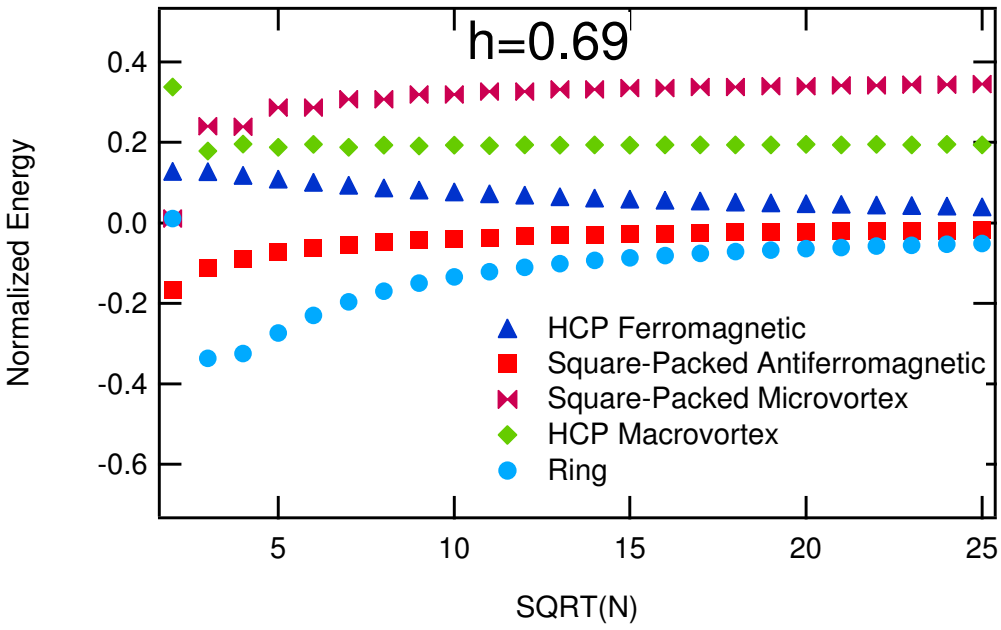

Fig. 4.10: A plot of the energies (normalized to the energy of $\sqrt{N}$ infinitely separated chains of length $\sqrt{N}$) of several different patterns of $h = 0.69$ model particles versus $\sqrt{N}$. All patterns except the ring pattern are rectangular lattices of dimensions N particles by N particles. Note that the ring state is energetically preferred for all calculated values of $N > 2$, while the microvortex and macrovortex patterns are highly unfavorable, in contrast to the favored patterns of the $h = 0.001$ dipolar particles as shown in Fig. 4.9.

As h/D increases, the energetically favored pattern changes qualitatively. Indeed, as $h/D \to 1$ in our model, the head-to-tail arrangement of the dipoles becomes infinitely more favorable than any other configuration. Our unique particles allow us to provide the first direct experimental evidence of the square-packed microvortex pattern in a zero temperature system of dipolar spheres, and the first observations of an HCP macrovortex state in an excited system of dipolar spheres. Finally, we note that the observed patterns can be understood as either minimum magnetostatic energy equilibria (in the macrovortex and microvortex cases) or (in the case of low density network patterns, Fig. 4.2(a)) as thermal equilibrium states.

4.6 Outlook

Possible future work includes studies of larger systems of particles with which orientations can be discerned. This could be achieved by building larger, lightweight containers that could be vibrated on a shaker similar to the one used here. Investigations of larger systems would allow for better statistics, but more importantly, it is possible that the qualitative features of the observed patterns could change in large systems. Specifically, for dipolar particles (without higher order interactions), it has been shown that the favored pattern of an HCP lattice is ferromagnetic for large systems, and vortex for small systems [52, 58].

It would also be interesting to study similar systems in 3D. One possible method of investigating 3D systems experimentally would be to build colloidal magnetic particles with variable field shapes, and density match them to a surrounding

fluid. Thermal energy could then provide the excitation force, rather than shaking. It may be simpler to build larger density-matched magnetic particles, and then excite them with an AC magnetic field imparted by a soleniod, similar to the method used by Bologa et al. [15].

5. SEGREGATION IN A MONOLAYER OF MAGNETIC SPHERES

5.1 Overview

In this chapter, we show using our experimental system, that in dilute systems, the long particles can form a loose unbranched network pattern. If the multipole moment distribution of a small fraction of the magnetic particles is altered, we show there is a significant increase in the branching of the self-assembled network. We also show that magnetic spheres of equal magnetic field strength can segregate due only to differences in their field shape. We find that the segregation increases approximately linearly with acceleration over the acceleration range studied. We also present evidence that systems of vertically vibrated magnetic spheres of equal mass, size, and surface properties can segregate due only to differences in the particles' magnetic field strengths. The observed segregation is shown to increase with the proportion of weaker particles, and it also increases approximately linearly with acceleration over the acceleration range studied. Finally, we show that the segregation is accompanied by a significant decrease in magnetic energy.

Segregation in binary mixtures of excited granular material is a widely observed phenomenon [59]. Segregation due to differences in size [39, 40, 60], shape [61,

62], density, and particle surface properties [39] has been observed to occur under various circumstances. In particular, there is significant current interest in the segregation and mixing of wet granular mixtures as an example of segregation among mutually attractive particles [39, 40]. In granular systems, the addition of attractive forces between particles has been observed to both cause and prevent segregation under different circumstances [39]. Recent observations have also been made on pattern formation in systems of dry magnetic spheres, as an investigation of an anisotropically attractive granular material [26, 41]. Blair and Kudrolli [26] found that, in a vertically vibrated 2D mixture of magnetic and non-magnetic granular spheres, the magnetic spheres can self organize and cluster, depending on the volume fraction of magnetic particles and on the relative strength of the magnetic dipole-dipole interaction to the external vibration amplitude. In our earlier work [41], we showed that the shape of the magnetic field also influences into what pattern the beads self-assemble.

In addition to the previous work on vertically vibrated magnetic granular spheres [26, 41], several groups have investigated vertically vibrated monolayers of unmagnetized granular particles [63, 64, 65]. However, the behavior of binary systems of granular matter that differs only in the shape or strength of the interaction potential, to our knowledge, has not been investigated. The results described in this chapter can therefore either be viewed as an investigation of a novel binary granular material with anisotropic interactions, or as a simple model system of a binary dipolar fluid.

5.2 Experimental Details

Figure 5.1 is a schematic of the magnetic particles used for this chapter. We investigate particles encasing magnetic cores of three types which we call 'weak', 'strong', and 'long' magnets. The properties of all particles are shown in table 5.1. The *weak* particles have nearly identical shape, size, and mass as the *strong* particles, with the only relevant differing property being their relative *magnetic strengths* (measured as the maximum magnetic field on the surface of an isolated sphere). The *strong* and *long* particles have comparable magnetic strengths and are nearly identical in shape, size, and mass, with the only relevant differing property being their magnetic core shapes, i.e. their *magnetic field shapes*. The strong and weak magnets were encapsulated with non-magnetic filler of appropriate size and mass so that the magnets were centrally located and the finished particles were identical in mass. For each strong and weak particle, the non-magnetic filler consisted of two pieces of hollow cylindrical brass tubing with inner and outer diameters and lengths such that the magnets were rigidly fixed and centrally located, and the final masses were well matched to those of the long particles.

The container was constructed with a black Delrin bottom and a mixture of two types of particles was placed in the container so that the particles were well mixed, i.e. there were relatively small numbers of like-particle contacts prior to vibration. a was varied from $4g$ to $10g$ and the system was imaged from above at a rate of 1 Hz with a 1280x1024 pixel color camera.

Tab. 5.1: A table of particle properties.

Particle Name	Colors (North/South)	Mass (g)	Strength (kG)[a]	P_z^b	O_{zzz}	l (cm)	Magnet Material
Weak	White/Yellow	5.4 ± 0.1	0.22 ± 0.03	1.0 ± 0.1	1.0 ± 0.1	0.52 ± 0.1	Ceramic
Strong	Blue/Green	5.4 ± 0.1	0.60 ± 0.08	2.7 ± 0.4	2.6 ± 0.4	0.51 ± 0.1	NdFeB
Long	Yellow/Green or Yellow	5.3 ± 0.1	0.54 ± 0.09	2.2 ± 0.3	17 ± 3	1.42 ± 0.1	Ceramic

[a] Measured as the maximum surface field on an isolated particle.

[b] Where the z axis is parallel to the line connecting the poles, with the origin at the particle center. Moments are calculated using the magnetic strength and the core shape, and are normalized by moments of a Weak particle.

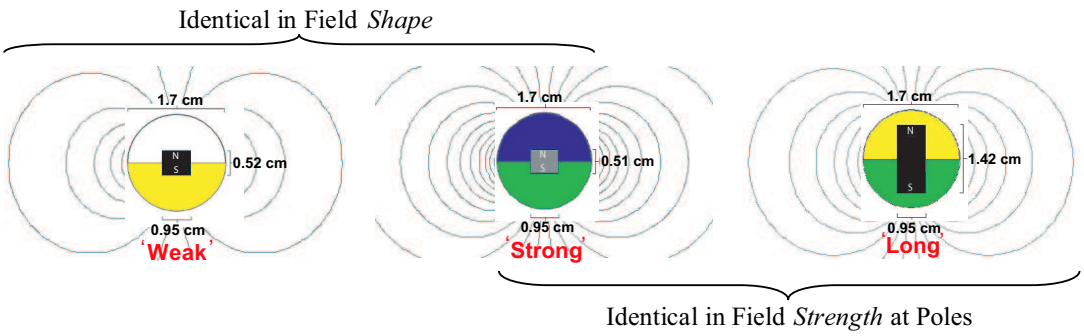

Fig. 5.1: A schematic of the magnetic particles used, together with a qualitative illustration of their respective magnetic field lines (obtained using *Vizimag* software).

5.3 Results

Figure 5.2 is a representative image a system of 2 strong and 55 long particles during vibration. Note that 3 to 4-fold branching occurs around the short particles, while branching is uncommon amongst the long particles. The presence of a relatively small number of strong particles significantly increases the branching in the network pattern.

In systems of larger mixture fractions, a different pattern is manifest. As an example of the observed patterns, Fig. 5.3(a) shows the mixed initial state of 88 weak and 23 strong particles. The initial state was made to have a low number of like-particle contacts. Figure 5.3(b) is the final state of the system in Fig. 5.3(a) after being shaken at $9.0g$ for 300 seconds. The final configuration (Fig. 5.3(b)) is highly segregated, with all strong blue/green (dark/dark in grayscale) particles in two dense clumps, and the weak white/yellow (light/light in grayscale) particles forming a loose, branching network pattern. The evolution of this system as shown

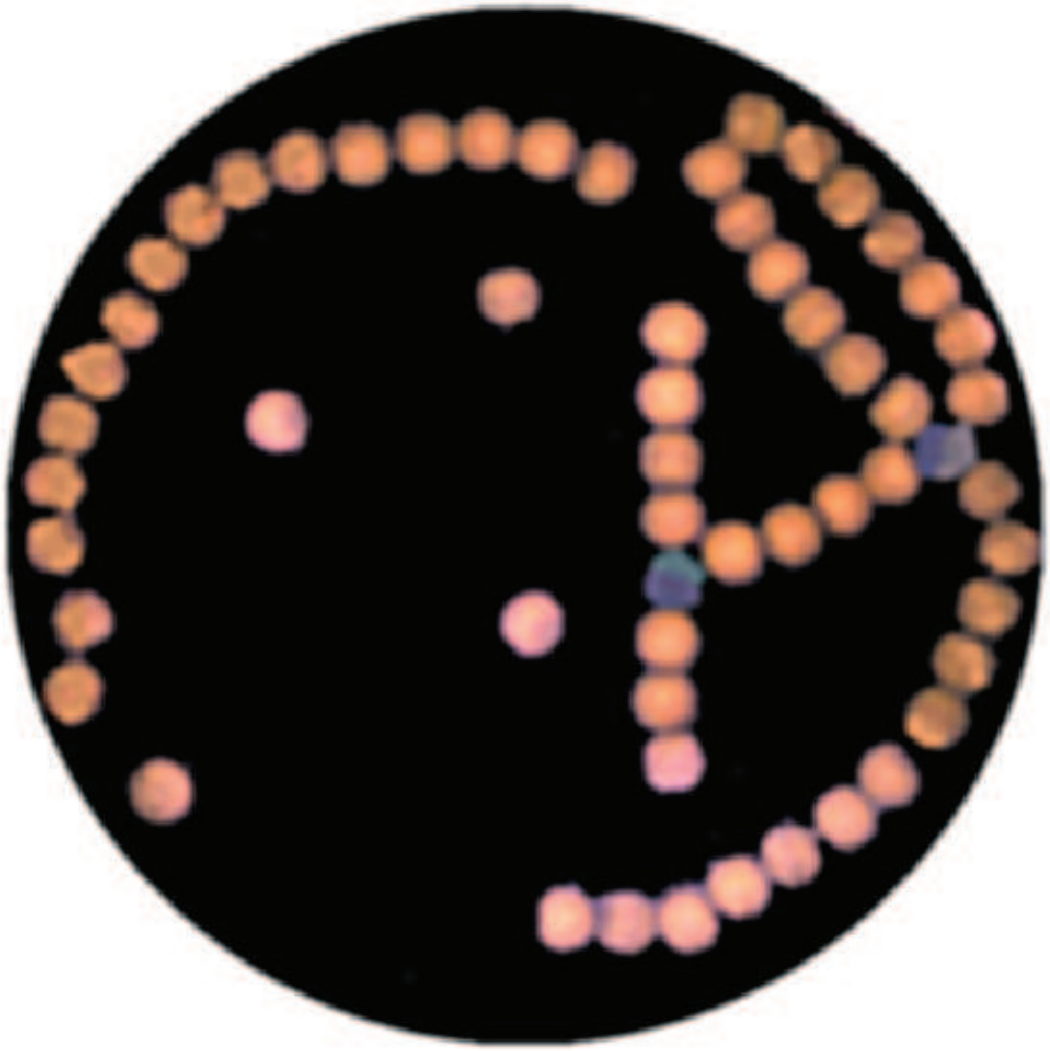

Fig. 5.2: A representative image of a system of 2 strong (blue/green) and 55 long (solid yellow) particles during vibration at $8.6g$. Note that 3 to 4-fold branching occurs around the short particles, while branching is uncommon amongst the long particles.

in Figs. 5.3(a) and (b) indicates that systems of otherwise identical magnetic spheres can segregate due solely to differences in magnetic field strength.

A mixed initial state of 51 strong blue/green, and 59 long yellow/green (light/dark in grayscale) particles is shown in Fig. 5.4(a). After 300 seconds of excitation at $9.6g$, the system evolves into the configuration shown in Fig. 5.4(b). The final state (Fig. 5.4(b)) is well segregated, with the strong particles having a tendency toward hexagonal-close-packed (HCP) clumps, and the long particles in long unbranched chains. The strong particles roughly tend toward HCP clumps while the long particles form long, unbranching chains as a consequence of their differences in magnetic field shape, as has been remarked upon earlier in a study of pattern formation in monodisperse 2D systems of magnetic spheres [41]. As evidenced in Figs. 5.4(a) and (b), systems of otherwise identical magnetic spheres can segregate due solely to differences in magnetic field shape.

For further analysis, we track the positions, 3D dipole orientations, and particle types of all particles during our experiments. To quantify the segregation in each system, we designed a program that finds all particle-particle contacts in every image. The program identifies particles as 'in contact' if the centers of the particles are within 9/8 particle diameters of each other. We tested different cutoff values and found that our results do not qualitatively depend on the cutoff. We then define a segregation parameter for each image,

$$S = \frac{C_{AA}}{C_{AA} + C_{AB}} + \frac{C_{BB}}{C_{BB} + C_{AB}}, \tag{5.1}$$

where C_{ij} is the total number of 'contacts' between particles of type i and particles of

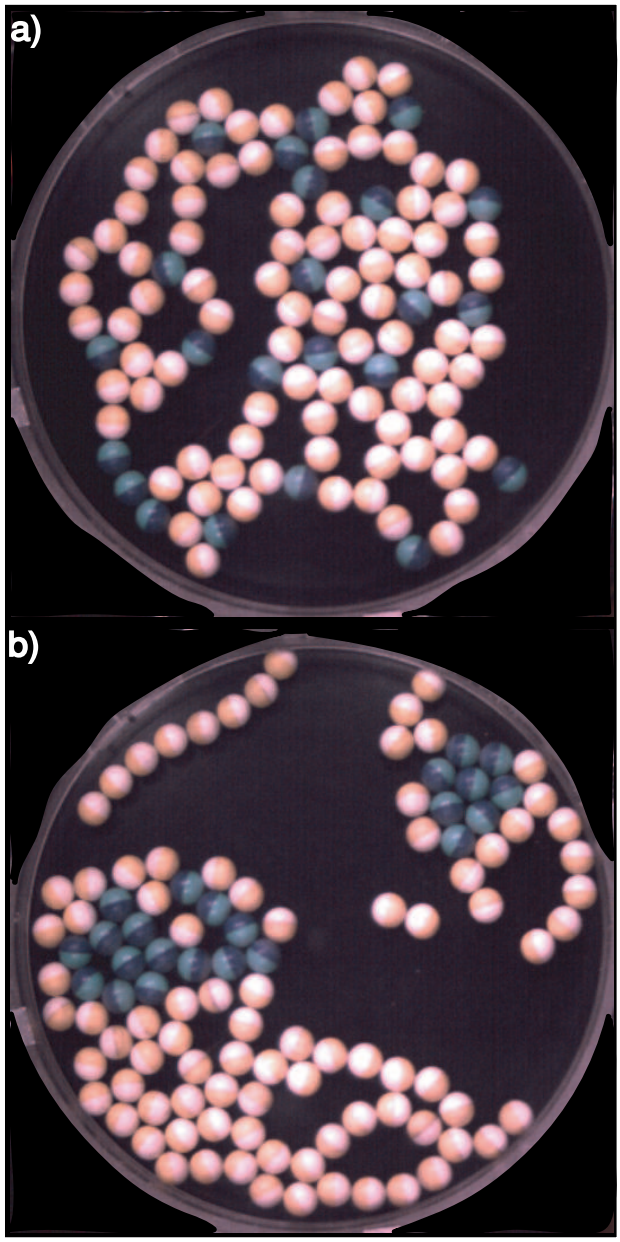

Fig. 5.3: (a) The mixed initial state of a system of 88 weak (white/yellow, light/light in grayscale) and 23 strong (blue/green, dark/dark in grayscale) particles. (b) The final segregated state of the 88 weak and 23 strong particles after being shaken at 9.0g for 300 seconds. Note that there are two dense clumps of the strong particles, while the weak particles form a loose network pattern.

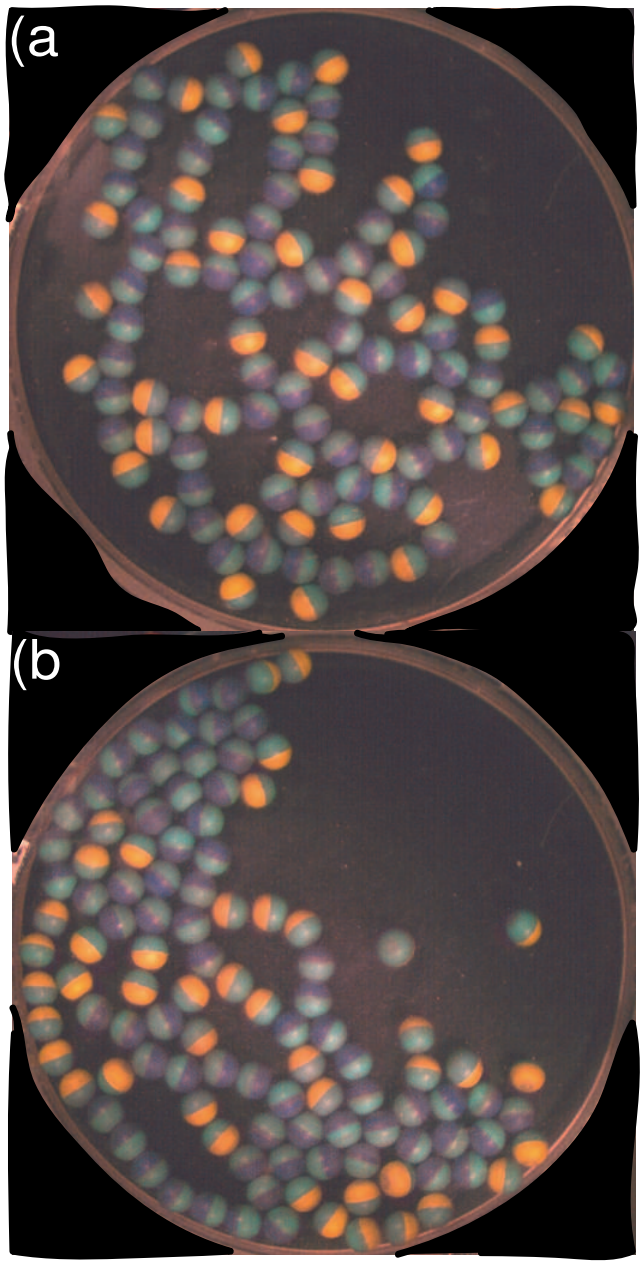

Fig. 5.4: (a) The mixed initial state of a system of 51 strong (blue/green, dark/dark in grayscale) and 59 long (yellow/green, light/dark in grayscale) particles. (b) The final state of the 51 strong and 59 weak particles after being shaken at $9.6g$ for 300 seconds. Note that the strong particles are largely in clusters and segregated from the long particles, which form long unbranching chains.

type j in the image (A and B are particle type labels). This segregation measure has the advantages of symmetry under interchange of particle type and equal weighting of the segregation of each particle type. $0 \leq S \leq 2$, and $S = 1$, on average, for random mixtures of all mixture ratios.

That $S = 1$ for random mixtures of all mixture ratios, can be seen by examining the probabilities of contacts of each type:

$$p_{ij} = \begin{cases} \frac{N_i}{N_i+N_j-1}, & i \neq j \\ \frac{N_i-1}{N_i+N_j-1}, & i = j \end{cases}$$

where p_{ij} is the probability that a contact associated with a particle of type i is with a particle of type j, and N_i is the total number of particles of type i in a system. So, on average,

$$C_{ij} = \kappa N_i p_{ij}, \tag{5.2}$$

where κ is the mean number of contacts per particle; hence, $S = 1$.

Figure 5.5(a) is a plot of S versus time for a single trial of the 88 weak/23 strong system shown in Fig. 5.3. S increases from an initial value, 0.86, to a final value, 1.48, indicating that the system began in a state which was '*supermixed,*' (since we intentionally placed unlike beads next to each other), i.e., more mixed than a random mixture ($S < 1$), and evolved into a segregated state ($S > 1$). Figure 5.5(b) is a plot of S versus time for a single trial of the 51 strong/59 long system in Fig. 5.4. S increases from an initial value, 0.88, to a final value, 1.39, again indicating that the system evolved from a mixed state to a segregated state. While trials with similar particle mixtures and acceleration amplitudes but differing initial

conditions showed similar qualitative long time segregation behavior, the short time behavior of S versus time varied significantly in different trials.

To compare the degree of segregation of different systems after 300 seconds, we define a parameter, S_f, as the mean of S over the final 20 seconds of a 300 second-long experiment. Figure 5.6 (a) is a plot of S_f versus the strong particle fraction for strong/weak systems of 111 particles driven at $9.0g$ (error bars are shown as one standard deviation of S, calculated over the final 20 seconds of a single experiment). S_f decreases as the fraction of strong particles is increased. Figure 5.6 (b) is a plot of S_f versus acceleration, a/g, for a system of 67 weak and 44 strong particles (filled circles) and a system of 67 strong and 44 long particles (filled triangles). S_f increases roughly linearly with acceleration for both systems. Note also, there are several data points in Fig. 5.6 (b), where $S_f < 1$, indicating that, after 300 seconds, the systems were supermixed. This is not an indication that the systems prefer a supermixed state; rather, it is due both to the fact that the systems began in a supermixed state and to the particles' lack of mobility. The particles' lack of mobility at low accelerations is likely because the average input (driving) energy is less than the magnetic particle-particle interaction energy. In no case, for any of our systems, have we observed a significant, non-transient decrease in S in time.

5.4 Energetic Considerations

To gain insight into the cause of the observed segregation, we numerically examined the magnetic particle model described in Chapter 2. We vary q with h so that the

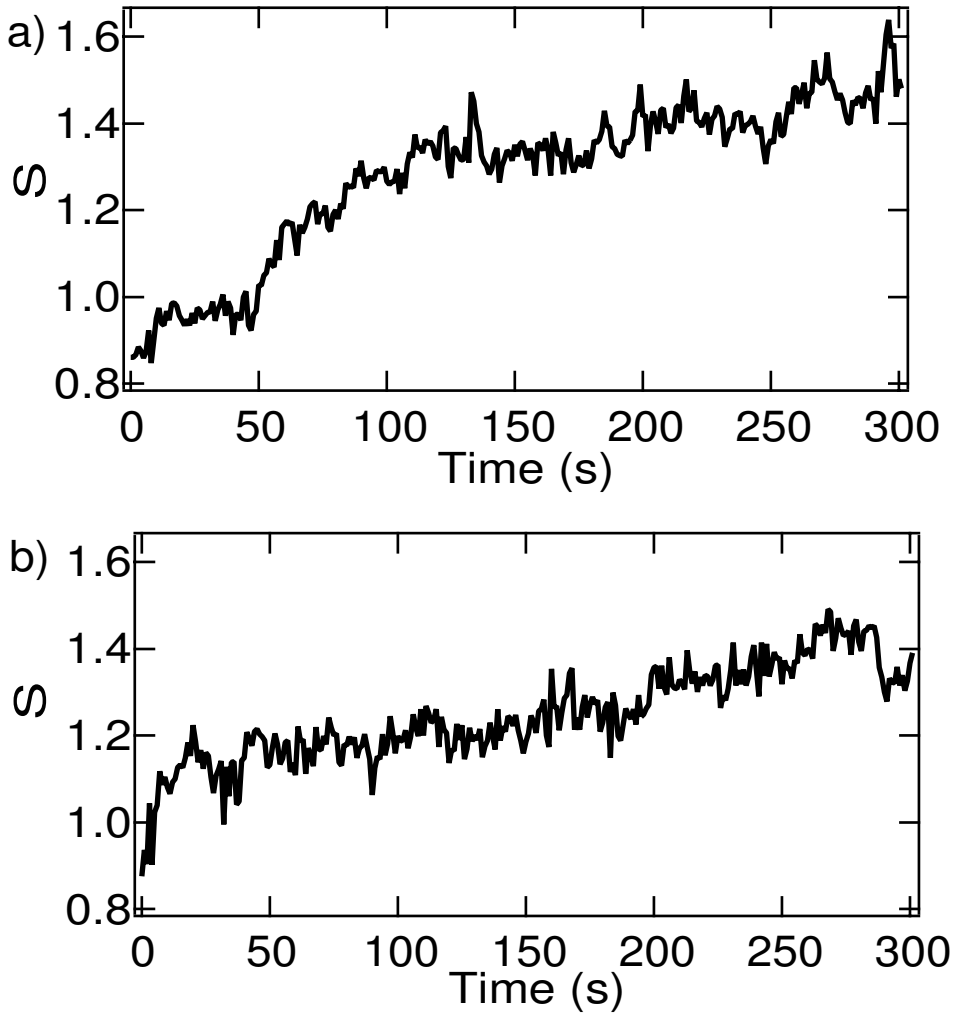

Fig. 5.5: a) The segregation, S, versus time for the system of 88 weak and 23 strong particles shown in Fig. 5.3. Note that S increases significantly over time, and it is greater than 1 (the S of a randomly mixed system) at the end of the experiment. b) S versus time for the system of 51 strong and 59 long particles shown in Fig. 5.4. Note that S again increases significantly over time, and it is greater than 1 at the end of the experiment

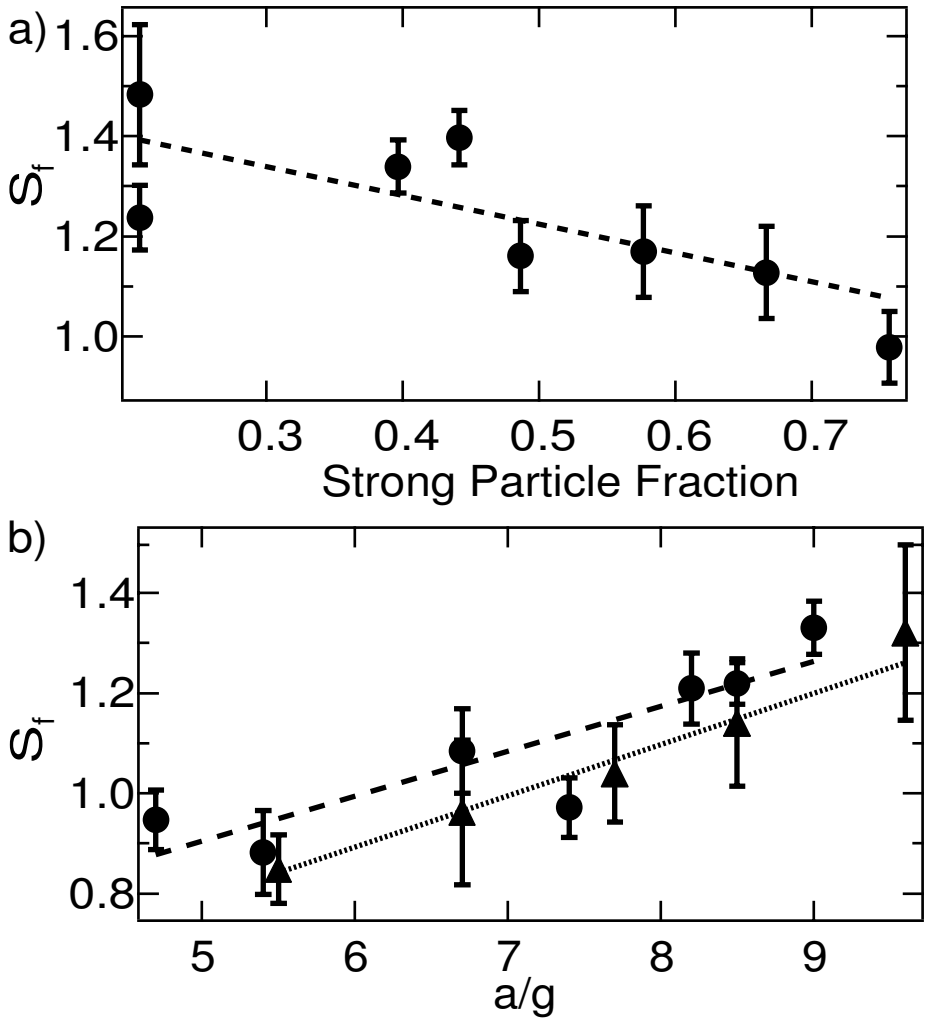

Fig. 5.6: (a) S_f versus the strong particle mixture fraction for strong/weak systems of 111 particles accelerated at $9.0g$. Note that S_f decreases as the number of strong particles in the mixture increases. (b) S_f versus acceleration, a/g, for systems of 111 particles. Mixtures of 44 strong and 67 weak particles are shown as filled circles, while mixtures of 67 strong and 44 long particles are shown as filled triangles. Note that, for both mixtures, S_f increases roughly linearly with acceleration.

dipole moment, $2qh$, is constant. This model is a generalized version of the two-charge model used previously [41, 27]; it reduces to the two-charge model in the limit of $w/D \to 0$. It can also be reduced to a two-point-dipole model in the limit of of $h/D \to 0$, and a single, centrally located point dipole model if $h/D \to 0$ and $w/D \to 0$.

By considering our cylindrical magnets as two uniformly charged discs of opposite sign, but equal total charge magnitude, we can then attempt to match magnetic scalar potentials of our model particles to our real particles. Using our simple two-parameter model, we match the magnetic scalar potential of our real and model particles up to the octopole terms. The weak and strong particles, having similar shaped cores, are both modeled with two parallel point dipoles separated by a distance, $w = 0.31D$, as shown in Fig. 5.7(b). The point dipoles are approximated using $h = 0.01D$ for both the weak and strong particles, with $q = 11.5$ and $q = 34.5$, respectively, to account for the difference in magnetic strength. The long particles are modeled with two opposite point charges of magnitude 2.0, separated by a distance of $0.69D$, as shown in Fig. 5.7(c).

Using our experimental particle type, position, and orientation data extracted from the images, we use our model to approximate the total magnetostatic energy of our systems for every frame. We use the usual Coulomb energy formula, $U_{ij} = \frac{q_i q_j}{R_{ij}}$, and sum over all interparticle pairs of charges (excluding the energy of pairs of charges within the same particle) to obtain the energy of our experimentally observed patterns of particles, U_{ex}. As a reference, we use the magnetic energy of a randomly mixed state of the same spatial and orientational structure, which we

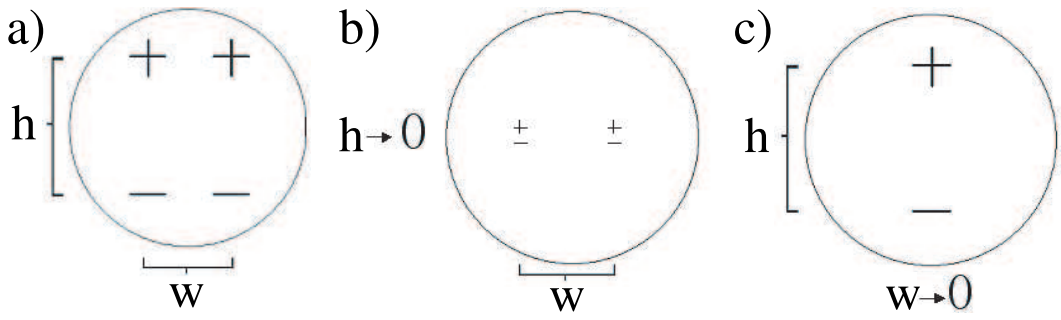

Fig. 5.7: (a) A schematic of our general magnetic particle model, as introduced in Fig. 2.3. (b) For the weak and strong particles, the model reduces to a two point-dipole model, with the dipoles separated by a distance, $w = 0.31D$, where D is the particle diameter. (c) For the long particles, the model in reduces to a two-charge model, with the charges separated by a distance, $h = 0.69D$.

obtain by taking the particle tracking data from the experiment, and interchanging the particle types of randomly chosen particle pairs (keeping the particle locations and dipole orientations fixed). The magnetic energy was then recalculated. This randomization and calculation process was repeated eleven times and the mean magnetic energy of the randomized system, U_r was calculated for each frame. After eleven randomizations, the time average of the standard deviation of the randomized magnetic energy was 5% of U_r.

In Fig. 5.8 (a), we have plotted U_{ex} (filled circles) versus time for the system of 88 weak and 23 strong particles shown in Fig. 5.3. U_r (open circles) is also plotted in Fig. 5.8 (a). The standard deviation of U_r is essentially constant in time at ± 5, approximately. Note that U_{ex} decreases over time, while U_r is roughly constant; also $U_{ex} \leq U_r$ for all time. The noticeable decrease of U_{ex} below U_r over time indicates

that the decrease in U_{ex} is not an artifact of indiscriminant pattern formation, but rather a part of the segregation phenomenon. Fig. 5.8 (b) is a plot of $U_{ex} - U_r$ versus time. Note that $U_{ex} - U_r$ decreases steadily after the first few seconds. The outlying points in Fig. 5.8 (a) and (b) are due to errors in particle position and orientation extraction, where false particles were detected or orientations were improperly extracted. While the observed segregation patterns tend toward states of low magnetostatic energy, it is not expected a priori that a driven dissipative system would arrange into a globally minimal magnetostatic energy state over long times. Rather, the observed patterns can be understood as non-equilibrium steady states.

5.5 Conclusions

Using a simple experiment of a model system, we have shown that in dilute self-assembled networks, a small change in the multipole moment distribution of a small fraction of the particles can significantly increase the branching in the self-assembled network. This has significant implications for the macroscopic properties of polymer networks, and it gives insight into the possible properties of branching particles in biologically relevant systems. Our results also show that otherwise identical systems of magnetized granular particles can segregate due only to differences in their magnetic fields. Vertically vibrated monolayers of magnetic spheres can segregate both by field strength and by field shape. In binary systems of particles with differing field strength, and all other properties identical, the segregation increases with

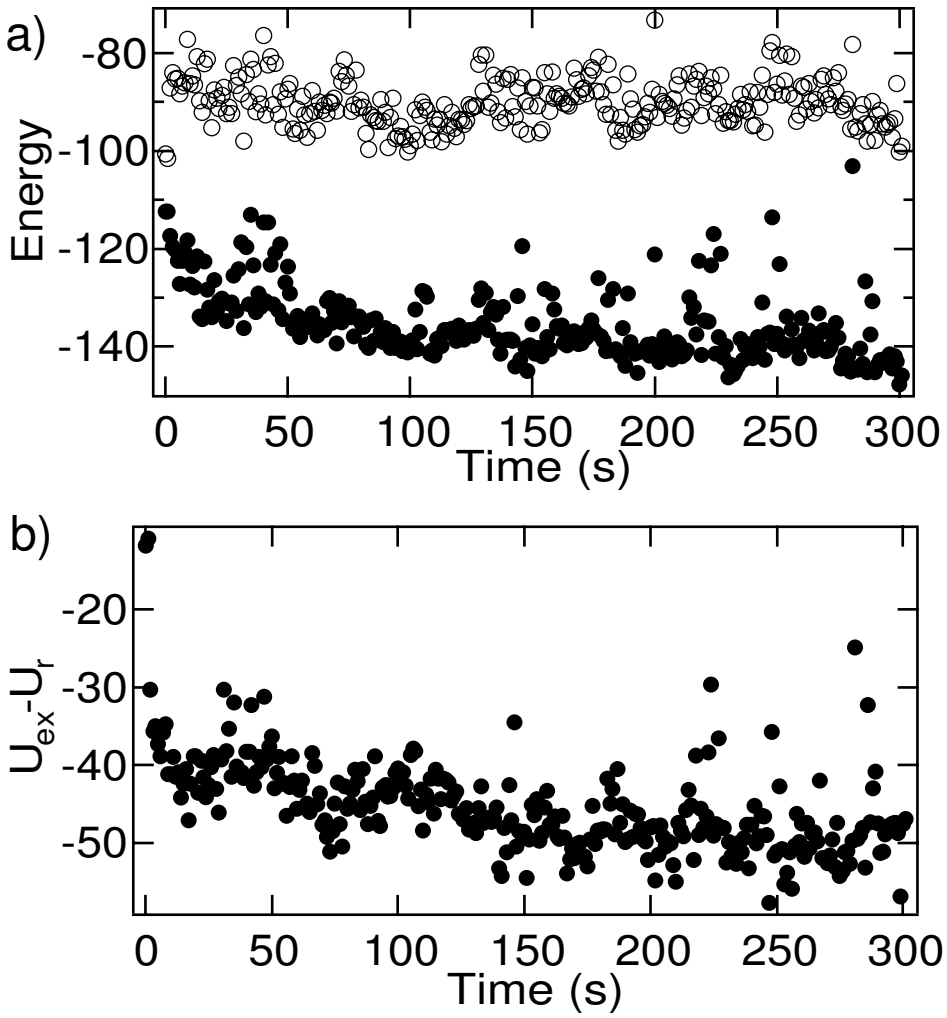

Fig. 5.8: a) The magnetic energy, U_{ex}, versus time for the system of 88 weak and 23 strong particles shown in Fig. 5.3 is plotted as filled circles. The magnetic energy of the randomly mixed state, U_r, is also plotted as open circles for reference. Note that U_{ex} decreases quickly within the first ten seconds, then decreases more gradually over time, while U_r remains roughly constant. b) A plot of $U_{ex} - U_r$ versus time. $U_{ex} - U_r$ decreases steadily after the first few seconds.

the proportion of weaker particles, and it also increases approximately linearly with acceleration over the acceleration range studied. Binary systems of particles with differing field shape and all other properties identical also show approximately linear increases in segregation as acceleration is increased over the acceleration range studied. Segregation occurs in conjunction with a decrease in magnetic energy, with the energy decrease being mostly due to the actual segregation, rather than an evolution of the spatial pattern.

5.6 Outlook

The weak plastic construction of our particles prevents us from probing the behavior of our systems at higher accelerations; however, it seems likely that at high accelerations, the input vibration energy would exceed the magnetic interaction energy, and systems such as ours would remix. While we expect that the qualitative behavior of larger systems to be similar, the small size of the systems we studied makes it difficult to obtain high-quality quantitative statistical results. Possible future work includes studies of larger binary systems of magnetic particles, and using more sturdily constructed particles that allow the investigation of higher accelerations.

It would also be interesting to investigate the interaction properties of particles which induce branching in biological self-assembly and polymer networks, and relate their properties to those of our magnetic branching particles. The interactions between biological macromolecules, and methods of quantitative comparison of interactions will be discussed in Chapter 6. It may be possible to simulate known

branching particles and other biological macromolecules using methods described in Chapter 6, and it would also be intersting to insert new, synthetic particles in the simulation to investigate their roles in the self-assembly of biologically relevent proteins. It is possible that insight gained from such exploration could give insight into possible real synthetic particles that would have similar effects on real biological self-assembly.

6. PROTEINS: ANISOTROPICALLY INTERACTING SELF-ASSEMBLING PARTICLES

6.1 Self-Assembly in Biological Systems

Self-assembly is of particular interest in molecular biology [36, 37]. A wide array of biologically relevant systems form through self-assembly [66]. Protein self-assembly is of particular interest because of the many diseases that are a result of the self-assembly [1, 2, 3, 4, 5, 36, 67]. Hemoglobin S, tubulin, and collagen self-assemble in sickle cell anemia, cancerous tumor growth, and brittle bone disease, respectively. Hemoglobin S, a mutation of the normal hemoglobin A protein, self-assembles into long twisting rope-like structures in the red blood cells of diseased individuals, and inhibits the transportation of oxygen within the body [36].

6.1.1 Hemoglobin

Hemoglobin is a protein mainly found in red blood cells; its chief function is the transport of oxygen within the body. Hemoglobin A is the normal form of the protein, while hemoglobin S is a variant which results from a small mutation of the protein structure. While hemoglobin A typically does not self-organize, hemoglobin S forms long twisting rope-like structures inside red blood cells [36]. Figure 6.1(a)

is a rendering of the hemoglobin A protein taken from the known crystallographic structure [68], while fig. 6.1(b) is a rendering of the hemoglobin S protein [69]. Note that, in fig. 6.1, hemoglobin S appears to be two hemoglobin A proteins bound together; the binding of the two hemoglobin A-like proteins is a consequence of the mutation. Figure 6.2 is a schematic of a typical self-assembly of hemoglobin S proteins. The self-assembly of these proteins is a direct result of the alteration of the interactions from the normal to mutated case.

6.1.2 Tubulin

Tubulin is a roughly cylindrical dimeric protein which self-assembles into long, hollow, cylindrical structures called microtubules inside most living cells [70, 71]. Figure 6.3(a) is a rendering of the tubulin protein, drawn from the known structure of the protein from crystallography [72]; fig. 6.3(b) is a schematic of a normal human microtubule. Microtubules play a crucial role in the transport of materials within the cell, cell structure, and cell division. Because of the key role microtubule growth has in cell division, controlling tubulin self-assembly is the purpose of many modern chemotherapy drugs [2].

6.1.3 Collagen

Collagen is a protein which plays and essential role in the formation of bones and cartilage in the body. There are many variants of the protein, some of which are mutants which cause bone and joint disease [67]. Figure 6.4(a) is a rendering of a collagen protein, drawn from its known structure from crystallography [73]; fig. 6.4(b)

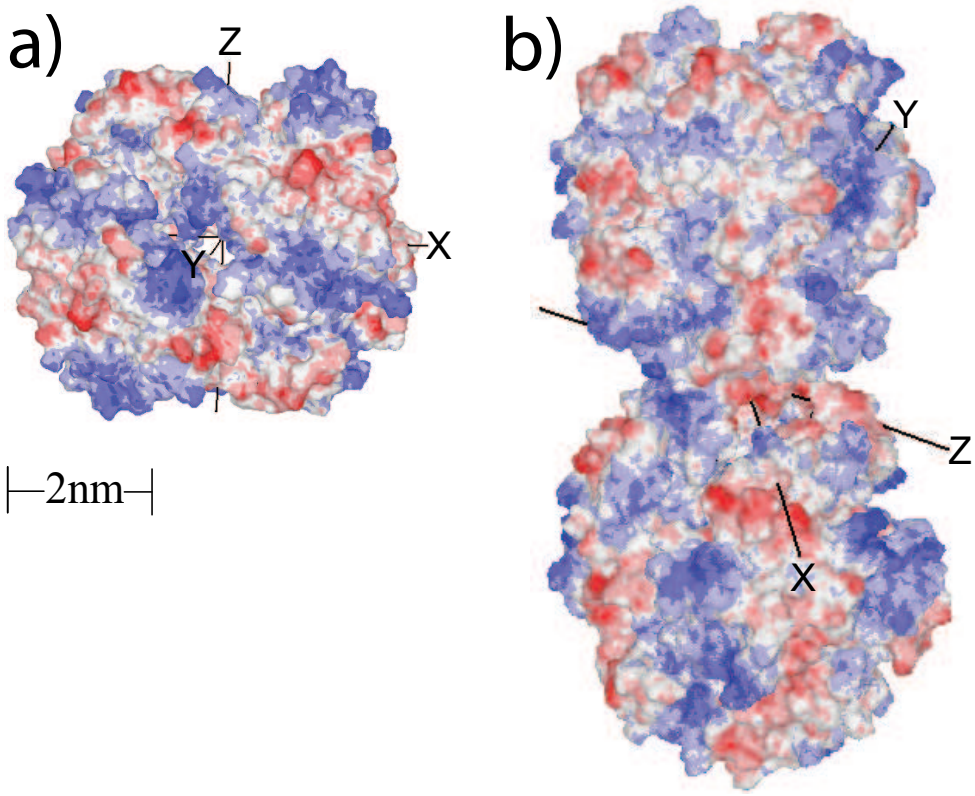

Fig. 6.1: a) A rendering of the electrostatic surface potential of the hemoglobin A protein drawn from the known crystallographic structure using *Protein Explorer Software*. Red indicates an area of relative negative charge, blue is an area of positive charge, and white is neutral. b) A rendering of the hemoglobin S protein by similar method. Note that hemoglobin S appears to be two hemoglobin A proteins bound together.

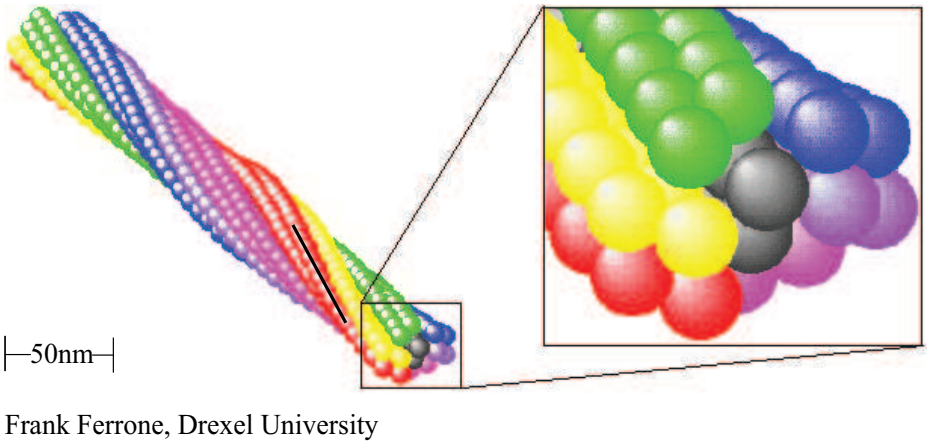

Fig. 6.2: A schematic of the twisted rope-like structure of self-assembled hemoglobin S. Color has no intended significance. *Schematic drawn by Frank Ferrone.*

is a confocal fluorescence microscopy image of the self-assembled network structure formed by normal collagen proteins [74]. It is believed that the mutated collagen associated with disease causes a significant change in collagen interactions, which alters the microscopic and macroscopic physical properties of the self-assembled network [67]. Understanding the roles of the protein interactions on the pattern of self-assembly is of significant interest because of the possible value for therapeutics.

6.2 Protein Electrostatics

Protein interactions, while anisotropic in nature, are generally far too complicated to be described by a point dipole. Interactions between proteins can be divided, principally, into two types [75]:

1. Hydrophobic interactions due to the relative affinities to water of the different surfaces of the protein [76].

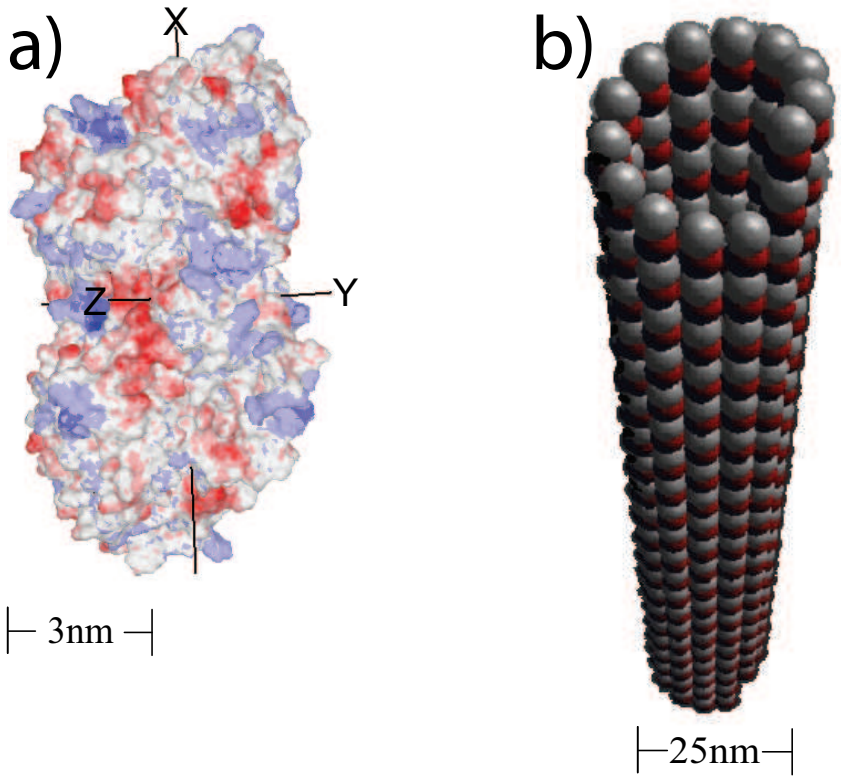

Fig. 6.3: a) A rendering of the electrostatic surface potential of tubulin, drawn from the known crystallographic structure using *Protein Explorer Software*. Red indicates an area of relative negative charge, blue is an area of positive charge, and white is neutral. b) A schematic of a normal human self-assembled structure of tubulin, a microtubule.

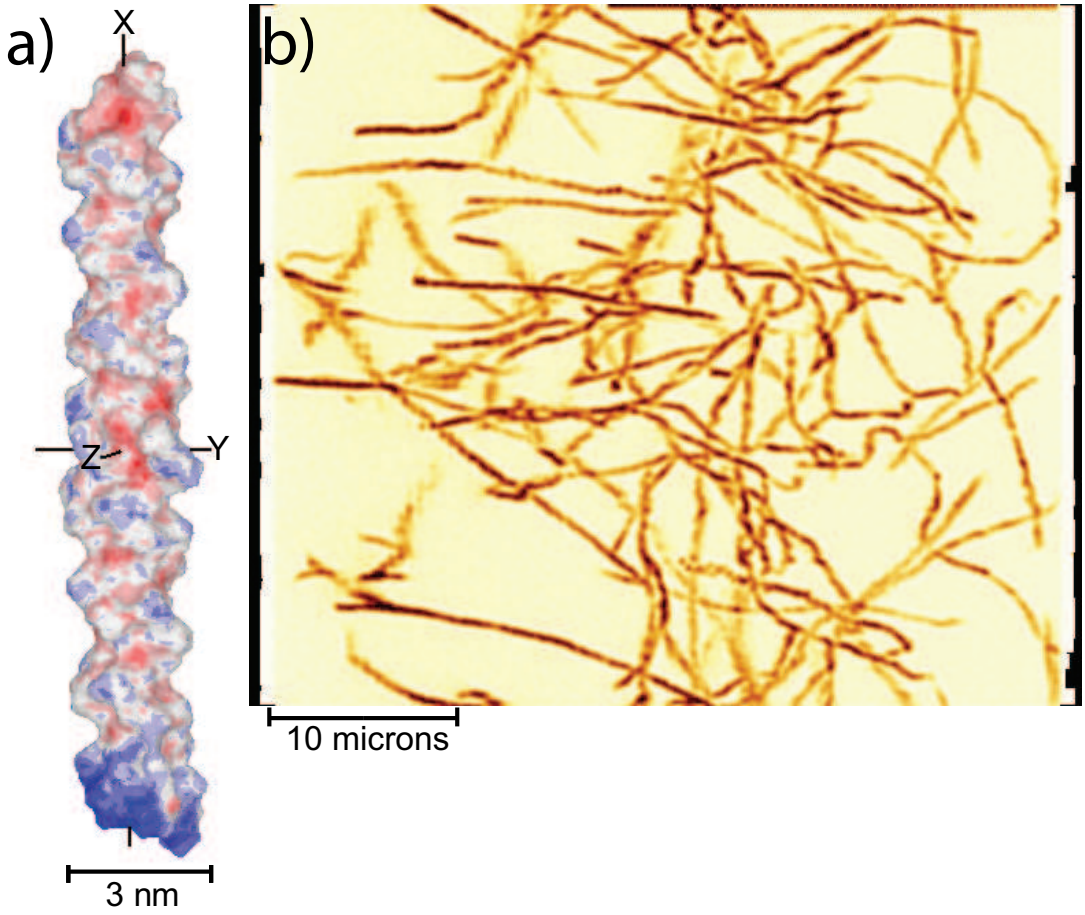

Fig. 6.4: a) A rendering of the electrostatic surface potential of collagen, drawn from the known crystallographic structure using *Protein Explorer Software*. Red indicates an area of relative negative charge, blue is an area of positive charge, and white is neutral. b) A confocal fluorescence microscopy image of the self-assembled network structure formed by normal collagen. *Image taken by Sejin Han and Wolfgang Losert*

2. Electrostatic interactions due to partial electron charges that are induced in the protein by the surrounding solution.

Although both types of interactions are important for most self-assembly, the electrostatic properties of the proteins are more easily quantified, and thus, I will focus upon the protein electrostatics for the remainder of this chapter.

Using X-ray, electron crystallography, and nuclear magnetic resonance, atomically detailed structure information for many proteins has been detrermined and is availible online at the Protein Data Bank (PDB) website, *http://www.rcsb.org/pdb/*. The PDB contains separate files (.pdb files) for each protein, with each file providing the positions of the atoms in a protein. Another online resource, the PDB2PQR Server at *http://agave.wustl.edu/pdb2pqr/*, takes the .pdb files as input and uses molecular modeling (AMBER, CHARMM, or PARSE) to determine approximate partial charges of each atom in the protein, assuming the protein is under normal physiological conditions. The PDB2PQR Server outputs a file (a .pqr file) which contains the position and charge of each atom in the .pdb file. Using the atomic position and charge data, electrostatic moments of many proteins can be calculated. I have calculated the electrostatic moments of hemoglobin A (protein database, *pdb*, code 1A3N), hemoglobin S (pdb code 2HBS), tubulin (pdb code 1JFF), and collagen (pdb code 1CAG); the independent moments of these proteins, up to quadrupole terms, are shown in Table 6.1, and the octopole moments are shown in Table 6.2. Note that the dipolar and higher order moments of all proteins listed in Tables 6.1 and 6.2 are all non-zero, indicating that the proteins interact anisotropically. In

particular, the total dipole moment of tubulin is $293e^{-}nm$, or 1410 Debye; this implies that, neglecting the effects of the surrounding fluid, the dipole-dipole interaction energy between tubulin proteins is on the order of $100kT$ when the proteins are in close proximity. Our calculated charge and dipole moments of tubulin are similar to those calculated by J. A. Brown [77], while our calculated dipole moments of hemoglobin A is significantly lower than the 480D dipole moment calculated by S. Takashima [78]. The discrepancy between our hemoglobin A dipole moment and that calculated by Takashima is likely due to our use of the higher resolution crystallographic structure of the protein and also due to our use of the improved molecular modeling package (AMBER) implicit in the PDB2PQR Server. The use of other available molecular modeling packages (CHARMM and PARSE) in the PDB2PQR Server did not significantly change the calculated moments.

6.3 Multipolar Models

Although the electrostatic potentials of proteins are somewhat simple to estimate using the atomically detailed position and charge data, because of the large number of partial charges associated with the proteins (on the order of 10^4, typically), the computation of electrostatic interactions between proteins can be computationally expensive. The relation between the computation time, t, of forces between electrostatically interacting particles and the number of charges, N, is $t \propto N^2$, if no cutoff length is introduced. Because of the large number of charges associated with most proteins, and the computational time required to properly calculate

Tab. 6.1: Charge, dipole, and quadrupole electrostatic moments of hemoglobin A, hemoglobin S, tubulin, and collagen. P_{total} is in units of Debyes and all other moments are calculated in units of electron charge and nanometers.

Protein	pdb code	Q	P_{total} (Debyes)	P_x	P_y	P_z	Q_{xx}	Q_{yy}	Q_{xy}	Q_{xz}	Q_{yz}
Hemoglobin A	1A3N	11.8	215	1.12	-3.22	-2.91	13.1	-58.7	-2.39	-27.7	5.16
Hemoglobin S	2HBS	28.8	545	8.91	3.92	-5.83	-11.7	209	327	85.4	100
Tubulin	1JFF	-18	1410	7.43	-27.5	7.07	-26.6	48.4	154	105	84.9
Collagen	1CAG	0	1150	-24.0	-.06	-.04	-15.9	8.38	-1.42	1.48	-.072

Tab. 6.2: Octopole electrostatic moments of hemoglobin A, hemoglobin S, tubulin, and collagen. All moments are calculated in units of electron charge and nanometers.

Protein	pdb code	O_{xxx}	O_{xxy}	O_{xxz}	O_{xyy}	O_{xyz}	O_{xzz}	O_{yyy}	O_{yyz}	O_{yzz}	O_{zzz}
Hemoglobin A	1A3N	-10.8	11.7	-14.9	-10.8	-17.4	8.51	-8.05	-5.6	-0.822	-17.5
Hemoglobin S	2HBS	76.6	92.5	-16.0	160	-2.06	-35.9	110	-22.0	-17.8	-42.6
Tubulin	1JFF	83.3	-140	-44.0	27.9	78.0	-103	-146	-0.753	-47.0	47.7
Collagen	1CAG	-386	-4.22	-0.997	-1.98	-0.171	-0.963	0.348	-0.0608	-0.045	-0.0721

electrostatic interactions, large-scale simulations of protein self-assembly based on physical protein-protein interactions, to my knowledge, have not been done. Using electrostatic moments as calculated in the previous section, and a simple Monte Carlo algorithm, I am able to develop simple 8-charge models of the proteins which match the electrostatic moments of the real proteins up to the octopole. This is a significant step toward a computationally inexpensive physical interaction model of self-assembling proteins.

In the Monte Carlo algorithm, 8 charges are allowed to move independently in four-dimensional position-charge space (q, x, y, z), with the range of each position parameter (x, y, z) constrained such that the charges are confined within the model protein's spacial boundaries. q is also constrained such that $|q| \leq q_{max}$, where $q_{max} \approx 100e^{-}$, typically. A rough outline of the Monte Carlo algorithm follows.

Inputs:

- All electrostatic moments of the protein up to octopole.
- Range of (q, x, y, z) parameters.
- A 'thermal' parameter, kT. Typically, $0.0001 \leq kT \leq 1$.

Internal Parameters:

- The variance,

$$V = \sum_{\text{all moments}} \left(\frac{M_{\text{model}} - M_{\text{real}}}{M_{\text{real}}}\right)^2, \tag{6.1}$$

  where M_{model} and M_{real} are electrostatic moments of the model and real protein, respectively. There are three variance parameters in the algorithm,

V_{new}, V_{old}, and V_{min}.

- The Monte Carlo parameter, $\Gamma = e^{\frac{V_{old}-V_{new}}{kTV_{min}}}$.

Steps:

1. V_{old} and V_{min} are initialized to some large number (typically 24).
2. All q, x, y, z are initialized to zero (thus, all model moments are also initialized to zero).
3. One of the 32 position-charge parameters, p, is chosen at random.
4. A new value, p_{new}, of the chosen parameter is selected from a uniform distribution with the range as input.
5. The moments of the model are calculated and V_{new} is calculated.
6. A random number, ϕ, between 0 and 1 is chosen from a uniform distribution.
7. If $\Gamma > \phi$, p_{new} is kept ($p = p_{new}$) and $V_{old} = V_{new}$. Also, if $V_{new} < V_{min}$, $V_{min} = V_{new}$.
8. The program loops back to step 4.

The program is allowed to continue to loop until V_{min} is sufficiently small. Typically, runtime is about 24 hours for 4×10^9 loops, where $V_{min} \approx 10^{-6}$ at completion, such that all moments are matched to better than 1%. Because this algorithm takes only electrostatic moments, the ranges of parameters, and a thermal parameter as input, it can be used to develop minimal electrostatic models of nearly any protein.

The algorithm can be easily be modified to give the desired model accuracy. The number of moments to match determines the number of charges needed in the model (1 charge for monopole, 2 for dipole, 4 for quadrupole, etc.).

6.4 Outlook

The relatively low runtime for the above descried algorithm makes it especially useful for large-scale self-assembly simulations where electrostatic calculations are computationally expensive. However, the hydrophobic interactions must also be accounted for if a structure-based model of protein interactions is to be used. If simple models of the hydrophobic interactions can be developed, it may be possible to accurately and simply model total protein interactions with a superposition of minimal electrostatic and hydrophobic models. One possible method of simulating hydrophobic interactions is to use 'charges' that have Lennard-Jones interactions. The magnitudes and positions of such 'charges' could be varied and possibly matched with information extracted from the Protein Data Bank, similar to the method used in the algorithm described above. However, for the remainder of this thesis I investigate fundamental anisotropic interaction models with no particular reference to hydrophobic or electrostatic protein modeling.

7. THE EFFECTS OF MULTIPOLAR INTERACTIONS ON SELF-ASSEMBLY

7.1 Overview

As illustrated in previous chapters, anisotropically interacting particles form a wide variety of self-assembly patterns. Controlling the self-assembly and the types of patterns that are formed is currently a major goal for several fields of study ranging from polymer engineering to cellular biology and medicine. In particular, controlling protein self-assembly is of significant interest to the pharmaceutical industry because of possible therapeutic value. For example, the chemotherapy drug Taxol introduces additional interactions among tubulin proteins in cancer cells and which, in turn, prevents cell division and the growth of tumors [2]. However, because of the computational expense of simulating such complex self-assembly systems at the molecular level and a desire to understand the self-assembly at a fundamental level, there has been recent renewed interest in the self-assembly of particles with simple interaction potentials such as dipolar spheres [29, 41].

In our recent work [41, 42], we investigated the effects of higher order multipole moments on self-assembly using numerical modeling and simple experiments on a macroscopic toy model of magnetic particles. We showed that a small change

in the multipole moment distribution of the particles can significantly alter the preferred self-assembly pattern in binary and monodisperse systems. In this chapter, we show that if the interactions of all particles are uniformly altered, complex self-assembled structures can be stabilised. As an example, we propose a simple point charge model of the protein tubulin, and we show that, without altering the dipole moment, the addition of higher order multipole moments to the model can energetically stabilise the biologically correct self-assembly pattern. We also present a physical macroscopic magnetic analog of our model, and show that it has many of the same structural characteristics as microtubules.

7.2 Biological Background

As illustrated in Chapter 6, microtubules are long, hollow, cylindrical structures formed by the self-assembly of roughly cylindrical dimeric tubulin proteins inside cells [70, 71]. In the presence of different drugs and ions, tubulin proteins (each about 8.0 nm long and 4.6 nm in diameter) self assemble into a plethora of other structures including rings, sheets [79], spirals, and 'macrotubules' [37]. While many variations of microtubule structure have been seen [80], for *in vivo* human microtubules, tubulin arranges into thirteen long filaments (*protofilaments*) that form the wall of the cylindrical tube structure. In the microtubule lattice, protofilaments are staggered by 0.93 nm from neighboring protofilaments [81] and, at the edges of depolymerizing microtubules, the protofilaments are believed to fray out from the main tube structure and break off [82].

The unusual pattern of microtubule growth and sudden shrinkage (termed *dynamic instability*) is not entirely understood, and is a topic of active research [75, 83]. It is our belief that simulations of tubulin self-assembly based on physical interactions between proteins could elucidate the microtubule growth process, and perhaps aid in novel drug discovery. However, because of the significant computational expense of using atomically detailed tubulin interaction models, large scale simulations of tubulin self-assembly based on physical interactions, to our knowledge, have not been done. The goal of our work is to develop an interaction model which accurately reproduces the self-assembly and is also simple enough to use in large-scale simulations.

Many investigations have been done in an attempt to understand the interaction between individual tubulin dimers and its relationship to microtubule structure [75, 84, 85]. In particular, recent computational work by Sept *et al.* [75] correctly predicted the microtubule filament staggering, and gave estimates of interfilament and intrafilament tubulin-tubulin binding energies using the known structure of microtubules [86]. However, because of the complexity of the tubulin protein and the computational expense of accurately reproducing all interactions, the study was limited to static energy calculations of only five proteins in a limited number of spacial configurations.

It is well known that tubulin is a protein that carries a strong electrostatic dipole moment [77]. Recent calculations, based on the known structure of tubulin indicates the strength of the intrinsic dipole moment of tubulin is about 1700D [77]; neglecting the effects of the surrounding solution, this indicates the tubulin dipole-

dipole interaction energy is on the order of 100 kT. It has also been shown that *in vitro* microtubules align in the presence of an electric field [87, 88]. The electrostatic polarity of microtubules, and its possible relationship to its cellular functionality is a topic of current research [89]. In addition to the known effects of electric fields on microtubules, it has also been shown that magnetic [87] and even gravitational fields [90] can significantly effect microtubule growth. While models based on the dipolar nature of tubulin have been used in investigations of microtubule function [38, 77, 91, 92], models which investigate the role of higher order moments in tubulin self-assembly have not been studied, to our knowledge.

7.3 Experimental Toy Model

Figure 7.1 is a photograph of patterns formed by cylindrical permanent magnets (dipolar cylinders) of length 1.42 cm and diameter 0.95 cm, similar to those used in the 'long' magnetic particles in Chapters 3-5. The magnets form a staggered, frayed yet stable microtubule-like 2D structure when chains of the magnets are brought together with consistent orientation. When chains of magnets are brought together with opposite orientation, they form a stable, non-frayed sheet, much like the zinc-stabilized tubulin sheets seen in previous work [37]. Chains of magnets can also be bent to form a closed ring shape, much like the observed tubulin rings [37, 93]. Inspired by these observations of self-assembled dipolar cylinders, we propose a simple interaction model that reproduces many of the key features of microtubules, including 0.93 nm staggering between neighboring protofilaments, stable microtubule

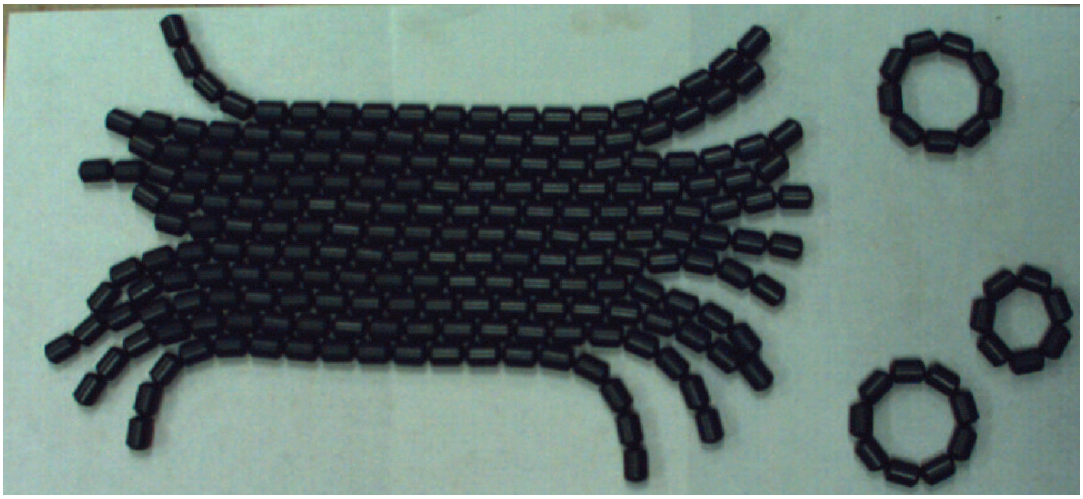

Fig. 7.1: A photograph of patterns formed by cylindrical permanent magnets of length 1.42 cm and diameter 0.95 cm. The magnets form a staggered, frayed yet stable microtubule-like structure when chains of the magnets are brought together with consistent orientation. Chains of magnets can also be bent to form a closed ring shape, much like the observed tubulin rings.

structure, and fraying protofilaments at the edges of the microtubule.

7.4 Theoretical Tubulin Model Details

Figure 7.2a is a schematic of our tubulin model. The model consists of an impenetrable rectangle of dimensions, 4.6 by 8.0 (unitless), encasing four point charges of magnitude 1. The point charges are arranged such that the model protein has zero charge, and the dipole moment is directed along the long axis of the protein (parallel with the microtubule axis). The charges are separated by vertical and lateral distances, s and t, so that if $s \neq 0$ or $t \neq 0$, moments of order higher than the dipole are generated. This model is a generalized version of the point dipole model

of tubulin used by Tuszyński *et al.* [92], and it reduces to a point dipole model when $s \to 0$ and $t \to 0$.

7.5 Energetic Considerations

The model proteins are arranged in a 3D, cylindrical, microtubule-like lattice as shown in Figure 5.7b. We use a Coulombic energy equation,

$$U_{ij} = \begin{cases} \frac{q_i q_j}{R_{ij}}, & \text{interprotein} \\ 0, & \text{intraprotein} \end{cases}$$

and sum over all pairs of charges (excluding the energy of pairs of charges within the same protein) to obtain the energy of our model microtubule,

$$U_{tot} = \sum_{i=1}^{4ZC} \sum_{j=i+1}^{4ZC} U_{ij}, \tag{7.1}$$

where i is a parameter that runs through the charges along the length of the microtubule, Z is the number of proteins in each protofilament, j is a parameter that runs through the charges around the circumference of the microtubule, and C is the number of protofilaments. In our investigation, the parameters varied were the protofilament staggering, δ, the vertical and lateral charge separations, s and t, the number of fraying proteins in each frayed protofilament at the edge of the microtubule, N, and the curvature of the frayed protofilaments, A. C was kept fixed at 13, while Z was varied from 10 to 100. We normalize U_{tot} to the energy of 13 infinitely separated protofilaments of length Z, such that

$$E = \frac{U_{tot} - 13 * U_{fil}}{13 * U_{fil}}, \tag{7.2}$$

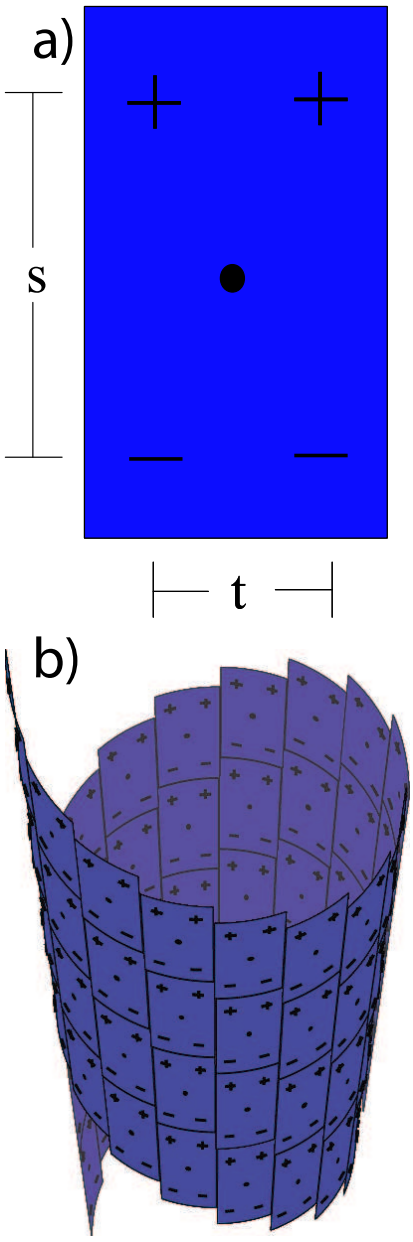

Fig. 7.2: a) A schematic of our tubulin model. Four point charges are separated by vertical and lateral distances, s and t, and encased in an impenetrable rectangle of dimensions, 4.6 by 8.0 (unitless). b) The model proteins are arranged in a 3D, cylindrical, microtubule-like lattice.

where E is the normalized energy, and U_{fil} is the energy of an isolated protofilament of length Z. We also calculate an energy density, which is the energy of each model protein within a structure,

$$\mathcal{U}(z,c) = \sum_{k=\text{internal charges}} \sum_{l=\text{external charges}} \frac{q_k q_l}{R_{kl}}, \tag{7.3}$$

where the k is a parameter that runs through all the charges within a single protein, l is a parameter that runs through all charges outside of that protein, z is an integral position index of the protein in a protofilament ($1 \leq z \leq Z$), and c is an integral position index of the protofilament within the microtubule ($1 \leq c \leq C$). A normalized energy density,

$$\mathcal{E}(z,c) = \frac{\mathcal{U}_{tot}(z,c) - \mathcal{U}_{fil}(z)}{\mathcal{U}_{fil}(z)}, \tag{7.4}$$

is then calculated, where $\mathcal{U}_{tot}(z,c)$ is the energy density of a protein at position (z,c) within the microtubule of length Z, and $\mathcal{U}_{fil}(z)$ is the energy density of a protein at position z within an isolated protofilament of the same length, Z.

Figure 7.3a is a plot of E vs. δ for a point dipole model of tubulin ($s \rightarrow \neq 0$ and $t \rightarrow \neq 0$), in a model microtubule where $Z = 30$. Note that the energy minimum is at $\delta = 4.3$ nm, unlike physical microtubules. This indicates that the point dipole model does not reproduce a realistic staggering. Figure 7.4a is a plot of $\mathcal{E}$ within the model microtubule. Note $\mathcal{E} > 0$ everywhere within the microtubule. This is evidence this simple point dipole model is cannot produce a stable microtubule structure.

Figure 7.3b is a plot of E vs. δ for a four point charge model of tubulin with $s = 7.2$, $t = 4.4$, and $Z = 30$. Note that the energy minimum is at $\delta = 0.93$ nm, as is the case in 13-protofilament microtubules. Figure 7.4b is a plot of $\mathcal{E}$

within the same model microtubule. $\mathcal{E} < 0$ within the core of the microtubule, indicating the formation of a stable microtubule core. The sharp rise in $\mathcal{E}$ at the ends of the microtubule is evidence that the microtubule edges are unstable and have an energetic preference to separate into isolated protofilaments. The four charge model of tubulin with $s = 7.2$ and $t = 4.4$ reproduces both the 0.93 nm staggering of real microtubules, and the stable tube structure. The instability of the model microtubule ends also suggests that the model may reproduce the fraying protofilaments seen in earlier experimental studies [82].

7.6 Conclusions

In this chapter, we showed that if the interactions of all particles are uniformly altered, complex self-assembled structures can be stabilised. As an example, we proposed a simple point charge model of the protein tubulin, and showed that, without altering the dipole moment, the addition of higher order multipole moments to the model can energetically stabilise the biologically relevant self-assembly pattern. We also presented a physical macroscopic magnetic analog of our model, and show that it has many of the same structural characteristics as microtubules.

7.7 Outlook

Given that a simple four point charge model can stabilise such complex structures as microtubules, it is likely that similar models could be used to gain insight into the self-assembly of other anisotropically interacting particles and macromolecules.

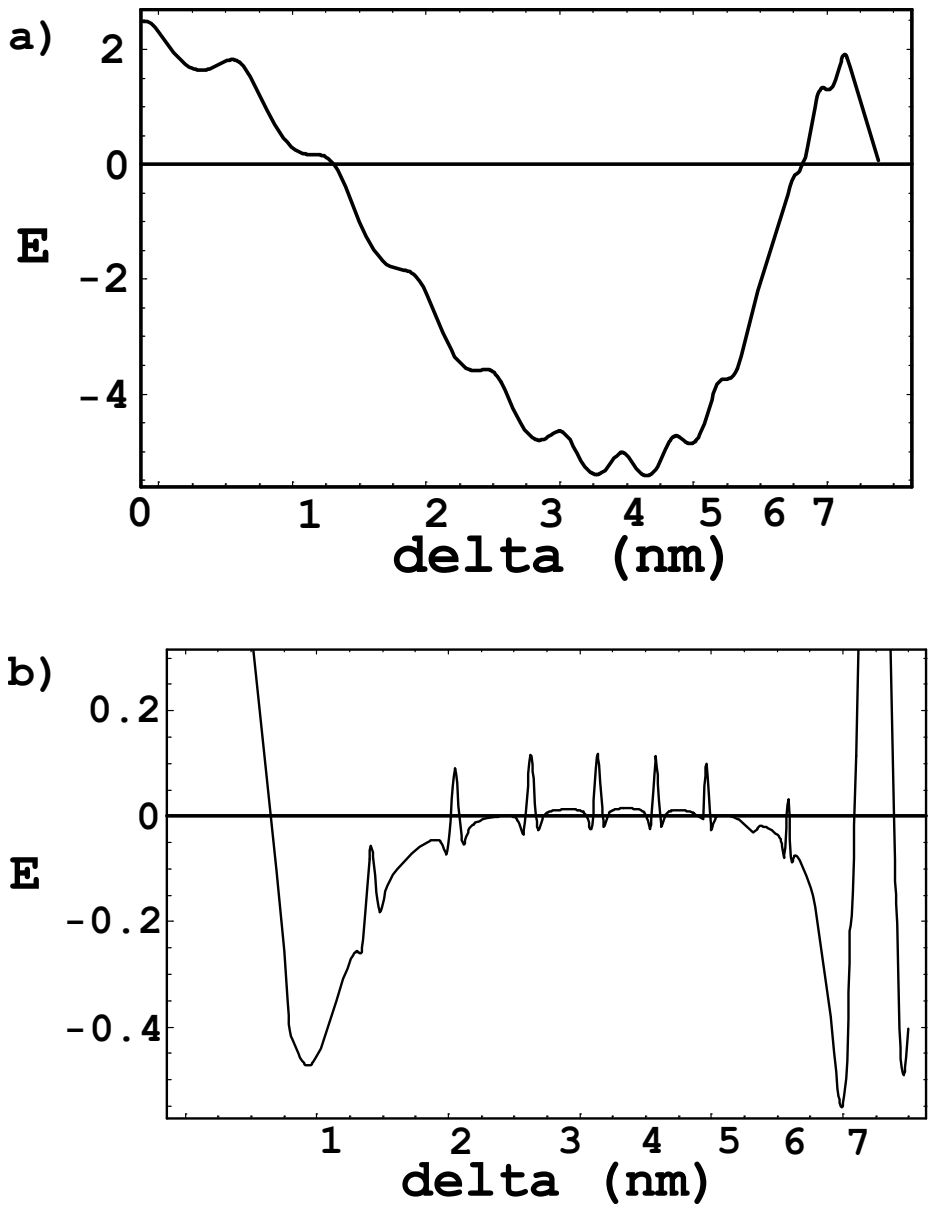

Fig. 7.3: a) A plot of E vs. δ for a point dipole model of tubulin in a 3D microtubule lattice with $Z = 30$. Note that the energy minimum is at $\delta = 4.3$nm, unlike physical microtubules. b) A plot of E vs. δ for a four point charge model of tubulin with $s = 7.2$, $t = 4.4$, and $Z = 30$. Note that the energy minimum is at $\delta = 0.93$nm, as is the case in real 13-protofilament microtubules.

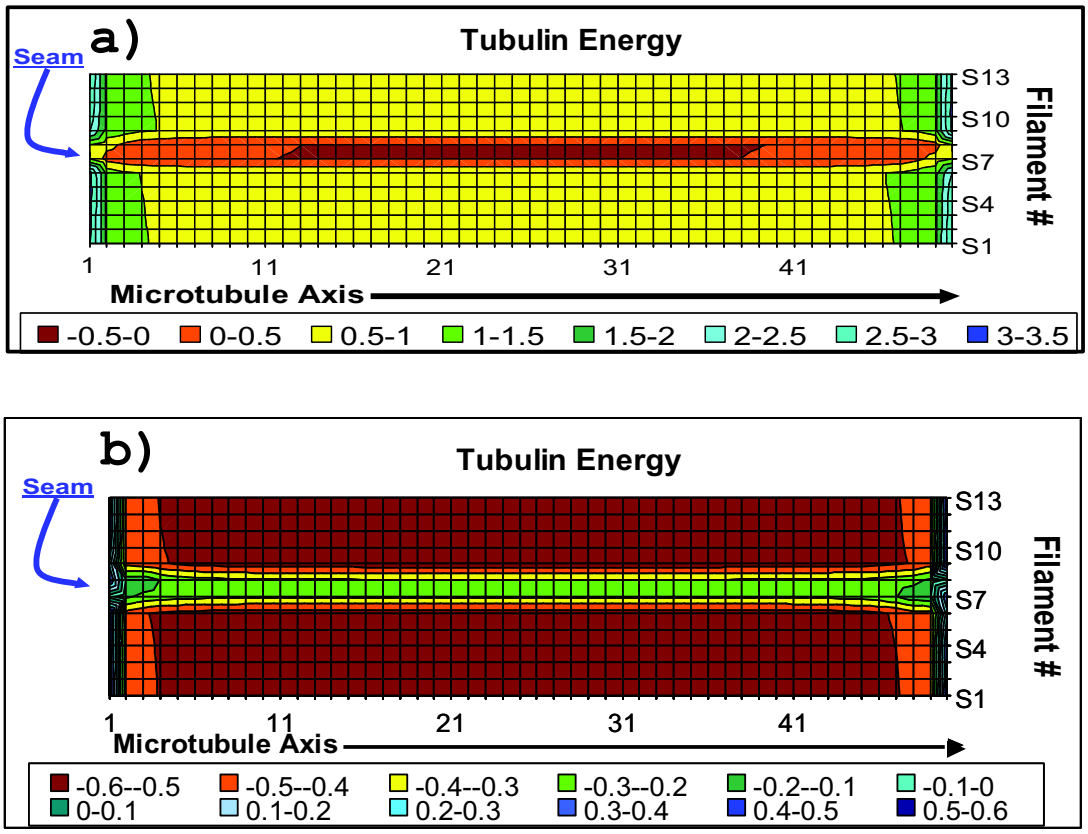

Fig. 7.4: a) A plot of $\mathcal{E}$ within the model microtubule. Note $\mathcal{E} > 0$ everywhere within the microtubule, indicating instability. b) A plot of $\mathcal{E}$ within the same model microtubule. $\mathcal{E} < 0$ within the core of the microtubule, indicating the formation of a stable microtubule core. The sharp rise in $\mathcal{E}$ at the ends of the microtubule is evidence that the microtubule edges are unstable and have an energetic preference to separate into isolated protofilaments.

Developing such models could be difficult, however, without deriving the models directly from the crystallographic data in the Protein Data Bank, similar to the method described in Chapter 6. In order to generalize this modeling to function for any arbitrary protein, methods must be developed to effectively and simply model the hydrophobic interactions betwee proteins. Together with the method of modeling electrostatics described in Chapter 6, a method of developing a minimal hydrophobic model of protein interactions could lead to an efficient method of modeling and simulating a wide array of proteins, and could give important insight into the self-assembly and possibly aid in drug discovery.

APPENDIX

A. SEGREGATION IN A MONOLAYER OF MAGNETIC SPHERES

A.1 Energetic Considerations

We assume our magnets are uniformly magnetized cylinders of axial length, l, constant diameter, d, with the cylinder axis coincident with the z axis and the center of mass at the origin. We may then model the magnetostatics of the magnet using two uniformly charged discs of opposite sign, but equal total charge magnitude q_{tot}, of diameter d with the centers of each disc set a distance l apart, and with the coincident planes of each of the discs being parallel. The magnetostatic moment calculations of the magnets follow.

Charge:

$$Q = \int_{\text{all space}} \rho(\mathbf{x}) d^3\mathbf{x} = q_{tot} - q_{tot} = 0 \tag{A.1}$$

Dipole:

$$P_x = \int_{\text{all space}} \rho(\mathbf{x}) x d^3\mathbf{x} = 0 \tag{A.2}$$

and

$$P_y = \int_{\text{all space}} \rho(\mathbf{x}) y d^3\mathbf{x} = 0, \tag{A.3}$$

by symmetry.

$$P_z = \int_{\text{all space}} \rho(\mathbf{x}) z d^3\mathbf{x} = q_{tot} l - q_{tot}(-l) = 2q_{tot} l \tag{A.4}$$

Quadrupole:

$$Q_{xx} = \int_{\text{all space}} \rho(\mathbf{x})(2x^2 - y^2 - z^2) d^3\mathbf{x} = 0, \tag{A.5}$$

because the position term is even in z and the charge term is odd in z. Similarly, $Q_{yy} = Q_{zz} = 0$.

$$Q_{xy} = Q_{yx} = \int_{\text{all space}} \rho(\mathbf{x})(3xy) d^3\mathbf{x} = 0, \tag{A.6}$$

because the position term is even in z and the charge term is odd in z.

$$Q_{xz} = Q_{zx} = \int_{\text{all space}} \rho(\mathbf{x})(3xz) d^3\mathbf{x} = 0, \tag{A.7}$$

because the position term is odd in x and the charge term is even in x. Similarly, $Q_{yz} = Q_{zy} = 0$, by symmetry.

Thus, all quadrupole moments are identically zero because of symmetry.

Octopole:

We also calculate the octopole terms in the multipole moment expansion (equation 2.1). In particular, we calculate the $l = 3$ terms in

$$q_{lm} = \int_{\text{all space}} Y^*_{lm}(\theta,\phi)\rho(\mathbf{x})r^l d^3\mathbf{x}, \tag{A.8}$$

where the $Y^*_{lm}(\theta,\phi)$ are the complex conjugates of the spherical harmonics.

$$q_{30} = \sqrt{\frac{7}{16\pi}}\int_{\text{all space}}(2z^3 - 3zr^2)\rho(\mathbf{x})d^3\mathbf{x} \tag{A.9}$$

$$= \frac{2lq_{tot}}{\pi d^2}\sqrt{\frac{7}{16\pi}}\int_{\text{r}=0}^{d/2} 2\pi(l^2 r - 6r^3)dr \tag{A.10}$$

$$= \frac{4lq_{tot}}{d^2}\sqrt{\frac{7}{16\pi}}(\frac{l^2d^2}{8} - \frac{6d^4}{64}) \tag{A.11}$$

$$= \frac{lq_{tot}}{2}\sqrt{\frac{7}{16\pi}}(l^2 - \frac{3d^2}{4}) \tag{A.12}$$

$$\tag{A.13}$$

$$q_{31} = -\frac{1}{4}\sqrt{\frac{21}{4\pi}}\int_{\text{all space}}(x - iy)(5z^2 - r^2)\rho(\mathbf{x})d^3\mathbf{x} = 0, \tag{A.14}$$

because the position term is even in z and the charge term is odd in z.

$$q_{32} = \frac{1}{4}\sqrt{\frac{105}{2\pi}}\int_{\text{all space}}(zx^2 - zy^2 - 2ixyz)\rho(\mathbf{x})d^3\mathbf{x} \tag{A.15}$$

$$= \frac{1}{4}\sqrt{\frac{105}{2\pi}}\int_{\text{all space}}(-2ixyz)\rho(\mathbf{x})d^3\mathbf{x} = 0, \tag{A.16}$$

because the position term is odd in x and the charge term is even in x.

$$q_{33} = -\frac{1}{4}\sqrt{\frac{35}{4\pi}}\int_{\text{all space}}(x^3 + iy^3 - 3xy^2 - 3ix^2y)\rho(\mathbf{x})d^3\mathbf{x} = 0, \tag{A.17}$$

because the position term is even in z and the charge term is odd in z.

The magnetostatic moment calculations of our model, as described in 2.3 follow. For the purposes of these calculations, the coincident plane of the four charges is the yz plane, with the center of mass at the origin, the dipole moment parallel with the z axis, and the magnitude of the charges, $q \equiv \frac{q_{tot}l}{2h}$ to keep the total dipole moment constant and equal to that of the magnet.

Charge:

$$Q = \int_{\text{all space}} \rho(\mathbf{x}) d^3\mathbf{x} = q + q - q - q = 0 \tag{A.18}$$

Dipole:

$$P_x = \int_{\text{all space}} \rho(\mathbf{x}) x d^3\mathbf{x} = 0 \tag{A.19}$$

and

$$P_y = \int_{\text{all space}} \rho(\mathbf{x}) y d^3\mathbf{x} = 0, \tag{A.20}$$

by symmetry.

$$P_z = \int_{\text{all space}} \rho(\mathbf{x}) z d^3\mathbf{x} = qh - q(-h) = 2qh = 2q_{tot}l \tag{A.21}$$

Quadrupole:

$$Q_{xx} = \int_{\text{all space}} \rho(\mathbf{x})(2x^2 - y^2 - z^2) d^3\mathbf{x} = 0, \tag{A.22}$$

because the position term is even in z and the charge term is odd in z. Similarly, $Q_{yy} = Q_{zz} = 0$.

$$Q_{xy} = Q_{yx} = \int_{\text{all space}} \rho(\mathbf{x})(3xy)d^3\mathbf{x} = 0, \tag{A.23}$$

because the position term is even in z and the charge term is odd in z.

$$Q_{xz} = Q_{zx} = \int_{\text{all space}} \rho(\mathbf{x})(3xz)d^3\mathbf{x} = 0, \tag{A.24}$$

because the position term is odd in x and the charge term is even in x. Similarly, $Q_{yz} = Q_{zy} = 0$, by symmetry.

Thus, all quadrupole moments are identically zero because of symmetry.

Octopole:

We also calculate the octopole terms in the multipole moment expansion (equation 2.1). In particular, we calculate the $l = 3$ terms in

$$q_{lm} = \int_{\text{all space}} Y^*_{lm}(\theta, \phi)\rho(\mathbf{x})r^l d^3\mathbf{x}, \tag{A.25}$$

where the $Y^*_{lm}(\theta, \phi)$ are the complex conjugates of the spherical harmonics.

$$q_{30} = \sqrt{\frac{7}{16\pi}} \int_{\text{all space}} (2z^3 - 3zx^2 - 3zy^2)\rho(\mathbf{x})d^3\mathbf{x} \tag{A.26}$$

$$= \sqrt{\frac{7}{16\pi}} \sum_{\text{all charges}} q_i(2z^3 - 3zx^2 - 3zy^2) \tag{A.27}$$

$$= \frac{q_{tot}h}{4}\sqrt{\frac{7}{16\pi}}(2h^2 - 3w^2) \tag{A.28}$$

$$\tag{A.29}$$

$$q_{31} = -\frac{1}{4}\sqrt{\frac{21}{4\pi}} \int_{\text{all space}} (x - iy)(5z^2 - r^2)\rho(\mathbf{x})d^3\mathbf{x} = 0, \tag{A.30}$$

because the position term is even in z and the charge term is odd in z.

$$q_{32} = \frac{1}{4}\sqrt{\frac{105}{2\pi}} \sum_{\text{all charges}} q_i(zx^2 - zy^2 - 2ixyz) \tag{A.31}$$

$$= \frac{1}{4}\sqrt{\frac{105}{2\pi}} \sum_{\text{all charges}} q_i(-zy^2) \tag{A.32}$$

$$= -\frac{qhw^2}{8}\sqrt{\frac{105}{2\pi}}, \tag{A.33}$$

$$q_{33} = -\frac{1}{4}\sqrt{\frac{35}{4\pi}} \int_{\text{all space}} (x^3 + iy^3 - 3xy^2 - 3ix^2y)\rho(\mathbf{x})d^3\mathbf{x} = 0, \tag{A.34}$$

because the position term is even in z and the charge term is odd in z.

In matching the model to the experiment, all moments below octopole are equivalent by design. For the octopole terms,

$$q_{32} = 0 \text{ for the experiment,} \tag{A.35}$$

$$\text{while } q_{32} = -\frac{qhw^2}{8}\sqrt{\frac{105}{2\pi}} \text{ for the model.} \tag{A.36}$$

Thus, $h = 0$ or $w = 0$ for the model.

Also,

$$q_{30} = \frac{lq_{tot}}{2}\sqrt{\frac{7}{16\pi}}(h^2 - \frac{3d^2}{4}) \text{ for the experiment,} \tag{A.37}$$

$$\text{while } q_{30} = \frac{q_{tot}h}{4}\sqrt{\frac{7}{16\pi}}(2h^2 - 3w^2) \text{ for the model.} \tag{A.38}$$

Thus,

$$q_{30} = \begin{cases} \frac{q_{tot}h}{4}\sqrt{\frac{7}{16\pi}}(-3w^2), & h = 0 \\ \frac{q_{tot}h}{4}\sqrt{\frac{7}{16\pi}}(2h^2), & w = 0 \end{cases} = \frac{lq_{tot}}{2}\sqrt{\frac{7}{16\pi}}(l^2 - \frac{3d^2}{4}).$$

So, if

$$\begin{cases} l > \frac{\sqrt{3}d}{2}, & w = 0 \\ l < \frac{\sqrt{3}d}{2}, & h = 0 \\ l = \frac{\sqrt{3}d}{2}, & h = w = 0 \end{cases}$$

and for

$$\begin{cases} h = 0, & w = \sqrt{\frac{d^2}{2} - \frac{2l^2}{3}} \\ w = 0, & h = \sqrt{l^2 - \frac{3d^2}{4}} \end{cases}$$

B. PATTERN FORMATION IN A MONOLAYER OF MAGNETIC SPHERES

B.1 Energetic Considerations

Figure B.1 is a plot of the energies (normalized to the energy of $\sqrt{N}$ infinitely separated chains of length $\sqrt{N}$) of several different patterns of short ($h = 0.001$, $w = 0.25$) model particles versus $\sqrt{N}$. All patterns except the ring pattern are rectangular lattices of dimensions N particles by N particles. Note that the microvortex and macrovortex energies are nearly identical and are the energetically preferred patterns for $\sqrt{N} > 3$. Also note that the HCP ferromagnetic pattern decreases significantly relative to all other patterns, over the calculated range.

Figure B.2 is a plot of the energies (normalized to the energy of $\sqrt{N}$ infinitely separated chains of length $\sqrt{N}$) of several different patterns of weak ($h = 0.001$,$w = 0.31$) model particles versus $\sqrt{N}$. All patterns except the ring pattern are rectangular lattices of dimensions N particles by N particles. Note that the microvortex is the energetically preferred pattern for $\sqrt{N} > 3$. Also note that the HCP ferromagnetic pattern decreases significantly relative to all other patterns, over the calculated range.

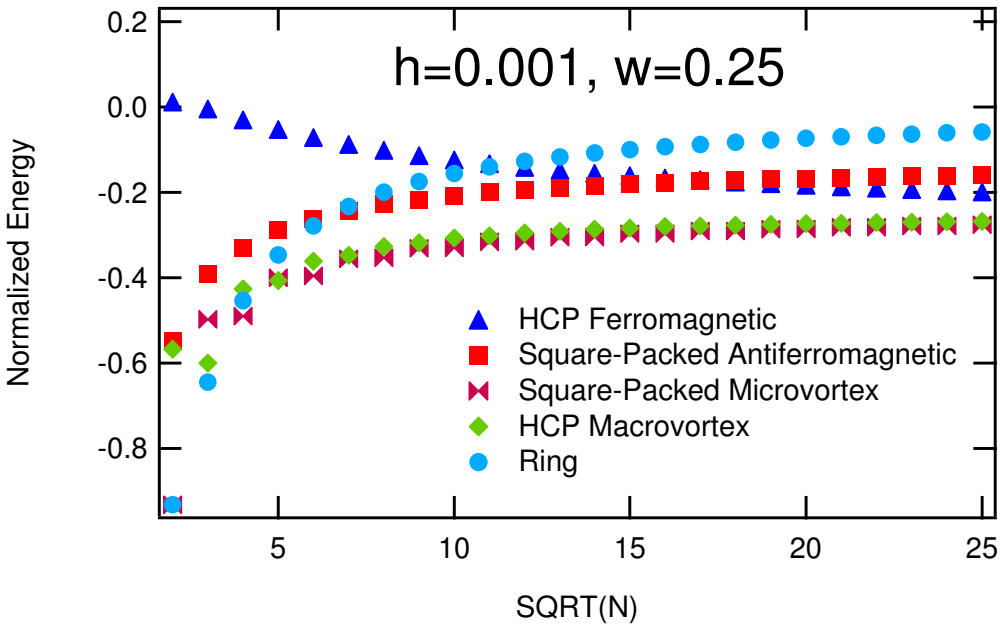

Fig. B.1: A plot of the energies (normalized to the energy of $\sqrt{N}$ infinitely separated chains of length $\sqrt{N}$) of several different patterns of $h = 0.001$, $w = 0.25$ particles versus $\sqrt{N}$. All patterns except the ring pattern are rectangular lattices of dimensions N particles by N particles. Note that the microvortex and macrovortex energies are nearly identical and are the energetically preferred patterns for $\sqrt{N} > 3$. Also note that the HCP ferromagnetic pattern decreases significantly relative to all other patterns, over the calculated range.

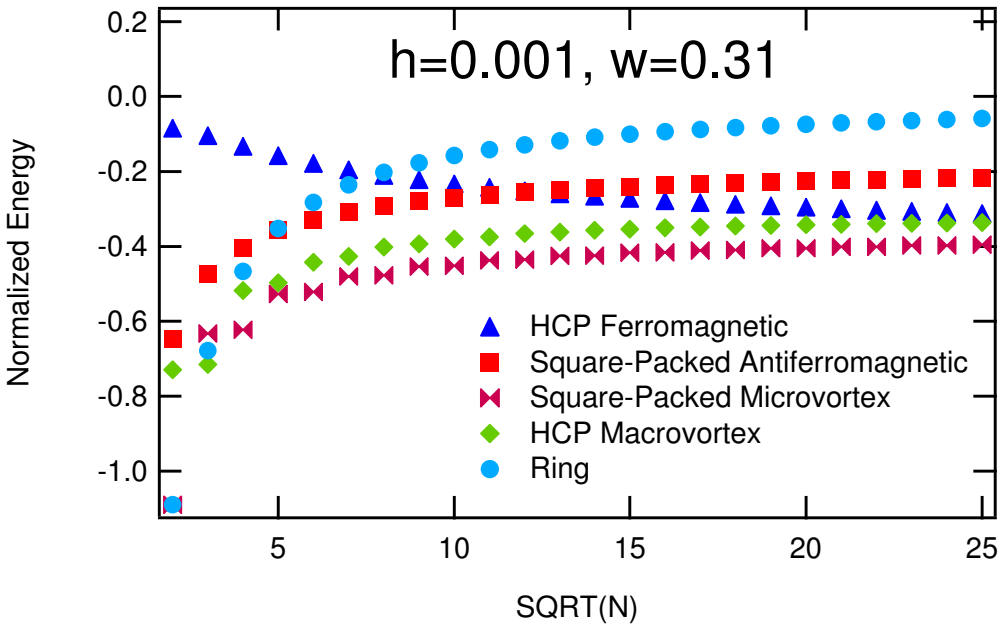

Fig. B.2: A plot of the energies (normalized to the energy of $\sqrt{N}$ infinitely separated chains of length $\sqrt{N}$) of several different patterns of $h = 0.001$,$w = 0.31$ particles versus $\sqrt{N}$. All patterns except the ring pattern are rectangular lattices of dimensions N particles by N particles. Note that the microvortex is the energetically preferred pattern for $\sqrt{N} > 3$. Also note that the HCP ferromagnetic pattern decreases significantly relative to all other patterns, over the calculated range.

C. PATTERN FORMATION IN A MONOLAYER OF MAGNETIC SPHERES

C.1 Energetic Considerations

Below are the equations used in the magnetostatic energy calculating algorithm. The calculations are performed in *Mathematica*. In general, the calculations follow the following steps:

1. Determine charge positions, r in the pattern being investigated.
2. Determine distances between any two charges, R, in the pattern.
3. Determine charge values, Q.
4. Calculate the magnetostatic energy, U of the entire pattern. Note: this step requires careful attention to summation limits so as not to double count or include particle self-energies.

The calculation of a linear chain begins with the determination of all charge positions,

$$r_{line}(d,s,m) = \begin{cases} (0, \frac{md}{2} - \frac{s}{2}), & m \text{ even} \\ (0, \frac{(m-1)d}{2} + \frac{s}{2}), & m \text{ odd} \end{cases}$$

where m is a dummy variable unique to each charge. The distances between all pairs of charges is then simply

$$R_{line}(d,s,m,n) = r_{line}(d,s,m) - r_{line}(d,s,n) \tag{C.1}$$

where n is another dummy variable unique to each charge. A charge value, $Q_{line}(q,d,s,m)$ is then assigned to each charge such that

$$Q_{line}(q,d,s,m) = \begin{cases} -\frac{qd}{s}, & m \text{ even} \\ \frac{qd}{s}, & m \text{ odd} \end{cases}$$

The energy of the linear chain is then

$$U_{line}(X,s,d,q) = \sum_{m=0}^{2X-3} \sum_{n=m+1}^{2X-1} \begin{cases} \frac{(1-\delta_{m,n-1})\mu_0}{4\pi} \frac{Q_{line}(q,d,s,m)Q_{line}(q,d,s,n)}{|R_{line}(d,s,m,n)|}, & m \text{ even} \\ \frac{\mu_0}{4\pi} \frac{Q_{line}(q,d,s,m)Q_{line}(q,d,s,n)}{|R_{line}(d,s,m,n)|}, & m \text{ odd} \end{cases}$$

where $\delta_{m,n-1}$ is the Kronecker delta, and X is the number of particles in the chain.

Similarly, the positions of all charges in an HCP ferromagnetic pattern can be calculated,

$$r_{hex}(d,s,m,n) = \begin{cases} (\frac{\sqrt{3}dn}{2}, \frac{md}{2} - \frac{s}{2}), & m \text{ even, } n \text{ even} \\ (\frac{\sqrt{3}dn}{2}, \frac{(m-1)d}{2} + \frac{s}{2}), & m \text{ odd, } n \text{ even} \\ (\frac{\sqrt{3}dn}{2}, \frac{(m+1)d}{2} - \frac{s}{2}), & m \text{ even, } n \text{ odd} \\ (\frac{\sqrt{3}dn}{2}, \frac{md}{2} + \frac{s}{2}), & m \text{ odd, } n \text{ odd} \end{cases}$$

where (m,n) is a set of dummy variables unique to each charge. The distances between all pairs of charges is then simply

$$R_{hex}(d,s,m,n,l,k) = r_{hex}(d,s,m,n) - r_{hex}(d,s,l,k) \tag{C.2}$$

where (l, k) is another set of dummy variables unique to each charge. A charge value, $Q_{hex}(q, d, s, m)$ is then assigned to each charge such that

$$Q_{hex}(q, d, s, m) = \begin{cases} -\frac{qd}{s}, & m \text{ even} \\ \frac{qd}{s}, & m \text{ odd} \end{cases}$$

The energy of the rectangular HCP ferromagnetic lattice of dimensions X *particles* $\times$ Y *particles* is then

$$U_{hex}(X, Y, s, d, q) = YU_{line}(X, s, d, q) + \sum_{m=0}^{2X-1} \sum_{n=0}^{Y-1} \sum_{l=0}^{2X-1} \sum_{k=n+1}^{Y-1} \frac{\mu_0}{4\pi} \frac{Q_{hex}(q, d, s, m) Q_{hex}(q, d, s, l)}{\mid R_{hex}(d, s, m, n, l, k) \mid} \tag{C.3}$$

Also, the positions of all charges in a square-packed antiferromagnetic pattern can be calculated,

$$r_{antsq}(d, s, m, n) = \begin{cases} (dn, \frac{md}{2} - \frac{s}{2}), & m \text{ even} \\ (dn, \frac{(m-1)d}{2} + \frac{s}{2}), & m \text{ odd} \end{cases}$$

where (m, n) is a set of dummy variables unique to each charge. The distances between all pairs of charges is then simply

$$R_{antsq}(d, s, m, n, l, k) = r_{antsq}(d, s, m, n) - r_{antsq}(d, s, l, k) \tag{C.4}$$

where (l, k) is another set of dummy variables unique to each charge. A charge value, $Q_{antsq}(q, d, s, m, n)$ is then assigned to each charge such that

$$Q_{antsq}(q, d, s, m, n) = \begin{cases} \frac{qd}{s}, & m \text{ even, } n \text{ even} \\ -\frac{qd}{s}, & m \text{ odd, } n \text{ even} \\ -\frac{qd}{s}, & m \text{ even, } n \text{ odd} \\ \frac{qd}{s}, & m \text{ odd, } n \text{ odd} \end{cases}$$

The energy of the rectangular square-packed antiferromagnetic lattice of dimensions *X particles* $\times$ *Y particles* is then

$$U_{antsq}(X,Y,s,d,q) = YU_{line}(X,s,d,q) + \sum_{m=0}^{2X-1}\sum_{n=0}^{Y-1}\sum_{l=0}^{2X-1}\sum_{k=n+1}^{Y-1}\frac{\mu_0}{4\pi}\frac{Q_{antsq}(q,d,s,m,n)Q_{antsq}(q,d,s,l,k)}{\mid R_{antsq}(d,s,m,n,l,k)\mid} \tag{C.5}$$

The positions of all charges in an HCP macrovortex pattern can be calculated, using some additional equations to account for the orientations of the particles,

$$r_{Xmacro}(d,n) = \frac{\sqrt{3}dn}{2} \tag{C.6}$$

$$r_{Ymacro}(d,m,n) = \begin{cases} \frac{(m+1)d}{2}, & m \text{ even, } n \text{ even} \\ \frac{md}{2}, & m \text{ odd, } n \text{ even} \\ -\frac{md}{2}, & m \text{ even, } n \text{ odd} \\ \frac{(m-1)d}{2}, & m \text{ odd, } n \text{ odd} \end{cases}$$

$$\theta_{macro}(d,m,n) = tan^{-1}(\frac{Xmacro}{Ymacro}) \tag{C.7}$$

Finally, the positions of the charges are determined by

$$r_{macro}(d,s,m,n) = \begin{cases} (\frac{\sqrt{3}dn}{2} + \frac{s}{2}cos(\pi+\theta_{macro}(d,m,n)), \frac{(m+1)d}{2} + \frac{s}{2}sin(\theta_{macro}(d,m,n))), & m \text{ even, } n \text{ even} \\ (\frac{\sqrt{3}dn}{2} + \frac{s}{2}cos(\theta_{macro}(d,m,n)), \frac{md}{2} + \frac{s}{2}sin(\pi+\theta_{macro}(d,m,n))), & m \text{ odd, } n \text{ even} \\ (\frac{\sqrt{3}dn}{2} + \frac{s}{2}cos(\pi+\theta_{macro}(d,m,n)), \frac{md}{2} + \frac{s}{2}sin(\theta_{macro}(d,m,n))), & m \text{ even, } n \text{ odd} \\ (\frac{\sqrt{3}dn}{2} + \frac{s}{2}cos(\theta_{macro}(d,m,n)), \frac{(m-1)d}{2} + \frac{s}{2}sin(\pi+\theta_{macro}(d,m,n))), & m \text{ odd, } n \text{ odd} \end{cases} \tag{C.8}$$

where (m, n) is a set of dummy variables unique to each charge. The distances between all pairs of charges is then simply

$$R_{macro}(d, s, m, n, l, k) = r_{macro}(d, s, m, n) - r_{macro}(d, s, l, k) \tag{C.9}$$

where (l, k) is another set of dummy variables unique to each charge. A charge value, $Q_{macro}(q, d, s, m)$ is then assigned to each charge such that

$$Q_{macro}(q, d, s, m) = \begin{cases} -\frac{qd}{s}, & m \text{ even} \\ \frac{qd}{s}, & m \text{ odd} \end{cases}$$

The energy of the HCP macrovortex lattice of dimensions X *particles* $\times$ Y *particles* is then

$$U_{macro}(X,Y,s,d,q) =$$

$$\begin{cases}
\sum_{m=-Y}^{Y-1} \sum_{n=-\frac{X-2}{2}}^{\frac{X}{2}} \sum_{k=n}^{\frac{X}{2}} \begin{cases} \sum_{l=-Y}^{Y-1} \frac{\mu_0}{4\pi} \frac{Q_{macro}(q,d,s,m)Q_{macro}(q,d,s,l)}{|R_{macro}(d,s,m,n,l,k)|}, & X,Y \text{ even}, n \neq k \\ \sum_{l=m+1}^{Y-1} \frac{\mu_0}{4\pi} \frac{Q_{macro}(q,d,s,m)Q_{macro}(q,d,s,l)}{|R_{macro}(d,s,m,n,l,k)|}, & X,Y \text{ even}, m \text{ odd}, n=k \\ \sum_{l=m+2}^{Y-1} \frac{\mu_0}{4\pi} \frac{Q_{macro}(q,d,s,m)Q_{macro}(q,d,s,l)}{|R_{macro}(d,s,m,n,l,k)|}, & X,Y,m \text{ even}, n=k \end{cases} \\
\sum_{m=-Y+1}^{Y-1} \sum_{n=-\frac{X-2}{2}}^{\frac{X}{2}} \sum_{k=n}^{\frac{X}{2}} \begin{cases} \sum_{l=-Y+1}^{Y-1} \frac{\mu_0}{4\pi} \frac{Q_{macro}(q,d,s,m)Q_{macro}(q,d,s,l)}{|R_{macro}(d,s,m,n,l,k)|}, & X \text{ even}, Y \text{ odd}, n \neq k \\ \sum_{l=m+1}^{Y} \frac{\mu_0}{4\pi} \frac{Q_{macro}(q,d,s,m)Q_{macro}(q,d,s,l)}{|R_{macro}(d,s,m,n,l,k)|}, & X,Y \text{ even}, Y,m \text{ odd}, n=k \\ \sum_{l=m+2}^{Y} \frac{\mu_0}{4\pi} \frac{Q_{macro}(q,d,s,m)Q_{macro}(q,d,s,l)}{|R_{macro}(d,s,m,n,l,k)|}, & X,Y,m \text{ even}, Y \text{ odd}, n=k \end{cases} \\
\sum_{m=-Y}^{Y-1} \sum_{n=-\frac{X-1}{2}}^{\frac{X-1}{2}} \sum_{k=n}^{\frac{X-1}{2}} \begin{cases} \sum_{l=-Y}^{Y-1} \frac{\mu_0}{4\pi} \frac{Q_{macro}(q,d,s,m)Q_{macro}(q,d,s,l)}{|R_{macro}(d,s,m,n,l,k)|}, & Y \text{ even}, X \text{ odd}, n \neq k \\ \sum_{l=m+1}^{Y-1} \frac{\mu_0}{4\pi} \frac{Q_{macro}(q,d,s,m)Q_{macro}(q,d,s,l)}{|R_{macro}(d,s,m,n,l,k)|}, & Y \text{ even}, X,m \text{ odd}, n=k \\ \sum_{l=m+2}^{Y-1} \frac{\mu_0}{4\pi} \frac{Q_{macro}(q,d,s,m)Q_{macro}(q,d,s,l)}{|R_{macro}(d,s,m,n,l,k)|}, & Y,m \text{ even}, X \text{ odd}, n=k \end{cases} \\
\sum_{m=-Y+1}^{Y} \sum_{n=-\frac{X-1}{2}}^{\frac{X-1}{2}} \sum_{k=n}^{\frac{X-1}{2}} \begin{cases} \sum_{l=-Y+1}^{Y} \frac{\mu_0}{4\pi} \frac{Q_{macro}(q,d,s,m)Q_{macro}(q,d,s,l)}{|R_{macro}(d,s,m,n,l,k)|}, & X,Y \text{ odd}, n \neq k \\ \sum_{l=m+1}^{Y} \frac{\mu_0}{4\pi} \frac{Q_{macro}(q,d,s,m)Q_{macro}(q,d,s,l)}{|R_{macro}(d,s,m,n,l,k)|}, & X,Y,m \text{ odd}, n=k \\ \sum_{l=m+2}^{Y} \frac{\mu_0}{4\pi} \frac{Q_{macro}(q,d,s,m)Q_{macro}(q,d,s,l)}{|R_{macro}(d,s,m,n,l,k)|}, & m \text{ even}, X,Y \text{ odd}, n=k \end{cases}
\end{cases} \tag{C.10}$$

The positions of all charges in a square-packed microvortex pattern can be calculated,

$$r_{micro}(d,s,m,n) = \begin{cases} (dn - \frac{\sqrt{2}s}{4}, \frac{md}{2} - \frac{\sqrt{2}s}{4}), & m,n,\frac{m}{2} \text{ even} \\ (dn + \frac{\sqrt{2}s}{4}, \frac{md}{2} - \frac{\sqrt{2}s}{4}), & m,n \text{ even}, \frac{m}{2} \text{ odd} \\ (dn + \frac{\sqrt{2}s}{4}, \frac{(m-1)d}{2} + \frac{\sqrt{2}s}{4}), & n, \frac{m-1}{2} \text{ even}, m \text{ odd} \\ (dn - \frac{\sqrt{2}s}{4}, \frac{(m-1)d}{2} + \frac{\sqrt{2}s}{4}), & n \text{ even}, m, \frac{m-1}{2} \text{ odd} \\ (dn - \frac{\sqrt{2}s}{4}, \frac{md}{2} + \frac{\sqrt{2}s}{4}), & m, \frac{m}{2} \text{ even}, n \text{ odd} \\ (dn + \frac{\sqrt{2}s}{4}, \frac{md}{2} + \frac{\sqrt{2}s}{4}), & m \text{ even}, n, \frac{m}{2} \text{ odd} \\ (dn + \frac{\sqrt{2}s}{4}, \frac{(m-1)d}{2} - \frac{\sqrt{2}s}{4}), & \frac{m-1}{2} \text{ even}, m,n \text{ odd} \\ (dn - \frac{\sqrt{2}s}{4}, \frac{(m-1)d}{2} - \frac{\sqrt{2}s}{4}), & m,n,\frac{m-1}{2} \text{ odd} \end{cases}$$

where (m,n) is a set of dummy variables unique to each charge. The distances between all pairs of charges is then simply

$$R_{micro}(d,s,m,n,l,k) = r_{micro}(d,s,m,n) - r_{micro}(d,s,l,k) \tag{C.11}$$

where (l,k) is another set of dummy variables unique to each charge. A charge value, $Q_{micro}(q,d,s,m)$ is then assigned to each charge such that

$$Q_{micro}(q,d,s,m) = \begin{cases} -\frac{qd}{s}, & m \text{ even} \\ \frac{qd}{s}, & m \text{ odd} \end{cases}$$

The energy of the square-packed microvortex lattice of dimensions X *particles* $\times$ Y *particles* is then

$$U_{micro}(X,Y,s,d,q) =$$

$$\begin{cases}
\sum_{m=-Y}^{Y-1} \sum_{n=-\frac{X-2}{2}}^{\frac{X}{2}} \sum_{k=n}^{\frac{X}{2}} \begin{cases} \sum_{l=-Y}^{Y-1} \frac{\mu_0}{4\pi} \frac{Q_{micro}(q,d,s,m)Q_{micro}(q,d,s,l)}{|R_{micro}(d,s,m,n,l,k)|}, & X,Y \text{ even, } n \neq k \\ \sum_{l=m+1}^{Y-1} \frac{\mu_0}{4\pi} \frac{Q_{micro}(q,d,s,m)Q_{micro}(q,d,s,l)}{|R_{micro}(d,s,m,n,l,k)|}, & X,Y \text{ even, } m \text{ odd, } n=k \\ \sum_{l=m+2}^{Y-1} \frac{\mu_0}{4\pi} \frac{Q_{micro}(q,d,s,m)Q_{micro}(q,d,s,l)}{|R_{micro}(d,s,m,n,l,k)|}, & X,Y,m \text{ even, } n=k \end{cases} \\
\sum_{m=-Y+1}^{Y-1} \sum_{n=-\frac{X-2}{2}}^{\frac{X}{2}} \sum_{k=n}^{\frac{X}{2}} \begin{cases} \sum_{l=-Y+1}^{Y} \frac{\mu_0}{4\pi} \frac{Q_{micro}(q,d,s,m)Q_{micro}(q,d,s,l)}{|R_{micro}(d,s,m,n,l,k)|}, & X \text{ even, } Y \text{ odd, } n \neq k \\ \sum_{l=m+1}^{Y} \frac{\mu_0}{4\pi} \frac{Q_{micro}(q,d,s,m)Q_{micro}(q,d,s,l)}{|R_{micro}(d,s,m,n,l,k)|}, & X,Y \text{ even, } Y,m \text{ odd, } n=k \\ \sum_{l=m+2}^{Y} \frac{\mu_0}{4\pi} \frac{Q_{micro}(q,d,s,m)Q_{micro}(q,d,s,l)}{|R_{micro}(d,s,m,n,l,k)|}, & X,Y,m \text{ even, } Y \text{ odd, } n=k \end{cases} \\
\sum_{m=-Y}^{Y-1} \sum_{n=-\frac{X-1}{2}}^{\frac{X-1}{2}} \sum_{k=n}^{\frac{X-1}{2}} \begin{cases} \sum_{l=-Y}^{Y-1} \frac{\mu_0}{4\pi} \frac{Q_{micro}(q,d,s,m)Q_{micro}(q,d,s,l)}{|R_{micro}(d,s,m,n,l,k)|}, & Y \text{ even, } X \text{ odd, } n \neq k \\ \sum_{l=m+1}^{Y-1} \frac{\mu_0}{4\pi} \frac{Q_{micro}(q,d,s,m)Q_{micro}(q,d,s,l)}{|R_{micro}(d,s,m,n,l,k)|}, & Y \text{ even, } X,m \text{ odd, } n=k \\ \sum_{l=m+2}^{Y-1} \frac{\mu_0}{4\pi} \frac{Q_{micro}(q,d,s,m)Q_{micro}(q,d,s,l)}{|R_{micro}(d,s,m,n,l,k)|}, & Y,m \text{ even, } X \text{ odd, } n=k \end{cases} \\
\sum_{m=-Y+1}^{Y} \sum_{n=-\frac{X-1}{2}}^{\frac{X-1}{2}} \sum_{k=n}^{\frac{X-1}{2}} \begin{cases} \sum_{l=-Y+1}^{Y} \frac{\mu_0}{4\pi} \frac{Q_{micro}(q,d,s,m)Q_{micro}(q,d,s,l)}{|R_{micro}(d,s,m,n,l,k)|}, & X,Y \text{ odd, } n \neq k \\ \sum_{l=m+1}^{Y} \frac{\mu_0}{4\pi} \frac{Q_{micro}(q,d,s,m)Q_{micro}(q,d,s,l)}{|R_{micro}(d,s,m,n,l,k)|}, & X,Y,m \text{ odd, } n=k \\ \sum_{l=m+2}^{Y} \frac{\mu_0}{4\pi} \frac{Q_{micro}(q,d,s,m)Q_{micro}(q,d,s,l)}{|R_{micro}(d,s,m,n,l,k)|}, & m \text{ even, } X,Y \text{ odd, } n=k \end{cases}
\end{cases} \tag{C.12}$$

The positions of all charges in a ring pattern can be calculated, using an additional equation to account for the orientations of the particles,

$$\theta_{ring}(X,n) = \begin{cases} \frac{\pi n}{X}, & n \text{ even} \\ \frac{\pi(n+1)}{X}, & n \text{ odd} \end{cases}$$

where X is the number of particles in the ring. Finally, the positions of the charges are determined by

$$r_{ring}(X,n,d,s) =$$
$$\begin{cases} \left(\frac{d}{2sin(\frac{\pi}{X})}sin(\theta_{ring}(X,n))+\frac{s}{2}cos(\theta_{ring}(X,n)),\frac{d}{2sin(\frac{\pi}{X})}cos(\theta_{ring}(X,n))-\frac{s}{2}sin(\theta_{ring}(X,n))\right), & n \text{ even} \\ \left(\frac{d}{2sin(\frac{\pi}{X})}sin(\theta_{ring}(X,n))-\frac{s}{2}cos(\theta_{ring}(X,n)),\frac{d}{2sin(\frac{\pi}{X})}cos(\theta_{ring}(X,n))+\frac{s}{2}sin(\theta_{ring}(X,n))\right), & n \text{ odd} \end{cases} \tag{C.13}$$

where n is a dummy variable unique to each charge. The distances between all pairs of charges is then simply

$$R_{ring}(d,s,m,n,X) = r_{ring}(X,m,d,s) - r_{ring}(X,n,d,s) \tag{C.14}$$

where m is another dummy variable unique to each charge. A charge value, $Q_{ring}(q,d,s,n)$ is then assigned to each charge such that

$$Q_{ring}(q,d,s,n) = \begin{cases} \frac{qd}{s}, & n \text{ even} \\ -\frac{qd}{s}, & n \text{ odd} \end{cases}$$

The energy of the ring is then

$$U_{ring}(X,s,d,q) = \frac{Xq^2d^2\mu_0}{4\pi s^3} + \sum_{m=0}^{2X-2}\sum_{n=m+1}^{2X-1}\frac{\mu_0}{4\pi}\frac{Q_{ring}(q,d,s,m)Q_{ring}(q,d,s,n)}{\mid R_{ring}(d,s,m,n,X)\mid} \quad \text{(C.15)}$$

BIBLIOGRAPHY

[1] E. Hamel, *Pharmac. Ther.* **55**, 31 (1992).

[2] A. Jordan, J. A. Hadfield, N. J. Lawrence, and A. T. McGown, *Med. Res. Rev.* **18**, 259 (1998).

[3] P. F. Mühlradt, and F. Sasse, *Canc. Res.* **57**, 3344 (1997).

[4] G. Agarwal, J. C. Wang, S. Kwong, S. M. Cohen, F. A. Ferrone, R. Josephs, and R. W. Briehl, *J. Mol. Biol.* **322**, 395 (2002).

[5] J. A. Hadfield, S. Ducki, N. Hirst, and A. T. McGown, *Prog. Cell Cyc. Res.* **5**, 309 (2003).

[6] K. De'Bell, A. B. MacIsaac, and J. P. Whitehead, *Rev. Mod. Phys.* **72**, 225 (2000).

[7] J. J. Weis, J. M. Tavares, and M. M. Telo da Gama, *J. Phys.: Cond. Mat.* **14**, 9171 (2002).

[8] M. Golosovsky, Y. Saado, and D. Davidov, *Appl. Phys. Lett.* **75**, 4168 (1999).

[9] W. Wen, L. Zhang, and P. Sheng, *Phys. Rev. Lett.* **85**, 5464 (2000).

[10] G. Helgesen and A. T. Skjeltorp, *J. Appl. Phys.* **69**, 8277 (1991).

[11] W. Wen, F. Kun, K. F. Pál, D. W. Zheng, and K. N. Tu, *Phys. Rev. E* **59**, R4758 (1999).

[12] K. Butter, P. H. H. Bomans, P. M. Frederik, G. J. Vroege, and A. P. Philipse, *Nature Mat.* **2**, 88 (2003).

[13] A. T. Skjeltorp, *Phys. Rev. Lett.* **51**, 2306 (1983).

[14] R. Seshadri and R. M. Westervelt, *Phys. Rev. B* **46**, 5142 (1992).

[15] M. K. Bologa, Yu. A. Buevich, S. V. Syutkin, V. V. Tetyukhin *Bull. Acad. Sci. USSR Phys. Ser.* **51**, 62 (1987).

[16] A. Wachowiak, J. Wiebe, M. Bode, O. Pietzsch, M. Morgenstern, and R. Wiesendanger, *Science* **298**, 577 (2002).

[17] M. Rahm, J. Biberger, V. Umansky, and D. Weiss, *J. Appl. Phys.* **93**, 7429 (2003).

[18] R. Pulwey, M. Rahm, J. Biberger, and D. Weiss, *IEEE Trans. Mag.* **37**, 2076 (2001).

[19] A. Fernandez and C. J. Cerjan, *J. Appl. Phys.* **87**, 1395 (2000).

[20] J. Raabe, R. Pulwey, R. Sattler, T. Schweinböck, J. Zweck, and D. Weiss, *J. Appl. Phys.* **88**, 4437 (2000).

[21] R. P. Cowburn, D. K. Koltsov, A. O. Adeyeye, and M. E. Welland, *Phys. Rev. Lett.* **83**, 1042 (1999).

[22] T. Shinjo, T. Okuno, R. Hassdorf, K. Shigeto, and T. Ono, *Science* **289**, 930 (2000).

[23] G. Gubbiotti, G. Carlotti, F. Nizzoli, R. Zivieri, T. Okuno, and T. Shinjo, *IEEE Trans. Mag.* **38**, 2532 (2002).

[24] H. Sun, R. O. Watts, and U. Buck, *J. Chem. Phys.* **96**, 1810 (1992).

[25] A. S. Clarke and G. N. Patey, *J. Chem. Phys.* **100**, 2213 (1994).

[26] D. L. Blair and A. Kudrolli, *Phys. Rev. E* **67**, 021302 (2003).

[27] K-P Schneider and J. Keller, *Chem. Phys. Lett.* **275**, 63 (1997).

[28] M. C. Phillips, D. A. Cadenhead, R. J. Good, and H. F. King, *J. Coll. Int. Sci.* **37**, 437 (1971).

[29] J. J. Weis, *Molec. Phys.* **100**, 579 (2002).

[30] J. J. Weis, *Molec. Phys.* **93**, 361 (1998).

[31] K. De'Bell, A. B. MacIsaac, I. N. Booth, and J. P. Whitehead, *Phys. Rev. B* **55**, 15108 (1997).

[32] J. M. Tavares, J. J. Weis, and M. M. Telo da Gama, *Phys. Rev. E* **59**, 4388 (1999).

[33] M. A. Osipov, P. I. C. Teixeira, and M. M. Telo da Gama, *Phys. Rev. E* **54**, 2597 (1996).

[34] D. Levesque and J. J. Weis, *Phys. Rev. E* **49**, 5131 (1994).

[35] R. P. Sear, *Phys. Rev. Lett.* **76**, 2310 (1996).

[36] R. W. Briehl, and E. S. Mann, *Ann. N. Y. Acad. Sci.* **565**, 295 (1989).

[37] E. Unger, K. J. Böhm, an W. Vater, *Elec. Mic. Rev.* **3**, 355 (1990).

[38] B. Trpišová and J. A. Brown, *Int. J. of Mod. Phys. B* **12** (1998).

[39] H. Li and J. J. McCarthy, *Phys. Rev. Lett.* **90**, 184301 (2003).

[40] A. Samadani and A. Kudrolli, *Phys. Rev. E* **64**, 051301 (2001).

[41] J. Stambaugh, D. P. Lathrop, E. Ott, and W. Losert *Phys. Rev. E* **68**, 026207 (2003).

[42] J. Stambaugh, Z. Smith, E. Ott, and W. Losert, *Phys. Rev. E* **70**, 031304 (2004).

[43] K.I. Morozov, and M.I. Shliomis, *Ferrofluids: Magnetically Controllable Fluids and their Applications*, 162 (2002).

[44] W. Losert, D. G. W. Cooper, J. Delour, A. Kudrolli, and J. P. Gollub, *Chaos* **9**, 682 (1999).

[45] B. Chen, and J. I. Siepmann, *J. Phys. Chem. B* **105**, 11275 (2001).

[46] U. H. E. Hansmann, *Chem. Phys. Lett.* **281**, 140 (1997).

[47] M. G. Wu, and M. W. Deem, *Mol. Phys.* **97**, 559 (1999).

[48] J. Dudowicz, K. F. Freed, and J. F. Douglas, *Phys. Rev. Lett.* **92**, 045502 (2004).

[49] K. Van Workum and J. F. Douglas, *Phys. Rev. E*, (2004).

[50] F. W. Starr, J. F. Douglas, and S. C. Glotzer, *J. Chem. Phys.* **119**, 1777 (2003).

[51] F. S. Dainton and K. J. Ivin, *Nature* **162**, 705 (1948).

[52] P. I. Belobrov, V. A. Voevodin, and V. A. Ignatchenko, *Sov. Phys. JETP* **61**, 522 (1985).

[53] V. M. Rozenbaum, and V. M. Ogenko, *Sov. Phys. JETP* **35**, 184 (1982).

[54] P. J. Camp and G. N. Patey, *Phys. Rev. E* **60**, 4280 (1999).

[55] J. D. Jackson, *Classical Electrodynamics* **3rd Edition**, 145 (1999).

[56] T. Tlusty and S. A. Safran, *Science* **290**, 1328 (2000).

[57] A. Gil-Villegas, S. C. McGrother, G. Jackson, *Chem. Phys. Lett.* **269**, 441 (1997).

[58] J. G. Brankov and D. M. Danchev, *Physica A* **144**, 441 (1987).

[59] J. Ottino and D. Khakhar, *Annu. Rev. Fluid Mech.* **32**, 55 (2000).

[60] M. Newey, J. Ozik, S. M. van der Meer, E. Ott, and W. Losert, *Europhys. Lett.* **66**, 205 (2004).

[61] N. Lecocq and N. Vandewalle, *Fractals* **11**, 259 (2003).

[62] H.A. Makse, S. Havlin, P.R. King, and H.E. Stanley, *Nature* **386**, 379 (1997).

[63] J. S. Olafsen and J. S. Urbach, *Phys. Rev. Lett.* **81**, 4369 (1998).

[64] W. Losert, D.G.W. Cooper, and J.P. Gollub, *Phys. Rev. E* **59**, 5855 (1999).

[65] E. Ben-Naim, Z. A. Daya, P. Vorobieff, and R. E. Ecke *Phys. Rev. Lett.* **86**, 1414 (2001).

[66] A Kentsis, and K. L. B. Borden, *Curr. Prot. Pep. Sci.* **5**, 125 (2004).

[67] H. Kuivaniemi, G. Tromp, and D. J. Prockop, *FASEB J.* **5**, 2052 (1991).

[68] J. Tame and B. Vallone, *Acta Cryst. D* **56**, 805 (2000).

[69] D. J. Harrington, K. Adachi, and W. E. Royer Jr., *J. Mol. Biol.* **272**, 398 (1997)

[70] K. H. Downing, and E. Nogales, *Curr. Op. Cell Biol.* **10**, 16 (1998).

[71] D. L. Sackett, *Sub-cell. Biochem.* **24**, 255 (1995).

[72] J. Lowe, H. Li, K. H. Downing, and E. Nogales, *J. Mol. Biol.* **313**, 1045 (2001).

[73] J. Bella, M. Eaton, B. Brodsky, and H. M. Berman, *Science* **266**, 75 (1994).

[74] S. Han, K. Lee, and W. Losert, *unpublished data.*

[75] D. Sept, N. A. Baker, and J. A Mccammon, *Prot. Sci.* **12**, 2257 (2003).

[76] J. Kyte, *Biophys. Chem.* **100**, 193 (2003).

[77] J. A. Brown, *PhD Thesis* University of Alberta (Edmonton) (1999).

[78] S. Takashima, *Biophys. J.* **64**, 1550 (1993).

[79] S. G. Wolf, G. Mosser, and K. H. Downing, *J. Struc. Biol.* **111**, 190 (1993).

[80] R. H. Wade, D. Chretien, and E. Pantos, *Elec. Crys. Org. Mol.*, **317** (1990).

[81] D. Chrétien, and S. D. Fuller, *J. Mol. Biol.* **298**, 663 (2000).

[82] E. Mandelkow, E. Mandelkow, and R. A. Milligan, *J. Cell Biol.* **114**, 977 (1991).

[83] M. E. Janson, M. E. de Hood, and M. Dogterom, *J. Cell Biol.* **161**, 1029 (2003).

[84] I. M. Jnosi, D. Chrtien, and H. Flyvbjerg, *Eur. Biophys. J.* **27**, 501 (1998).

[85] V. VanBuren, D. J. Odde, and L. Cassimeris, *J. Cell Biol.* **99**, 6035 (2002).

[86] P. Meurer-Grob, J. Kasparian, and R. H. Wade, *Biochem.* **40**, 8000 (2001).

[87] P. M. Vassilev, R. T. Dronzine, M. P. Vassileva, and G. A. Georgiev, *Annu. Biosci. Rep.* **2**, 1025 (1982).

[88] W. J. Meggs, *Med. Hyp.* **26**, 165 (1988).

[89] L. J. Gagliardi, *Phys. Rev. E* **66**, 011901 (2002).

[90] J. Vassy, S. Portet, M. Beil, G. Millot, F. Fauvel-Lafève, G. Gasset, and D. Schoevaert, *Adv. Space Res.* **32**, 1595 (2003).

[91] M. V. Satarić and J. A. Tuszyński, *Phys. Rev. E* **67**, 011901 (2003).

[92] J. A. Tuszyński, B. Trpišová, D. Sept, and J. A. Brown, *J. Struc. Biol.* **118**, 94 (1997).

[93] H. Boukari, R. Nossal, and D. L. Sackett, *Biochem.* **42**, 1292 (2003).